Chemistry and Physics of Metallic Contaminants on Crystalline Silicon Surfaces

by

Gerd Johan Maria Norga

Burgerlijk Ingenieur Materiaalkunde, KU Leuven (1992)

Submitted to the Department of Materials Science and Engineering in partial fulfillment of the requirements for the degree of

Doctor of Science in Electronic Materials

at the

MASSACHUSETTS INSTITUTE OF TECHNOLOGY

June 1996

© Massachusetts Institute of Technology 1996. All rights reserved.

Author .....

Department of Materials Science and Engineering
May 3, 1996

Certified by ....
Lionel C. Kimerling
Thomas Lord Professor of Materials Science
Thesis Supervisor

Accepted by ....
Michael F. Rubner
TDK Professor of Materials Science and Engineering
Chair, Departmental Committee on Graduate Students

MASSACHUSETTS INSTITUTE OF TECHNOLOGY

JUN 24 1996

ARCHIVES

Chemistry and Physics of Metallic Contaminants on Crystalline Silicon Surfaces

by

Gerd Johan Maria Norga

Submitted to the Department of Materials Science and Engineering
on May 3, 1996, in partial fulfillment of the
requirements for the degree of
Doctor of Science in Electronic Materials

Abstract

A superior control over the surface chemistry of crystalline silicon in wet and dry ambients is an essential requirement for achieving high product yield in integrated circuit manufacturing. The continual reduction in feature sizes, necessary to accommodate higher clock speeds, has emphasized the role of wet wafer cleaning to meet stringent surface purity needs. Because of their deleterious effects on device operation, control and detection of trace metals on silicon is especially critical. Meanwhile, increases in process complexity have created a need for fast, *in situ* analysis techniques for early detection of process contamination.

Radio frequency photoconductance decay (RFPCD) is a noninvasive technique to measure carrier lifetime in silicon. On high bulk lifetime (> 1 ms) silicon, RFPCD allows the measurement of surface defects with extraordinary sensitivity ($\approx 10^8$ cm^{-2}). We have used RFPCD for *in situ* studies of silicon surface reactions in wet and dry ambients. *Ab initio* electronic structure calculations at the Hartree-Fock level were used to model the reactivity of chemisorbed impurities on hydrogen terminated silicon. Reasonable agreement was obtained between bond polarity, obtained from population analysis of the electron density results, and experimentally observed reactivity towards polar molecules such as HF and water.

Chemisorbed metal atoms introduce states in the HOMO-LUMO "bandgap" of the orbital energy spectrum. These states are due to localized orbitals on the metal atom. Chemisorption of oxygen introduces gap states arising from silicon dangling bonds. Both types of surface states act as efficient recombination centers for excess carriers, and can therefore be detected by surface recombination velocity measurement using RFPCD.

To ensure accurate quantitation of surface state density, the effects of injection level and surface charge on the RFPCD measurement were analyzed. We developed a detailed theoretical model for the dependence of surface recombination on injection level in the presence of surface charge. Our analysis extends the Shockley-Read-Hall formalism to include the effect of bandbending on surface recombination velocity. The extraction of the areal density of surface charge Q from the intensity dependence of

the surface lifetime is demonstrated for a thermally oxidized wafer. Using a potentiostat to control the bias voltage across a silicon/HF liquid junction, we confirm the strong increase in surface recombination velocity with bandbending potential towards depletion, as predicted by our analysis. This method provides an estimate for the energy position of the recombination centers in the gap.

In oxidizing cleaning solutions, effective metal removal is dependent on high ionic solubility. Metal deposition increases with the tendency of a metal to form silicate-like bonding arrangements with Si and O in the chemical oxide. We propose the use of E-pH diagrams (E = oxidation potential, pH=-log([H^+])) to assist in the design of novel cleaning chemistries for optimum metal removal. E-pH diagrams have significant potential for the development of more "robust" cleaning chemistries, which achieve satisfactory contaminant removal even when chemical purity specifications are relaxed.

In HF-based cleaning solutions, metal deposition involves reduction of metal ions, a process which is driven by the difference between the electron (quasi) fermi energy in the silicon and the redox levels of ions in solution. Deposition occurs only when the driving force for deposition is positive, such as for Cu and Au. We present a detailed model for the energetics of the deposition reaction, based on the alignment of the silicon bands with the redox levels of ions in solution. For copper, the driving force for reduction at the Si/solution interface is small and nucleation of metallic copper clusters is therefore required. Cluster nucleation is slow, because reduction of copper ions requires electron capture from surface states by the Cu^{++}/Cu^{+} couple. For gold, the driving force for reduction is much larger and ions deposit by hole injection into the silicon valence band. We studied the effect of doping type, illumination intensity and sample bias on the copper deposition rate and growth morphology using AFM, TXRF (total X-ray fluorescence) and RFPCD. Nucleation on p-type is slower than on n-type, and illumination increases nucleation for both types. Anodic biasing reduces nucleation drastically. All three effects are in excellent agreement with model predictions.

The sensitivity of the RFPCD measurement to surface metals depends on wafer thickness, bulk lifetime, and the cross section of the defect for carrier capture. For gold, we find a cross section of 10^{-17} cm^2, resulting in a detection limit of 10^{10} cm^{-2} on high lifetime CZ material. Since RFPCD measures the density of surface defects, the sensitivity of the technique is degraded as the size of the copper clusters increases. However, air exposure leads to a major improvement in detection sensitivity for very low copper levels ($< 10^{10}$ cm^{-2}). We attribute this effect to reduction of chemisorbed copper ions at surface states introduced by native oxide growth. After air exposure, we obtain a cross section of 10^{-15} cm^2 per copper atom, resulting in a detection limit of 10^8 cm^{-2}. This value represents an improvement in sensitivity by a factor of 50 over today's most advanced techniques for wafer surface analysis.

Thesis Supervisor: Lionel C. Kimerling
Title: Thomas Lord Professor of Materials Science

Acknowledgements

First and foremost, I wish to express my deepest gratitude to Professor Kim Kimerling, for giving me the freedom and opportunity to pursue a dream. This thesis adventure would not have been possible without his support, both moral and material. I am happy to have been part of his research group and thank him for teaching me the value of knowledge.

I want to acknowledge all the undergraduate students who were involved in my thesis project, especially Alexis Black, for her key role in the experimental work, and Marlene Platero, for her help with the AFM analyses. Without them, it would have been impossible for me to finish this work in the allotted time.

Thanks to all the people who helped make my MIT years such a memorable time: especially my housemates, Alan and Jeet, my friends Nozomi and Ahmed, and my brother Koen. I am grateful to Aimeé Smith, Anton Vanderven and Anand Reddy, for generously sharing food and friendship during the writing part. Thanks also to all the present and past members of the Kimerling group, especially to Jurgen, Kate, Song and Laura, for their cheerful presence, help and support. I know that I could not have wished a better research group to work in.

I thank David Clarke of UC Santa Barbara for encouraging me to undertake graduate studies in the US.

I am grateful to my parents for their support and encouragements, and to Pascale for her friendship and love from faraway.

This research was supported by the MIT Leaders for Manufacturing program. Critical technical support from industrial collaborators, especially Ed Wijaranakula of SEH, Zach Hatcher of Ashland Chemical and Jamie Rose of DEC, is much appreciated.

Contents

1 Introduction 18

1.1 Motivation 18

1.2 Scope and structure 21

2 Cleaning and Surface Preparation for IC Manufacturing 25

2.1 Introduction 25

2.2 Effects of metallic contamination on device performance 26

2.3 The RCA clean 27

2.4 HF-based cleaning solutions 30

2.4.1 Dilute HF 30

2.4.2 Buffered HF 31

2.5 The Piranha clean 32

2.6 New approaches and future trends 32

3 Experimental Techniques and Analysis Methods 34

3.1 Introduction 34

3.2 Total reflection X-ray fluorescence (TXRF) 35

3.3 Atomic force microscopy (AFM) 37

3.3.1 Principle of operation 37

3.3.2 Quantification of metallic precipitates using AFM 40

3.4 Liquid chemical analysis 42

3.4.1 Graphite furnace atomic absorption spectroscopy 42

3.4.2 Inductively coupled plasma mass spectroscopy 43

3.5 Wafer surface preparation procedure 43
3.5.1 Chemicals 43
3.5.2 Beakerware 44
3.5.3 Cleaning recipe 44
3.5.4 Controlled contamination 45
3.6 Wafer material 46

4 Surface Recombination of Photoexcited Carriers 48
4.1 Introduction 48
4.2 Background 50
4.2.1 The effect of injection level on recombination rate 50
4.2.2 Principle of operation of radio-frequency photoconductance decay 54
4.2.3 Measurement of surface recombination velocity 57
4.2.4 Carrier excitation by monochromatic light 58
4.3 Effect of bandbending on surface recombination 61
4.3.1 Relationship between excess carrier density and surface bandbending 61
4.3.2 Dependence of surface recombination rate on excess carrier density in presence of bandbending 64
4.3.3 Effect of bandbending on minority carrier decay 65
4.4 The dependence of surface recombination velocity on bias potential . 69
4.4.1 Introduction 69
4.4.2 Experimental 70
4.4.3 Results and discussion 70
4.5 Intensity dependence of surface lifetime 73
4.5.1 Experimental 73
4.5.2 Results 73
4.5.3 Discussion 75
4.6 Conclusions 77

5 Impurity Chemisorption on Hydrogen Terminated Silicon 80

5.1 Introduction 80
5.2 Background 81
5.2.1 Halogen adsorption 81
5.2.2 Oxygen adsorption 82
5.3 Computational approach 83
5.3.1 *Ab initio* electronic structure methods 83
5.3.2 The Hartree-Fock approximation 84
5.3.3 Cluster choice 87
5.4 Halogen chemisorption on Si(100)-H 89
5.4.1 Character of the silicon-halogen bond 89
5.4.2 Stability of halogen termination in different ambients 92
5.5 Oxygen chemisorption on Si(100)-H 96
5.5.1 Chemisorption mechanism 96
5.5.2 Effect of chemisorbed impurities on the electronic structure of the hydrogen passivated surface 97
5.6 Metal chemisorption on Si(100)-H 99
5.6.1 Chemisorption mechanism 99
5.6.2 Effect of chemisorbed copper on the electronic structure of the surface 102
5.7 *In situ* measurements of silicon surface reactions using RFPCD 105
5.7.1 *In situ* monitoring of chemical oxide etching in HF 105
5.7.2 Measurement of O_2 adsorption on Si-H 107
5.8 Conclusions 110

6 Metal Deposition from Hydrofluoric Acid Solutions 112
6.1 Introduction 112
6.2 Background 113
6.2.1 The germanium years 113
6.2.2 Semiconductor electrochemistry 115
6.2.3 Metal-decorated semiconductors for liquid-junction photovoltaics 115

6.2.4 Metallic contamination in silicon wafer cleaning 116
6.3 Model for metal deposition onto hydrogen-terminated silicon from HF solutions 117
6.3.1 Thermodynamics of metal reduction at silicon 117
6.3.2 Kinetics of metal reduction at silicon 121
6.3.3 Growth of metallic precipitates on silicon 123
6.4 Experimental results 123
6.4.1 Deposition tendencies for various metals 123
6.4.2 *In situ* detection of copper deposition from HF 126
6.4.3 Effect of chloride ion on copper deposition from HF 128
6.4.4 In situ detection of gold deposition from HF 133
6.4.5 Dependence of gold deposition rate and surface lifetime on immersion time 134
6.4.6 Effect of doping type on copper deposition rate 137
6.4.7 Effect of doping type on precipitate size 142
6.4.8 Effect of HF concentration on copper deposition rate 148
6.4.9 Impact of ambient exposure on copper-induced surface lifetime degradation 151
6.4.10 Effect of illumination on copper deposition rate 154
6.4.11 Effect of bias potential on copper deposition rate 159
6.4.12 The effect of trace copper levels on dielectric strength of ultra-thin thermal oxides 165
6.5 Conclusions 169

7 Metallic Contaminants in Oxidizing Cleaning Solutions 173
7.1 Introduction 173
7.2 Thermodynamics of metallic contaminants in oxidizing cleaning solutions 174
7.2.1 Introduction 174
7.2.2 The representation of cleaning solutions on an E-pH map . . . 175
7.2.3 E-pH diagrams for metallic contaminants 176

7.3 Kinetics of metal deposition and removal in oxidizing cleaning mixtures 181
7.3.1 The deposition mechanism 181
7.3.2 Driving force for deposition 182
7.3.3 Model for simultaneous etching, deposition and oxidation . . . 185
7.3.4 Time dependence of the surface contaminant level 187
7.3.5 Discussion of model results 189
7.4 Conclusions 190

8 Research Achievements, Applications and Future Strategies 194
8.1 Summary 194
8.2 Applications 198
8.3 Future strategies 200

List of Figures

1-1 Moore's law 20

3-1 Operating principle of total reflection X-ray fluorescence (TXRF). . . 36
3-2 TXRF spectrum of a gold contaminated wafer 38
3-3 Operating principle of scanning tunneling microscopy (STM). 39
3-4 The effect of tip radius when imaging tall features on an otherwise smooth surface. 41

4-1 Three basic mechanisms for excess carrier recombination in semiconductors: (a) radiative; (b) Auger and (c) recombination via a deep level (Shockley-Read-Hall). 50
4-2 Two recombination modes for excess carriers: (a) band-to-band recombination with simultaneous emission or absorption of a phonon and (b) recombination via a deep level (Shockley-Read-Hall). 51
4-3 The operating principle of radio-frequency photoconductance decay. . 55
4-4 The measurement of surface recombination velocity by photoconductance decay. 58
4-5 Surface band bending terminology. x_d is the space charge region (SCR) width, L_n is the minority carrier diffusion length, and ϕ_s is the bandbending potential (positive in depletion). 62
4-6 Effect of excess carrier concentration on recombination rate, in presence of bandbending in depletion. 66
4-7 Effect of excess carrier concentration on recombination rate, in presence of bandbending in inversion. 68

4-8 The experimental setup for the surface potential dependent lifetime measurements. 71
4-9 The dependence of the reciprocal effective lifetime on bias potential. . 72
4-10 The effect of injection level on the normalized photoconductance decay transient plotted on a (a) linear and (b) logarithmic scale. The light intensity was varied by varying the distance between the LED and the wafer surface. The drive current was 1 A. The curves plotted are for relative illumination intensities (1) 1.00, (2) .0625, (3) .0156, (4).00360. 74
4-11 The variation of effective lifetime, τ_{eff}, with log(relative illumination intensity). 77

5-1 The Si_9H_{14} cluster, used to model monovalent termination of the silicon (100) surface. The top and second layer silicon atoms are indicated. . 88
5-2 Total valence electron density maps for (a) $Si_9H_{12}F_2$ and (b) $Si_9H_{12}Cl_2$. The slice is defined by the two top silicon and the lowest lying (fourth layer) silicon. 90
5-3 Passivation attack by backbond insertion. 94
5-4 Passivation attack by hydrolysis of the surface bonds. 95
5-5 The catalysing role of water in the condensation of surface silanols. This reaction introduces a bridging oxygen and two dangling bonds. . 98
5-6 Orbital energies for Si_9H_{14}; $Si_9H_{12}F_2$; $Si_9H_{12}Cl_2$; $Si_9H_{12}Br_2$; $Si_9H_{12}I_2$; $Si_9H_{12}(OH)_2$. Only the energy values near the HOMO and LUMO level are shown. 100
5-7 The $Si_9H_{12}O$ cluster and its orbital energy levels. Only the energy values near the HOMO and LUMO level are shown. 101
5-8 The $Si_9H_{14}Cu$ cluster used to model the bonding of an individual copper atoms to (100) silicon. 103
5-9 Orbital energies for (a) Si_9H_{14}; (b) $Si_9H_{14}Cu$ (alpha electrons) and (c) $Si_9H_{14}Cu$ (beta electrons) 104

5-10 The effect of oxide etching and hydrogen termination buildup on the surface lifetime and surface state density of a p-type FZ wafer. The surface state density obeys a single exponential decay with rate constant k_f=0.3125 s^{-1}. A minority capture cross section of 10^{-15} cm^2 was assumed. 106

5-11 (a) The effect of oxygen exposure on the effective lifetime of an n-type CZ wafer. The measurement was started immediately after the wafer was removed from the 48 % HF solution. (b) The density of surface states corresponding to the lifetime measurement shown in Figure 5.11a. A minority capture cross section of 10^{-15} cm^2 was assumed. . 108

6-1 A simple band model for the reduction of metal ions from solution. . 119

6-2 The Gerischer mechanism for oxidoreduction reactions at the semiconductor/electrolyte interface. 122

6-3 The effect of immersion in a contaminated solution on the surface lifetime. The wafers were immersed in 1:100 HF solutions containing 1 ppm of V, Fe and Cu ions respectively. 125

6-4 In-situ detection of copper deposition from a 1:100 dilute HF solution. 127

6-5 Effect of chloride ion on copper deposition from dilute HF. (a) Wafer exposed to 10 ppb Cu^{++}, no Cl^-; (b) wafer exposed to 10 ppb Cu^{++} and 2 ppm Cl^-. 129

6-6 10x10μm AFM image of the sample exposed to 10 ppb Cu^{++} in 1:100 HF for 3200s, 2 ppm Cl^- added to solution. 131

6-7 10x10μm AFM image of the sample exposed to 10 ppb Cu^{++} in 1:100 HF for 3200s, no Cl^- added. 132

6-8 In-situ detection of gold deposition from a 1:100 dilute HF solution. . 135

6-9 Variation of surface lifetime, τ, with immersion time, t, plotted as (a) log τ vs log t and (b) $1/\tau$ vs $t^{1/2}$. The solutions contained 10 ppb Au^{+++} as $AuCl_3$. The wafers were measured by immersion in 48 % HF immediately after the contamination treatment. 136

6-10 Variation of gold coverage, determined by TXRF, with immersion time. 138
6-11 The effect of copper concentration in 1:100 HF solution on lifetime and deposition level for (a) n and (b) p-type wafers. All wafers were immersed for 5 minutes. 140
6-12 AFM image of a n-type wafer immersed for 5 minutes in 1:100 HF containing 400 ppb Cu^{++}. 143
6-13 AFM image of a p-type wafer immersed for 5 minutes in 1:100 HF containing 400 ppb Cu^{++}. 144
6-14 Precipitate size distribution of the wafers immersed for 5 minutes in 1:100 HF containing 400 ppb Cu^{++}. 145
6-15 The effect of HF concentration on copper deposition level and lifetime. The wafers were immersed for 5 minutes in solutions containing 30 ppb Cu^{++}. Lifetimes were measured by 48% HF-immersed RFPCD immediately after the contamination treatment. 149
6-16 (a) Variation of surface lifetime with spiking level and immersion time. The wafers were exposed to air for several hours before being measured in 48 % HF. (b) Variation of surface lifetime with immersion time for n and p-type wafers. The wafers were exposed to 1:100 HF solutions containing 50 ppb Cu^{++}, followed by air exposure for 24 hours before being measured in 48 % HF. 152
6-17 The effect of illumination on copper deposition on silicon from 1:100 HF solution. 155
6-18 The effect of illumination on precipitate size and density for n and p-type wafers immersed for 2 min. in 1:100 HF containing 200 ppb Cu^{++}. Density and average precipitate size were obtained from 5x5 μm AFM images. 157
6-19 The effect of connecting the wafer to a Pt electrode on the electrode potential of n and p-type silicon. 160

6-20 The effect of contacting the wafer to an immersed Pt electrode on the precipitate size for n and p-type wafers immersed for 2 min. in 1:100 HF containing 200 ppb Cu^{++}. The average precipitate sizes were obtained from 5x5 μm AFM images. 162
6-21 The effect of contacting the wafer to an immersed Pt electrode on the number of precipitates for n and p-type wafers immersed for 2 min. in 1:100 HF containing 200 ppb Cu^{++}. The numbers of precipitates were obtained from 5x5 μm AFM images. 163
6-22 Weibull plots of breakdown voltage E_{bd} for 200 Å, 90 Åand 70 Åoxides. 170

7-1 The E-pH diagram for the Fe-H_2O system at 75°C, with the stability regions for Fe, Fe_2O_3, Fe_3O_4, Fe^{++} and Fe^{+++}. Phase boundaries for 1, 10^{-3} and 10^{-6} molal concentration are shown. 174
7-2 (E, pH)-values for some standard cleaning mixtures. The E values were calculated based on the reduction reaction of the oxidant, assuming standard cleaning solution compositions. For the acid solutions, the pH values are based on the assumption of complete dissociation (strong acid). The pH value for SC-1 was determined by pH measurement. . 176
7-3 The E-pH diagram for the Ca-H_2O system at 75°C. Phase boundaries for 1, 10^{-3} and 10^{-6} molal concentration are shown. 177
7-4 The E-pH diagram for the Cu-H_2O system at 75°C. Phase boundaries for 1, 10^{-3} and 10^{-6} molal concentration are shown 178
7-5 The E-pH diagram for the Cr-H_2O system at 75°C. Phase boundaries for 1, 10^{-3} and 10^{-6} molal concentration are shown. 179
7-6 The E-pH diagram for the Na-H_2O system at 75°C. Phase boundaries for 1, 10^{-3} and 10^{-6} molal concentration are shown. 180
7-7 The Gibbs free energy of a metal ion undergoing incorporation in the silicon oxide, as a function of reaction coordinate. The energy barriers for the forward and reverse reaction are ΔG^* and $\Delta G^* - \Delta G_R$. . . . 183

7-8 Model for the cleaning solution–wafer interface (r=etching speed ; d = oxide thickness ; Φ = flux of contaminant atoms). The contamination is concentrated in the outer layer (thickness a) of the chemical oxide. 186

7-9 Effect of the magnitude of the driving force on the deposition transient. The following model parameters were used : $k_{eq} = \exp(- \Delta G^o_R/RT)$, $c_o = 10^{12}$ atoms/cm^2, a = 2 nm, $\Phi_o = 10^{11}/cm^2$, r=0.01 nm/s. 189

7-10 The total contaminant flux as the sum of deposition (Φ_{dep}) and etching (Φ_{etch}) fluxes. The following model parameters were used : $k_{eq} = 10^4$, $c_o = 20 \cdot 10^{12}$ atoms/cm^2, a = 2 nm, $\Phi_o = 10^{11}/cm^2$. r=0.01 nm/s. 190

7-11 The E-pH diagram for the Al-H_2O system at 75°C, (a) without taking into account silicate formation and (b) assuming the formation of the silicate phase $Al_2O_3.SiO_2$. Phase boundaries for 10^{-3}, 10^{-6}, and 10^{-9} molal concentration are shown. 192

List of Tables

1.1 The evolution of minimum feature size, integration density, gate oxide thickness and clockspeed of silicon ICs. 21

2.1 Present and future standards for chemical purity and surface roughness. 28

2 2 Some common cleaning solution chemistries (DI=deionized water) . . 29

3.1 Purity of Ashland Gigabit^{TM} grade chemicals used for wafer preclean 43

3.2 Pretreatment of quartzware used for experiments. 44

3.3 Pretreatment of teflon beakerware used for experiments. 44

3.4 The MIT clean. 45

3.5 Standard solutions used for controlled contamination experiments. . . 46

3.6 Wafer materials used for controlled contamination experiments. . . . 47

4.1 The determination of the ratio of capture cross sections σ_n/σ_p, band-bending potential ϕ_s^o, and surface charge, Q, from surface lifetime measurements. 79

5.1 Net charge on halogen atom, q_X; net charge on top silicon atom, q_{Si1}; order of bond between top and second layer silicon atoms, n_{12}); and difference in Pauli electronegativity, $\Delta\chi$. All data except $\Delta\chi$ were obtained from single point Hartree-Fock calculations on $Si_9H_{12}X_2$ clusters. 91

6.1 Standard reduction potential, surface lifetime, 1:100 HF exposure conditions, and calculated driving force for the cathodic reaction. 126

6.2 Factors investigated in copper deposition study. 139

6.3 Results of AFM analysis of precipitate density on p and n-type wafers immersed for 5 min. in 1:100 HF solution containing 400 ppb Cu^{++}. . 146

6.4 Cross section for minority carrier capture per copper atom on the silicon surface, for < $10^{10}cm^{-2}$ copper coverage. 150

6.5 The effect of doping type and illumination on the driving force (Δ G, in meV) for the $1/2\ Cu^{++} + e^- \longrightarrow 1/2\ Cu^o$ reaction. A doping level of $10^{15}cm^{-3}$, a light injection level of $10^{13}cm^{-3}$ and 200 ppb Cu^{++} in solution were assumed. The calculation is further based on the measured values for the bandbending on n- and p-type material in the in the dark. 156

6.6 The effect of doping type and illumination on the copper concentration (in ppb) where the driving force, ΔG, vanishes. This calculation was based on the driving force values listed in Table 6.5. 158

6.7 Copper levels of HF solutions, and estimated copper coverage after 5 min. immersion, for solutions used in pregate clean. 167

7.1 The stable ionic or oxide species formed for SC-1 conditions and the experimentally observed deposition tendency. 181

7.2 Standard free energies for the formation of a silicate from the metal oxide and SiO_2. 184

8.1 Typical bulk lifetimes of commercial CZ material (dsp = double side polished; ssp = single side polished) and their influence on the lower detection limit for surface defects, N_{ldl}. 199

Chapter 1

Introduction

1.1 Motivation

The birth of the modern science of surfaces can be traced to the golden age of germanium electronics [1]. After the invention of the point-contact transistor by Shockley, Bardeen and Brattain in 1947, it soon became clear that surface phenomena could drastically influence the electrical characteristics of solid state devices. Starting in the early 1950s, the stabilization of the chemical and electrical properties of germanium surfaces became a hot topic in the nascent field of semiconductor research. Surface states, proposed earlier on theoretical grounds by Tamm [2] and Shockley [3], were first used by Bardeen in 1947 [4] to explain the observed discrepancy between metal work functions and the barrier heigths at metal/semiconductor contacts. The same concept later entered semiconductor textbooks as a convenient link between electrical and chemical processes at the semiconductor surface. In all of the early germanium work, poor crystal quality tended to compromise reproducibility, and lack of sensitive surface analysis tools led to limited understanding of the reaction chemistry. Nevertheless, the foundations were laid for a new field of materials research: semiconductor surface science.

As attempts to achieve stable surface passivation of germanium continued to falter, mainly because of the poor chemical stability of germanium's oxides, the research emphasis shifted to the natural alternative, silicon, by the late 1950s. In less than a

decade, silicon established itself as the material of choice for solid state transistors, a trend which was further strengthened by the discovery of the MOSFET (Metal Oxide Field Effect Transistor) in 1960. Silicon owes its present-day success as an electronic device material mainly to the superior chemical stability of its oxide, SiO_2, and the excellent electrical properties attainable of surfaces carefully prepared by thermal oxidation. The dominant role of silicon in electronics is reflected in its 95 % share of the global semiconductor market.

Today's most advanced microprocessors contain millions of devices (mostly MOSFETs) with features as small as 0.35 μm, and run at clock speeds greater than 250 MHz. The phenomenal progress in integrated circuit (IC) performance during the last three decades is due to a famous industry paradigm. Moore's Law [5], which predicts the doubling of the number of devices per chip every 18 months (Figure 1.1). The migration towards smaller features and larger die sizes confronts the IC industry with some formidable technical and financial challenges, arising from the need to continuously lower defect densities on substrates with increasing diameter.

As feature sizes are scaled down to accommodate higher clock speeds, gate oxide thickness has to be reduced also to avoid increases in power consumption arising from short channel effects[6]. Table 1.1 shows the evolution in gate oxide thickness in subsequent device generations [7]. Since the introduction of VLSI (very large scale integration) in the late 80s, the importance of surface cleanliness for achieving satisfactory device yield and reliability has become clear. Wet wafer cleaning, the most frequently applied process step in IC processing, has become an active research field, with much effort devoted to exploring the relationship between cleaning recipe, residual levels of contaminants, and device performance [8]. Recently, the rapid growth in semiconductoring manufacturing has brought the environmental impact of cleaning operations under scrutiny, making the development of environmentally benign cleaning strategies a priority.

The detrimental effects of metallic contaminants on submicron electron devices are well documented [9], [10]. When present in silicon, heavy metals often form midgap states, which act as efficient generation-recombination centers, increasing the leakage

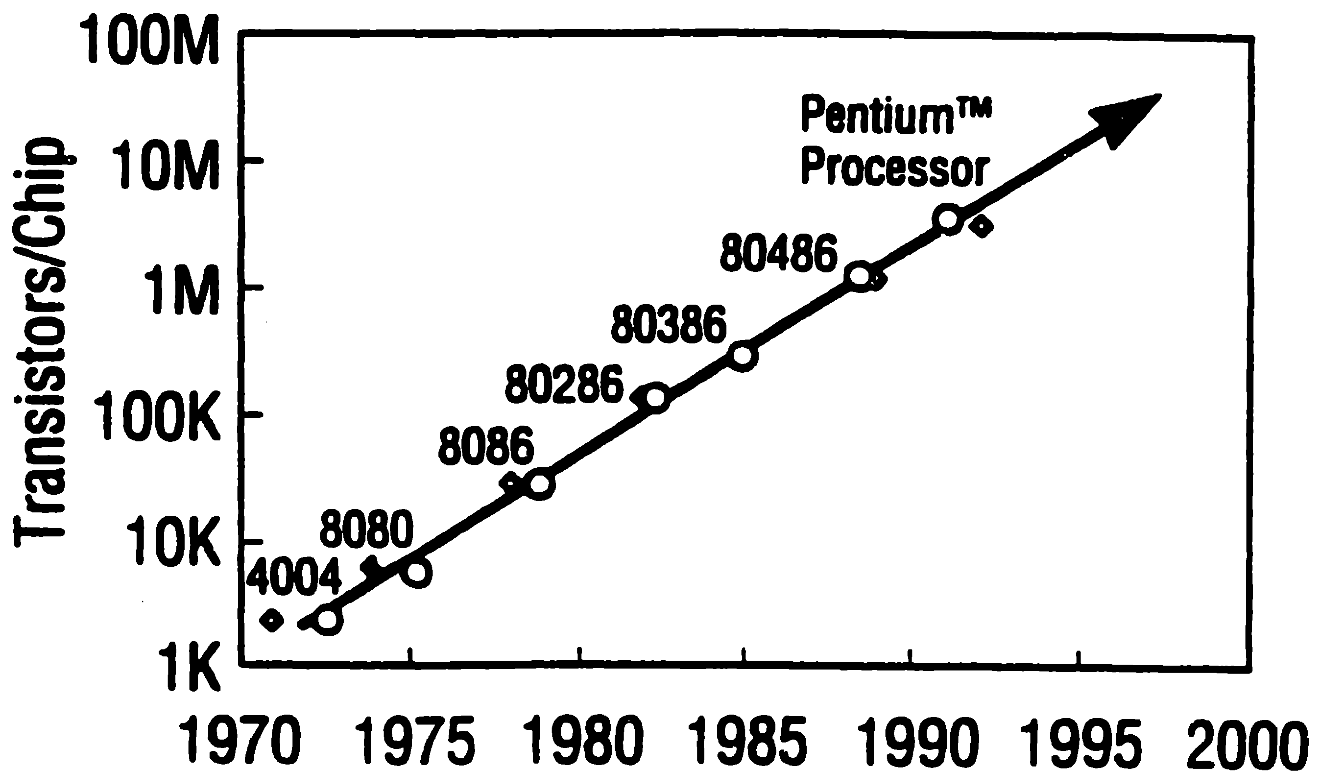

Figure 1-1: Moore's law

first production	1992	1995	1998	2001	2004
minimum feature (μm)	0.5	0.35	0.25	0.18	0.12
gates/chip	300K	800K	2M	5M	10M
gate oxide (nm)	120	90	70	60	45
DRAM size	16M	64M	256M	1G	4G
clock speed (MHz)	120	200	350	500	700

Table 1.1: The evolution of minimum feature size, integration density, gate oxide thickness and clockspeed of silicon ICs.

current of junctions. Due to their high diffusivity and low solubility, they exhibit a strong tendency to precipitate and decorate extended defects, leading to junction shorting and degradation of the gate oxide integrity (GOI). While leakage current increases are most detrimental to charge storage based devices, such as dynamic random access memories (DRAMs) and charge coupled devices (CCDs), degradation of GOI is the most critical yield limiter of today's CMOS logic circuits [11].

It has been projected that metallic surface contamination levels will have to be suppressed below 10^9 atoms/cm^2 to obtain satisfactory device yield for future ULSI (Ultra Large Scale Integration)[7]. Concurrently, a tight control over particulate contamination will continue to grow more important with each subsequent IC generation, as the size of a "killer" particle in photolithography scales with minimum feature size. As cleanliness standards continue to grow tighter, chemisorption of gaseous contaminants from the cleanroom ambient onto the wafer surface is causing increasing concerns as well. Oxygen chemisorption is known to degrade thin film quality in epilayer growth and metallisation processes [12], while chemisorbed organics may severly degrade GOI and epilayer quality [13]. For thin gate oxides (<100 Å), atomic scale increases in surface roughness, have been shown to affect GOI also [14].

1.2 Scope and structure

The research comprised in this thesis is motivated by the need for fast, *in situ* detection of low levels of chemical impurities on the wafer surface during IC manufactur-

ing [15]. Our work addresses the surface chemistry of metals on silicon in wet wafer cleaning solutions and gaseous ambients, and their effect on the surface recombination velocity, an electronic property of the surface. Surface recombination is important because it defines the impact of adsorbates on bulk carrier transport. In this thesis, we propose a novel approach to impurity detection on silicon wafers, based on the measurement of surface recombination by photoconductance decay. Our method allows quantification of surface impurities at levels far below the practical detection limit of state-of-the-art surface analysis tools based on photon-, electron-, or ion spectroscopy. The sensitivity of the photoconductance measurement to surface defects is the result of the extraordinary perfection of the 200 mm diameter silicon material used in today's high volume IC manufacturing.

Chapter 4 of this thesis is devoted to the application of the photoconductance decay technique to surface recombination velocity (SRV) measurements. To ensure accurate quantification of surface defects, an accurate control of carrier injection level is essential. We develop a straightforward model for the effect of injection level on SRV in the presence of bandbending, and verify it using measurements on HF-immersed and oxidized wafers.

To minimize contamination risk during ULSI processes, a rational design of cleaning solutions, based on sound theoretical models for the effect of solution chemistry on impurity removal, is essential. We have developed predictive models for impurity adsorption from the gas and liquid phase. The research addresses two problems:

- Which adsorption reactions are thermodynamically favored, *i.e.*, result in a reduction of the total Gibbs free energy of the system ?
- What are the kinetic barriers associated with the reactions ?

While the solution of the first problem will isolate the adsorption reactions that are energetically possible, the solution of the second problem is generally necessary to correctly predict adsorption behavior. This dual approach will be followed throughout our work.

Chapter 5 covers the chemisorption reactions of oxygen, halogens and metals on a silicon surface passivated by hydrogen (Si-H). We have used *ab initio* electronic structure calculations at the Hartee-Fock level to study the nature of the chemical bond between silicon and the impurity. Based on these calculations, we predict the resistance of various surface termination layers on silicon (100) ar[illegible]tching (in the liquid) and chemisorption reactions (in gaseous ambients). Pho[illegible]uctance decay measurements are used for *in-situ* kinetic studies of these reactions.

Chapters 6 and 7 discuss metallic impurity adsorption from liquid media. The theoretical framework need to describe metal deposition equilibria and kinetic effects depends on the type of cleaning solution. Chapter 6 addresses metal deposition from HF solutions. In these solutions, the surface is passivated by a covalently bound monolayer (mostly hydrogen). Metal ions deposit by reduction from solution:

$$M^{z+} + ze^- \longrightarrow M^o \qquad (1.1)$$

Because of the need to maintain charge balance across the silicon/solution interface, the electrons consumed in the reduction reaction are supplied by the etching of silicon:

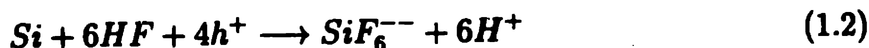

$$Si + 6HF + 4h^+ \longrightarrow SiF_6^{--} + 6H^+ \qquad (1.2)$$

We develop a photoelectrochemical model for the deposition reaction, which demonstrates the effect of doping, illumination, and surface potential on the energetics of these reactions. Copper, a commonly encountered background contaminant with a strong tendency to deposit from HF, receives special emphasis. The important role of surface states in the reduction reaction of copper ions will be discussed.

Chapter 7 discusses metal deposition in oxidizing solutions. Because the chemical oxide which covers the silicon in oxidizing solutions is electrically insulating, direct charge transfer between the semiconductor bands and the cleaning solution cannot occur. The poor electrical quality of the chemical oxide/silicon interface is reflected in a large density of surface states, which dominate recombination behavior of chemical

oxide-covered wafers. Metal deposition from oxidizing solutions occurs by incorporation of the metal oxide into the silicon oxide. We have developed a model for metal deposition from various solutions, which incorporates the thermodynamics and kinetics of metal removal and redeposition. Thermodynamic stability diagrams (E-pH maps) are presented as convenient visual aids for cleaning solution design.

Because metal atoms introduce surface states in the silicon bandgap, they can be detected through their effect on the surface recombination rate at a hydrogen terminated surface. This approach has allowed us to measure, for the first time, the minority capture cross section of a chemisorbed metal atom on a silicon surface. The possibility to detect ultralow levels of surface contaminants ($<10^8$ atoms/cm^2) by minority carrier lifetime measurement is of great practical significance for in line monitoring of wafer surface purity in IC processing.

Finally , Chapter 8 puts the major conclusions of this research in a broader perspective. The ability to detect surface impurities at levels hitherto impossible opens up new opportunities for *in situ* control of surface cleaning. Based on new insights in adsorption chemistry gained from our work we discuss future strategies in cleaning research.

Chapter 2

Cleaning and Surface Preparation for IC Manufacturing

2.1 Introduction

As sizes shrink and junctions become shallower, devices become more sensitive to low levels of chemical impurities and particles. Notably since the advent of VLSI (Very Large Scale Integration), the importance of process cleanliness for achieving high device yield and reliability has been realized. Because of their excellent ability to remove particles, chemical contaminants, and native oxides, wet processes play a central role in wafer cleaning and surface preparation. Today, a typical process flow for advanced ICs consists of 300 to 500 process steps, 30 % of which are wafer cleaning steps. Wafer cleaning equipment also accounts for 20 % of equipment capital cost. Cleaning prior to thermal front-end-of-line process steps, such as gate oxidation, dopant diffusion, and epilayer deposition is especially critical because early introduction of contamination may severly compromise the yield and reliability of finished devices. The purpose of the present chapter is to review some aspects of wafer cleaning technology, relevant to our research. We focus on wet cleaning solution chemistry for preoxidation cleaning. A good general review of wafer cleaning technology can be found in Ref. [8].

2.2 Effects of metallic contamination on device performance

During a high temperature oxidation treatment, a poorly cleaned surface acts as a source of metallic contaminants, which will redistribute themselves between silicon bulk, oxide and the oxidation ambient. The extent of redistribution of a metal depends on its solubility in the silicon and the thermodynamic stability of the metal oxide [16]. Because of their vanishingly small solubility in silicon at low temperature, transition metals in silicon tend to precipitate, or decorate extended defects, upon cooling. The final distribution of the metal after cooling will be determined by its temperature dependent diffusivity and the cooling rate.

The behavior of metals during heat treatment has been studied widely. Iron, for example, readily dissolves in the silicon bulk at sufficiently high temperatures, strongly degrading the bulk lifetime [17]. For sufficiently low cooling rates, Fe_2Si precipitates form in the surface region, degrading the breakdown strength of thin oxides[18]. Aluminum mostly segregates to the oxide, giving rise to surface charge, which may interfere with device operation. Calcium becomes trapped in the oxide as well, increasing the roughness of the Si/SiO_2 interface and degrading GOI [19].

Copper, like most transition metals, is an interstitial diffuser in silicon. Because of its high solubility at elevated temperatures, surface copper readily dissolves in the silicon lattice during thermal treatments [20]. Copper pairs with acceptor atoms, thereby electrically passivating them [21]. Because of its high diffusivity, copper atoms have a high tendency to cluster and form copper silicide precipitates in the surface region during wafer cooling, degrading the surface lifetime and breakdown properties of Si/SiO_2 structures [22, 23, 24].

Verhaverbeke [6] investigated the effect of Ca, Zn, Fe, Cu and Al contamination on the dielectric strength of thermal oxides. The impact of Cu and Zn was found to be marginal compared to Ca, Fe and Al. Liehr *et al.* [25] found that reducible metals can create voids in the oxide layer by catalyzing the decomposition reaction of silicon dioxide during high temperature annealing in an inert ambient.

Once a metal is present in the silicon, its impact on device performance can be minimized by providing 'sinks' for metal atoms in parts of the wafer removed from active device regions, a technique commonly referred to as gettering. Gettering is especially effective for metals with low solubility and high diffusivity such as Ni and Cu. Cr, Mn, Fe and Co have a higher solubility and are much harder to getter [20]. Gettering can occur at oxygen precipitates in the bulk of the wafer (intrinsic gettering) or at deliberately introduced extended defects in the surface region (extrinsic gettering). The use of heavily doped p-type substrate, with higher solubility for donor metallic impurities, is known as segregation gettering [26]. Gas phase gettering using chlorine compounds during hight temperature treatments has also been reported. Unfortunately, the presence of strain and high doping in active device regions may cause them to act as effective getter sites as well, thereby limiting the efficacy of various gettering schemes.

Reductions in gate oxide thickness call for a tighter control of surface impurity concentrations. The surface purity and smoothness requirements for future ULSI generations is summarized in Table 2.1 [7]. While surface iron levels as high as 10^{13} atoms/cm^3 have little effect on the breakdown properties of 200 Åthick gate oxides [18], levels below 1x10^{10} atoms/cm^3 will be required to achieve satisfactory GOI for 45 Åthick gate oxides to be used in the 0.12 μm device generation planned for 2004 [7]. To minimize process risk in USLI and reduce the need for gettering, design of wet cleaning processes for optimum metal removal is highly desirable. Meanwhile, prevention of particle deposition, organic contamination and surface roughening will continue to be important as well.

2.3 The RCA clean

While the development of high-performance cleaning systems is considered crucial for achieving high ULSI process yields, wet wafer cleaning technology has undergone relatively little change during the past twenty years. Indeed, since its introduction by Kern [27] in 1970, the RCA (*Radio Corporation of America*) clean has continued

first production	1995	1998	2001	2004
surface Al, Ca (cm^{-2})	1E11	5E10	2.5E10	1E10
surface Fe, Ni, Cu, Zn. Na (cm^{-2})	5E10	2.5E10	1E10	5E9
bulk metals (cm^{-3})	1E11	5E10	2E10	1E10
surface organics(cm^{-2})	5E14	3E14	1E14	5E13
RMS microroughness (Å)	2	1.5	1	1

Table 2.1: Present and future standards for chemical purity and surface roughness.

to be widely used, with only minor modifications to the solution composition and the cleaning sequence.

Some commonly used wet cleaning solutions are shown in Tabel 2.1. SC-1 [1], the first step of the RCA clean, consists of hydrogen peroxide (H_2O_2), ammonium hydroxide (NH_4OH) and deionized water (DI) (Table 2.1). Because of the high pH, and the slow etching of the chemical oxide, particle removal occurs very effectively in SC-1. Light organics are readily oxidized as well, and certain metals are removed effectively by complexing. Meanwhile, SC-1 typically contaminates the wafers with unacceptable amounts of Al, Fe and Zn [28]. In addition, the slow etching of the chemical oxide leads to slight surface roughening of (100) wafers [29], which has been shown to degrade GOI [14].

SC-2 (hydrochloric acid (HCl), hydrogen peroxide and DI water) is the second step in the RCA cleaning sequence. SC-2 is an acidic cleaning solution, which effectively

[1]SC=Standard Clean

Clean	Chemicals	Mixing ratio	Temperature	Contaminants
Piranha	H_2O_2 (30%) : H_2SO_4 (98 %)	1:4	90°C	organics, metals
SC-1	H_2O_2 (30%) : NH_3 (29 %) : DI	1:1:5	70°	particles, organics
SC-2	H_2O_2 (30%) : HCl (37 %) : DI	1:1:6	70°	metals
DHF	HF (48%) : DI	1:10 to 1:100	25°	native oxides, metals
BHF	HF (48%) : NH_4F (40%)	1:7	25°	native oxides

Table 2.2: Some common cleaning solution chemistries (DI=deionized water)

removes metals, left behind in the SC-1 step, by dissolution. Because of its low pH, SC-2 tends to deposit particles [30].

RCA-type cleaning sequences, which leave the silicon surface passivated by a thin (2 nm) layer of chemical oxide, have long been the standard clean for preoxidation cleaning. Recently, the ability of the RCA clean to meet stringent surface purity standards for ULSI has come under question. The main shortcomings of the RCA clean are:

- the poor particle performance of SC-2;
- the surface roughness introduced in the SC-1 step;
- the high disposal costs associated with the use of concentrated chemicals.

For these reasons, HF- and ozone-based cleans (see next sections) are expected to become more important in future ULSI cleaning.

2.4 HF-based cleaning solutions

2.4.1 Dilute HF

Hydrofluoric acid (HF) plays an indispensable role in silicon processing, principally because of its unique capability to etch silicon dioxide. The etching of SiO_2 is a result of HF's low dissociation constant (K_a = 6.58x10^{-4} mol/l) and the high polarity of the H-F bond, which result in a molecule with a combination of strong nucleophilic and electrophilic properties. Therefore, HF readily inserts between Si and "bridging" O in the silica network, forming Si-F and Si-OH groups. Further reaction lead to removal of silicon as SiF_6^{--}, and oxygen as water[6].

Concentrated HF (48 %) is hardly ever used in its undiluted form. Dilution ratios vary from 1:5 to 1:100. In wet cleaning, dilute HF is virtually always used in combination with a prior oxidizing cleaning step. Exposure to an oxidizing, acidic cleaning solution effectively removes metals by dissolution and organics by oxidation, and grows a thin chemical oxide (2-3 nm) into the silicon. Subsequent immersion in

dilute HF solution quickly dissolves this chemical oxide, together with any remaining metals trapped in it. Because HF leaves the surface oxide free, hydrogen terminated and devoid of most metallic contaminants, HF passivation is widely used for surface preparation prior to epilayer growth, polysilicon deposition, and metallisation processes. Lately, the use of HF-last cleaning cycles for wafer cleaning prior to gate oxidation has also gained popularity.

Surface termination by hydrogen (Si-H) represents a tremendous reduction in reactivity compared to "bare" (unterminated) silicon. Chemisorption of reactive organics and oxygen, while thermodynamically favorable, occurs only slowly on ideal Si-H because the energy barrier associated with H displacement is high.

The nonpolar Si-H bond results in a strongly hydrohobic surface. Because liquid droplets are repelled from the surface, drying of hydrophobic surfaces is very facile; however, particle addition from the liquid is a well known downside of HF-last cycles. Therefore, special wafer drying strategies are needed to minimize particle deposition. Addition of 0.05 % IPA (isopropyl alcohol) to dilute HF appears to improve the particle removal efficiency[31].

Another major concern is the deposition of certain metals, notably copper and the noble metals, by electrochemical reduction from solution. Because the electrons consumed in this process are provided by dissolution of the silicon, metals may also cause surface roughness by localised etching ("pitting"). For this reason, HF solutions need to have extremely low levels of metallic impurities in order to be effective.

2.4.2 Buffered HF

By mixing concentrated HF with ammonium fluoride (NH_4F) in a 1:7 ratio, a buffered solution with pH 4.5 is obtained. Buffered HF (BHF) is also known as BOE, buffered oxide etch. While wet HF etching of thermal oxides has been replaced by dry techniques for small-geometry applications, buffered HF solutions are still widely used in wet cleaning to remove chemical and native oxides. Because of its high pH, BHF etches SiO_2 more rapidly than does DHF; meanwhile, the presence of HF_2^- gives rise to anisotropic etching of silicon (111) surfaces, resulting in surface roughening of (100)

wafers by (111) facet formation [32]. The same etching reaction leads to atomically smooth surfaces with highly perfect monohydride termination on (111) silicon. The use of BHF instead of DHF for hydrogen passivation prior to epilayer deposition has been shown to improve epilayer quality on (111) wafers, because the chemisorption of organics from the ambient air is reduced compared to dilute HF passivation [13]. Like DHF, BHF readily deposits certain reducible metals and a tight control over trace metallic impurities in the cleaning solution is essential.

2.5 The Piranha clean

The standard piranha clean (also known as Caro etch) consists of 3 parts sulphuric acid and 1 part hydrogen peroxide, heated to 90 °C. Because of its high oxidizing power, piranha grows a thick (3 nm) chemical oxide, while effectively removing organics by oxidation, and metals by dissolution. The use of piranha followed by dilute HF has been proposed for pre-gate cleaning cycles [31]. Effective metal removal results from the combination of a "deep" wet oxidation by piranha with an HF dip that dissolves the chemical oxide together with any trapped contaminants.

A downside of the piranha clean is the high viscosity of the concentrated sulphuric acid mixture, which makes thorough DI rinsing necessary, in order to avoid particulate contamination from drying residues. An advantage of the piranha clean over SC-2 is that sulphuric acid can more easily be obtained in high purity grades than hydrochloric acid. A modified version of the piranha clean is part of the standard precleaning sequence used in this work (see Section 3.6).

2.6 New approaches and future trends

As wafer cleanliness and smoothness requirements continue to grow tighter, the ability of the RCA clean to satisfy future cleaning needs has come under question, and alternate wet cleaning solutions, such as HF/ H_2O_2 [33], and slight etch (HF/HNO_3) [34] have been proposed. While these solutions possess excellent metal removal char-

acteristics, they do give rise to slow etching of the silicon. Other novel cleaning approaches include the use of complexants to improve metal removal in SC-1 [35], and the growth of ultraclean chemical oxides using ozonized DI water [36].

There has been considerable interest in vapor phase and dry cleaning techniques recently. Notably for specialized cleaning jobs between process steps, such as the pre-silicide and pre-emitter clean, vapor phase cleaning techniques are popular [37], because they can be carried out in a cluster tool with reduced chemicals consumption. Recently, dry chemistries have been proposed which are able to remove metals from the wafer surface quite effectively [38]. Dry cleaning methods are scheduled to be introduced for the pre-metal contact and pre-gate cleans in the 0.25 μm technology, projected for first production in 1998 [7]. Since efforts to achieve gas-phase particle removal have met with limited success, the continued use of wet cleaning cycles, and notably SC-1, for effective particle removal seems inevitable in the near future.

Finally, cleaning effectiveness does not solely depend on cleaning recipe, but is obviously influenced by the purity of the chemicals used, as well as by the cleaning equipment and the drying technique. In addition, the effect of contaminants on device performance may depend on the details of the processing and even on the characteristics of the starting material. Because of the high purity of the chemicals in use today[2], contamination of the solutions by cleaning equipment is becoming more important. Therefore, intelligent design of cleaning equipment to avoid process contamination is expected to receive more emphasis in future cleaning research.

[2]A specified impurity content of <1 ppb for most metallic elements is the industry standard for submicron processes; ultraclean chemicals with less than 10 ppt (part per trillion) individual impurities are already being used today for the most advanced processes.

Chapter 3

Experimental Techniques and Analysis Methods

3.1 Introduction

The extremely high purity demands of the submicron IC industry necessitate the extensive use of state-of the-art analysis techniques for in-line control of process cleanliness during IC manufacturing. As reductions in feature size further tighten purity standards, the number of surface analysis techniques capable of impurity identification in the required sensitivity range (Table 2.1) has become quite limited. For surface metals. total internal reflection x-ray fluorescence (TXRF) is in wide current use. TXRF is capable of identifying most heavy metals on wafer surfaces with detection limits between 5x10^9 and 10^{11} atoms/cm^2, depending on the element and the brightness of the X-ray source. Since a detection limit three times lower than the level to control is a prerequisite for effective monitoring of surface purity[7], sensitivity of TXRF will need to be improved in order to remain useful as a metrology tool.

Impurity detection in bulk chemicals with sub ppb (part per billion) detection limits is routinely possible using well-established instrumental analysis techniques, such as atomic absorption spectroscopy (AAS) and inductively coupled plasma mass spectroscopy (ICP-MS). Collecting surface metals from the wafer surface by scanning an appropriately formulated droplet across the wafer surface, allows the excellent

sensitivity of bulk liquid analysis techniques to be extended to surface analysis of wafer materials. Another application of the droplet scan method is to concentrate all impurities in the centerspot of the wafer, for subsequent analysis by TXRF. In this way, the sensitivity of TXRF can, in principle, be boosted by several orders of magnitude. The accuracy of this approach has been questioned, however, because the collection efficiency may vary depending on the chemical state of the metal on the surface, especially so for copper and the noble metals.

As reductions in feature size further tighten purity standards, existing analysis methods are pushed to their limits and the need for new detection schemes arises. Because metallic impurities often form electrically active defects in the bandgap [39], their presence in the semiconductor bulk can be detected by electrical measurement of material or device properties. Especially noncontact techniques that measure minority carrier lifetime or diffusion length have found widespread application in the semiconductor industry for rapid in-line detection of bulk metallic contamination. While usually not capable of elemental identification, these electrical techniques offer the advantage of speed, sensitivity, and noninvasiveness over conventional surface analysis techniques.

3.2 Total reflection X-ray fluorescence (TXRF)

Total reflection X-ray Fluorescence is based on the same principles as traditional bulk X-ray fluorescence methods, but uses an X-ray beam incident incident on the sample at a glancing angle so that the condition for total external reflection is met [40, 8, 41]. In practice, X-rays penetrate a few nm into the sample, primarily because of the divergence of the X-ray beam. Penetration depth also depends on glancing angle, energy of the primary X-rays, sample bulk composition, and surface roughness. As a result of the shallow penetration of the X-rays, the sensitivity for metallic impurities residing in the thin surface layer is greatly increased compared to conventional XRF.

A schematic view of the basic configuration is shown in Figure 3.1. A rotating anode (W or Mo) in combination with a monochromator is used as an X-ray source.

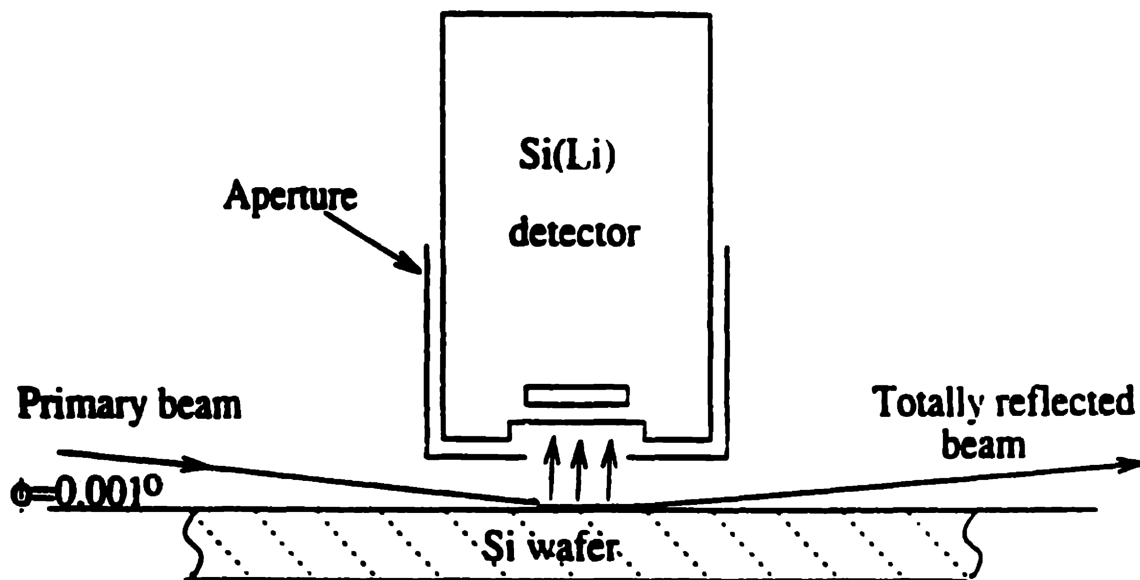

Figure 3-1: Operating principle of total reflection X-ray fluorescence (TXRF).

A Si(Li) detector collects X-rays from a 10 mm diameter surface region and is used as energy dispersive spectrometer (EDS). A TXRF spectrum is a graph of fluorescence energy (0 to 18 keV for Mo primary beam) vs photon count per second (Figure 3.2). For analysis of silicon wafers, the large peak at the low energy end of the spectrum is the silicon signal from the wafer substrate. High counts at the high energy end of the spectrum are due to scattered primary X-rays (Mo K_α) Characteristic x-ray peaks of elements S through Br (K_α) and Rb through Bi (L_α (Mo source) have energies between the silicon peak and the high-energy scatter. Quantification is achieved by analyzing a sample with known contamination level of one element and calculating areal densities for unknown samples using sensitivity factors related to well known relative fluorescence yields for the elements.

3.3 Atomic force microscopy (AFM)

3.3.1 Principle of operation

AFM is a one of the better known members of the family of imaging techniques collectively referred to by the term Scanning Probe Microscopy (SPM). Its oldest member, STM (Scanning Tunelling Microscopy), was invented by Binnig and Rohrer in 1981[42]. In its most straightforward form, STM images the tunneling current between a sharp metallic tip and a conducting sample (Figure 3.3). Because the tunneling occurs at an atomically sharp protrusion on the tip, STM has atomic resolution.

In conventional (or contact mode) AFM, a flexible cantilever with a sharp tip on the downward facing side is scanned over the sample surface while its deflection is monitored using a laser beam and position sensitive photodetector. The deflection signal is read into a feedback loop which acts to keep the distance between the tip and the sample surface constant by means of piezoelectric transducers. When the tip is brought sufficiently close to the sample surface, interatomic forces between the tip and the surface atoms will cause the cantilever to deflect. The feedback allows

File: MN1-0000

Sample: Slot 1 | Date: 3/4/96 1:02:32 PM
Operator: RHB | Sub.: Si WAFER
Memo1: MIT/Norga CFA #13491
Memo2: T937

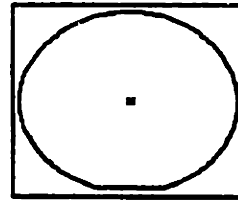

Slot: 1 | M. Spot | X-ray | D.P. Cond.:T
Size: 6 inch | X: 0.00 mm | Voltage: 40 KV
Time: 1000 sec | Y: 0.00 mm | Current: 40 mA | Element Cond.:M-AU
D.T.: 2.72% | Angle: 0.050 deg | TARGET: Mo | Quant. Cond.:W-111

Spectrum	Energy keV	Peak Int.cps	Conc. *E10	BG.Int. cps
Mo-Kal	17.44	242.6723		
Si-Ka	1.74	168.8561		0.7864
S -Ka	2.31	0.0861	666.29	0.6889
Ca-Ka	3.69	0.0882	101.69	0.4469
V -Ka	4.95	0.0334	24.54	0.2852
Cr-Ka	5.41	0.0157	8.59	0.2621
Fe-Ka	6.40	0.0883	22.14	0.2366
Ni-Ka	7.47	0.0413	8.60	0.1980
Zn-Ka	8.63	0.1063	14.71	0.1779
Br-Ka	11.91	0.5291	34.86	0.2408
Au-La	9.71	3.0996	134.07	0.1854

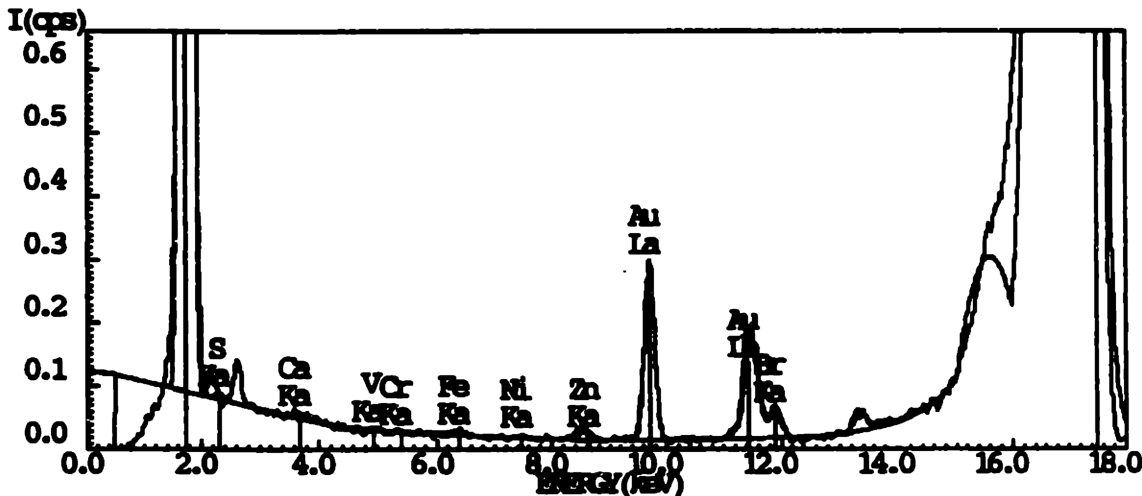

Figure 3-2: TXRF spectrum of a gold contaminated wafer

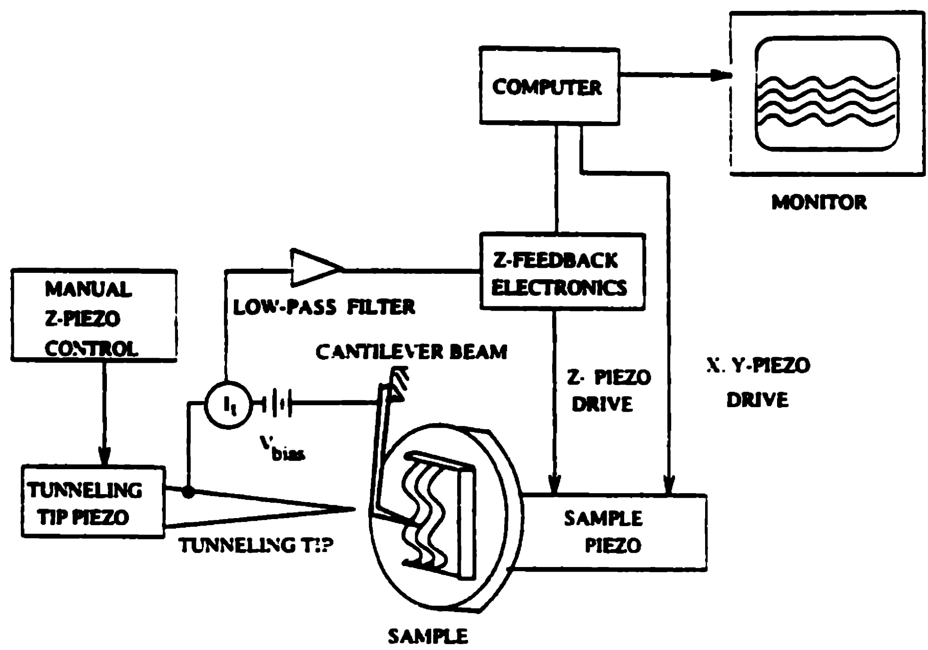

Figure 3-3: Operating principle of scanning tunneling microscopy (STM).

the tracking of surface features without intimate physical contact between the surface and the tip. By imaging the height information from the piezo a topographic image is obtained.

A recent innovation is so-called "tapping mode" AFM (TMAFM), which further reduces the physical contact between the AFM tip and the sample. In TMAFM, the tip is oscillated near its resonance frequency. Because the amplitude of the tip oscillation is damped by interatomic forces between the tip and the sample as the surface is approached, this amplitude can be used as an alternate feedback signal for the tracking of surface topography.

3.3.2 Quantification of metallic precipitates using AFM

While AFM is well established as an in-line tool for surface roughness and topographical measurements on silicon wafers, its use for obtaining quantitative information regarding the presence of low amounts of metallic contamination is relatively new [43, 44]. An obvious drawback of the AFM technique is the absence of elemental identification. In this thesis, we have used AFM for measuring the density of copper precipitates on silicon wafers. Because AFM does not allow elemental identification, copper precipititates could not be distinguished from similarly sized particulate contaminants, possibly present on the wafer surface. With this in mind, we have performed elaborate AFM studies on blank control wafers, to assess the likelihood of including non-copper particulates during the precipitate counting.

Control wafers were cleaned and exposed to blank HF solution. TXRF analyses revealed copper levels below the detection limit ($< 5 \times 10^9$ atoms/cm^2). AFM images of the control wafers consistently revealed smooth, particulate-free surfaces with very low RMS roughness values (0.15 - 0.20 nm for 1x1μm image size). Since all the wafers from the experimental set were exposed to the same process steps as the blanks (apart from the presence of copper in the contaminated solutions), these observations made us confident that the AFM counts of copper precipitates were not biased by the presence of particulate contamination.

In this research we used a Nanoscope III AFM with Dimension 3000 analysis soft-

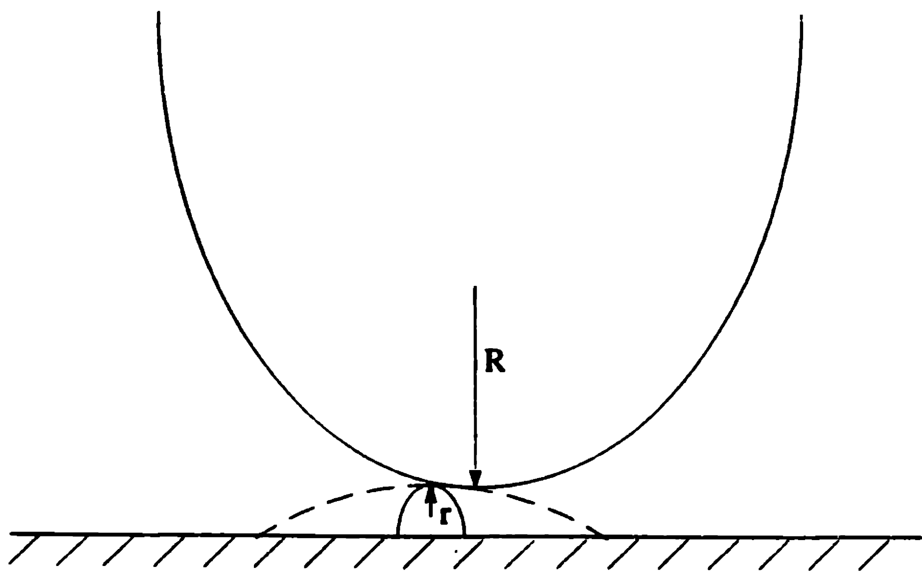

Figure 3-4: The effect of tip radius when imaging tall features on an otherwise smooth surface.

ware (Digital Instruments, Santa Barbara, CA) at the Center for Materials Science and Engineering at MIT. We used the instrument in Tapping Mode^{TM}, using silicon tips. This instrument allows measurements on whole wafers up to 200 mm diameter in size. Precipitate densities were counted using the grainsize analysis algorithm, which counts the total number of surface features with heights greater than a chosen threshold value. The low roughness ($\approx$ 0.20 nm) allows accurate counting of precipitates with heights as small as 1 nm.

The height resolution of AFM is similar to STM (0.1 Å), while its lateral resolution is considerably less (1 nm). Features much smaller than the tip radius will be imaged with enlarged lateral dimensions (Figure 3.4). For precipitates on an otherwise smooth surface, a hemispherical precipitate with radius r will be imaged as a lens-shaped feature with height r and radius approximately r + R (R = tip radius). Since the tip radius, R, is not known accurately, we have consistently assumed hemispherical precipitates with radius equal to the measured precipitate height.

3.4 Liquid chemical analysis

3.4.1 Graphite furnace atomic absorption spectroscopy

Graphite furnace atomic absorption spectroscopy (GFAAS. also known as electrothermal atomic absorption spectroscopy), is a relatively recent modification of the well known AAS (atomic absorption spectroscopy) technique [45]. Instead of a flame, a graphite furnace is used as the sample cell. The free atoms absorb radiation focused on the cell from an external source. As in all absorption spectroscopic methods, the incident radiation absorbed by free atoms in moving from the ground to an excited state provides the analytical data.

GFAAS allows determination of trace metallic impurities in liquid smaples down to part-per-billion (ppb) and even part-per-trillion (ppt) levels. Multi-element analysis is relatively slow because each element must be calibrated for and analyzed idependently. In our experiments, we used a Perkin Elmer 5100 PC GFAAS instrument, located in

the Central Analytical Facility of Digital Equipment Corporation (DEC) (Hudson, MA).

3.4.2 Inductively coupled plasma mass spectroscopy

Inductively coupled plasma mass spectroscopy (ICP-MS) uses an inductively coupled plasma to generate ions that are subsequently analyzed by a mass spectrometer [46]. The plasma is a highly efficient ion source which allows detection limits below 1 ppb. Under ideal conditions, detection limits of a few tens of part per trillion (ppt) are possible for most elements.

Typical applications of ICP-MS in the IC-industry include trace element determinations (up to 80 elements) on ultrapure acids, bases, oxidizers, water, photoresists and organic solvents; and analysis of micro-samples obtained from wafer surfaces using VPD (vapor phase decomposition). A Fisons Plasma-Trace 1 High Resolution ICP-MS, also at DEC, was used in our analysis work.

3.5 Wafer surface preparation procedure

3.5.1 Chemicals

To ensure sufficiently low background levels of metallic impurities in the contamination experiments, we used very high purity chemicals for all the experimental work. The chemicals were Gigabit^{TM} grade, (Ashland Chemical (Dublin, OH)) and are specified to contain less than 1 ppb of most metallic impurities, as shown in Table 3.2. The DI water was 18 MΩcm, obtained from a Modulab DI polishing unit.

Impurity(ppb)	Au	Cu	Fe	Na	Ni	Zn	Cl
HF, 48%	< 1	<1	<1	<1	<1	<1	<10
H_2SO_4, 98%	< 1	<1	<1	<3	<1	<1	<100
H_2O_2, 30%	<1	<1	<1	<1	<1	<1	<30

Table 3.1: Purity of Ashland Gigabit^{TM} grade chemicals used for wafer preclean

3.5.2 Beakerware

All the wafer surface preparations were performed wafer by wafer in high purity containers to avoid contamination by impurities leached out from the beakerware[26]. For HF solutions and DI rinse, we used PFA (perfluoroalkoxy) tanks manufactured by Fluoroware (Chaska, MN). Piranha cleaning was performed in high purity (semiconductor grade) fused quartz containers. Both quartz and teflon were thoroughly cleaned before use [47], as shown in Table 3.3 and 3.4. HNO_3 and HCl for the container cleans were Megabit^{TM} (10 ppb) grade; organic solvents were JT Baker Electronic Grade.

DI water rinse
Trichloroethylene (TCE)
Isopropyl alcohol
DI rinse
HCl/HNO_3 (1/3)
DI rinse
HF .5% (max. 2 min)
DI water rinse
HNO_3 5%
DI rinse

Table 3.2: Pretreatment of quartzware used for experiments.

$H_2SO_4/H2O_2$ at 70°C
DI rinse
HCl/HNO_3 (1/3)
DI rinse

Table 3.3: Pretreatment of teflon beakerware used for experiments.

3.5.3 Cleaning recipe

The MIT clean consists of 2 minutes in dilute (1:100) HF, a 10s DI rinse, followed by immersion in hot piranha H_2SO_4/H_2O_2 at 70°C for 4 minutes. The purpose of

the first cleaning step is to remove any native oxides, while the second step grows a 2-3 nm thick chemical oxide, which traps any contaminants present in the top silicon layer.

Clean	Chemicals	Mixing ratio	Temperature	Duration	Rinse
DHF	HF (48%) : DI	1:100	25°	2 min.	10 s
Piranha	H_2O_2 (30%) : H_2SO_4 (98 %)	1:4	90°C	4 min.	1 min.
DHF	HF (48%) : DI	1:100	25°	2 min.	10 s

Table 3.4: The MIT clean.

After the piranha step, the wafer is thoroughly rinsed in DI for 1 minute, followed by immersion in dilute (1:100) HF for 2 minutes.

3.5.4 Controlled contamination

We use standard solutions with a precisely known concentration of a specific ion to obtain controlled, low concentrations of metallic ions in HF solution. We used both AAS standard solutions (Alpha Aesar Specpure) and ICP-MS standard solutions (Aldrich Chemical co.). Table 3.4 summarizes the types of solutions used in the various experiments where wafers were immersed in deliberately contaminated solutions.

Volumetric amounts of the standard solutions were added to the cleaning solution using Fischer Scientific Digital Micropipettes (1-10 ml, 40-200 μl, 5-50μl). For certain experiments intermediary dilutions were prepared in 50 ml pyrex flasks.

Element	Standard solution	Concentration	Matrix
Cu	ICP-MS	10,000 μg/ml	≤ 2 wt % HNO_3
Cu	AAS	1000 μg/ml	1 wt % HNO_3
Fe	AAS	1000 μg/ml	1 wt % HNO_3
V	AAS	1000 μg/ml	5 wt % HCl; 0.5-1 % HAsc
Au	AAS	1000 μg/ml	20 wt % HCl

Table 3.5: Standard solutions used for controlled contamination experiments.

3.6 Wafer material

To prevent material variations from affecting the measurement results, most experiments were carried out using a limited number of wafer types. All wafers were we prime type. A limited number of experiments were carried out using double side polished wafers (Type I and II).

Type	Doping	Size	Thickness (μm)	Resistivity (Ωcm)	Bulk lifetime τ_{bulk}	Vendor
I	n	125 mm	625	10-25	> 5ms	SEH
II	p	150 mm	675	10-15	>6ms	SEH
III	p	200 mm	725	20-40	>10ms	MEMC
IV	p	100 mm	575	10-20	$\approx$ 100μs	MEMC

Table 3.6: Wafer materials used for controlled contamination experiments.

Chapter 4

Surface Recombination of Photoexcited Carriers

4.1 Introduction

Carrier lifetime measurement is one of the oldest characterization methods in semiconductor science. Its origins can be traced to the early 1950s, when the nascent bipolar transistor technology called for the development of a new characterization technique with direct relevance to device performance. The success of the MOSFET, which gradually replaced bipolar transistors for IC applications in the ensuing decades, shifted interests from bulk lifetime measurements to MOS-CV characterization of the Si/SiO_2 interface. However, since the advent of VLSI, increases in the number and complexity of IC processing steps have created a need for fast, noninvasive monitors to replace MOS-CV measurements, which require time consuming fabrication of capacitor structures. The timely development of non-contact lifetime techniques with optical carrier excitation has again lead to their widespread use for in-line process control in IC manufacturing.

Lifetime is the most important quality metric for semiconductor silicon. Depending on the measurement method, lifetimes can be classified as *recombination* or *generation* lifetimes. The recombination lifetime τ_r is the average time it takes excess carriers to recombine, after injection by a forward biased pn junction or by light. The

generation lifetime is a measure for the carrier generation rate in the space charge region. Both quantities are related, and have a pervasive impact on device operation. Recombination lifetime controls the efficiency of a solar cell material, while generation lifetime determines DRAM refresh time, junction leakage in bipolars, and power consumption in MOSFET devices. In this research, we focus on recombination lifetime measurements using the photoconductance decay technique [48].

At present, lifetime techniques are in wide use for in-line detection of metallic contaminants [49]. Because they detect impurities through their effect on recombination time of excess carriers, they can detect impurities well below the detection limits of conventional analysis methods, based on spectroscopy. Lifetime measurements are fast and noninvasive; in addition, they measure a quantity which is directly related to device performance. Meanwhile, lifetime measurements do not normally allow identification of contaminants, only detection [1]. Impurities which do not introduce deep levels cannot be detected. Measurements on oxidized wafers only provide information on the density of states near midgap; no direct information can be obtained on oxide breakdown behavior, the main determinant of MOS device yield.

Surface recombination controls lifetime results obtained by the photoconductance decay technique. In the past, surface recombination was mostly viewed as a complicating factor in the measurement of bulk lifetime, and much effort has been aimed at eliminating its contribution by passivating surface defects which act as recombination centers for excess carriers. For the first time, this research focuses on the measurement of surface recombination itself, using the radio frequency photoconductance decay (RFPCD) method. Because chemical impurities often introduce surface recombination centers, RFPCD can be used as a sensitive probe for surface impurities and for *in situ* studies of chemical processes at the silicon surface.

The basics of minority carrier lifetime measurement have been covered in depth by Orton and Blood [52] an Schroder [53]. Excitation wavelength, surface charge, and injection level all affect the photoconductance decay measurement. In this chapter, we

[1] Analysis of the dependence of carrier lifetime on injection level [50] or temperature [51] can be used to determine the energy position of recombination centers in the gap.

establish the theoretical basis for achieving accuracy and reproducibility when studying surface processes using the photoconductance decay method. We present a new model for the effect of injection level and surface charge on the RFPCD measurement, which is supported by experiments.

4.2 Background

4.2.1 The effect of injection level on recombination rate

The recombination of excess carriers in semiconductors can occur by three basic mechanisms (Figure 4.1) [54]. The first mechanism, radiative recombination (Figure 4.1a), is of great importance in direct gap semiconductors. In indirect gap materials such as silicon, this recombination mechanism can usually be neglected, because conservation of crystal momentum requires the simultaneous absorption or emission of a phonon, a low probability process (Figure 4.2).

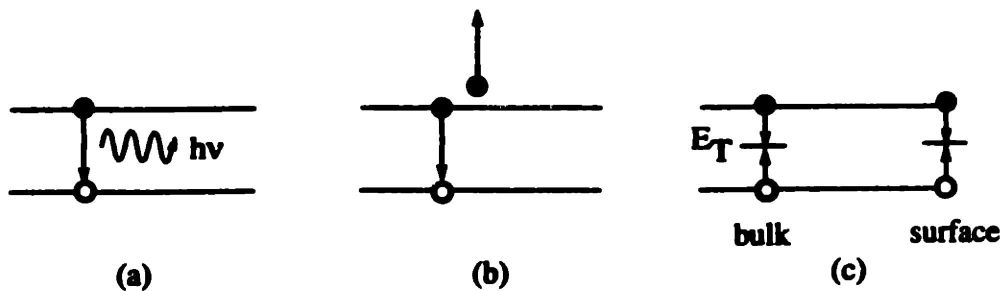

Figure 4-1: Three basic mechanisms for excess carrier recombination in semiconductors: (a) radiative; (b) Auger and (c) recombination via a deep level (Shockley-Read-Hall).

The radiative recombination rate in silicon is given by:

$$\tau_{rad} = \frac{1}{B(p_o + n_o + \Delta n)} \tag{4.1}$$

Where B, the radiative recombination coefficient, equals $2\text{x}10^{-15}$ cm^3s^{-1} for silicon.

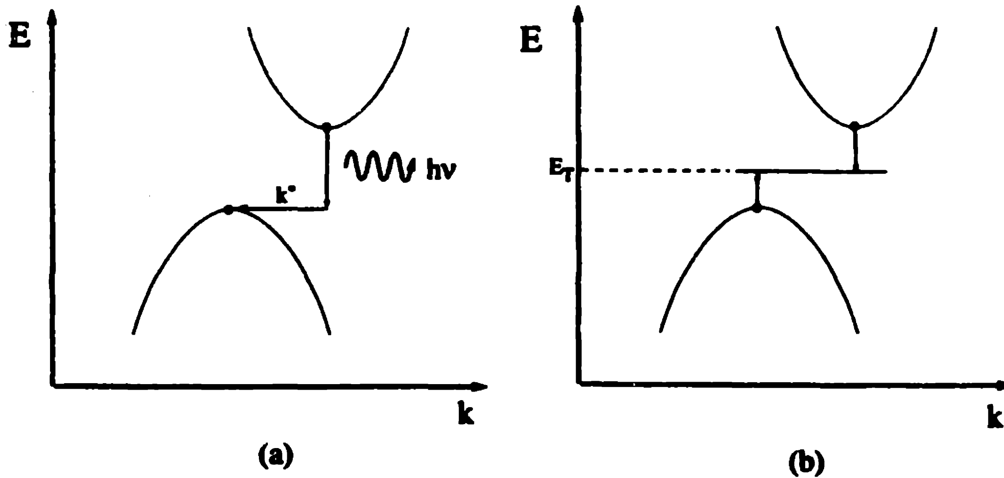

Figure 4-2: Two recombination modes for excess carriers: (a) band-to-band recombination with simultaneous emission or absorption of a phonon and (b) recombination via a deep level (Shockley-Read-Hall).

The second mechanism, Auger recombination, involves three carriers. The energy released by the electron-hole recombination is transferred to the third carrier (Figure 4.1b). This mechanism is only important when the excess carrier density is large. The Auger recombination lifetime is given by:

$$\tau_{Auger} = \frac{1}{C(p_o + \Delta p)^2} \tag{4.2}$$

where C, the Auger recombination coefficient, equals $2\text{x}10^{-30}$ cm^6s^{-1} for silicon [55].

The third mechanism is dependent on the presence of deep energy levels in the bandgap, which may arise from bulk or surface defects. Because localised deep levels are delocalised in k-space, they can effectively capture carriers from both bands, thereby annihilating them (Figure 4.1c). This mechanism is commonly associated with the names Shockley, Read, and Hall (SRH), whose phenomenological treatment of carrier recombination statistics has become a semiconductor literature classic [56, 57].

On phenomenological grounds, the average lifetime of excess carriers τ can be related to the density of impurities N_T assuming that each impurity atom introduces

a single deep state in the bandgap [54]:

$$\tau = \frac{1}{\sigma v_{th} N_T} \tag{4.3}$$

where v_{th} is the mean thermal velocity of minority carriers and σ is the capture cross section.

The principal conclusion of the SRH model is the dependence of the bulk lifetime on the excess minority carrier concentration, Δn, by the expression:

$$\tau_{SRH} = \frac{\tau_{po}(n_o + n_1 + \Delta n) + \tau_{no}(p_o + p_1 + \Delta n)}{p_o + n_o + \Delta n} \tag{4.4}$$

where n_o and p_o are the equilibrium carrier densities and p_1 and n_1 are defined by:

$$p_1 = N_v exp\left(-\frac{E_1 - E_v}{kT}\right) \tag{4.5}$$

$$n_1 = N_c exp\left(-\frac{E_c - E_1}{kT}\right) \tag{4.6}$$

where E_1 is the energy level of the defect, and E_c and E_v are the energy of the conduction and valence band edge, respectively. The SRH model assumes that the bands are flat at the surface, and therefore the excess carrier concentrations at the surface are equal to their values in the bulk ($\Delta n = \Delta n_s$). The surface recombination velocity, s, is defined as the proportionality constant between the surface recombination rate R ($cm^{-2}s^{-1}$) and the excess minority carrier concentration at the surface, Δn_s:

$$R = s \cdot \Delta n_s \tag{4.7}$$

The decay of a nonuniform distribution of excess minority carriers can be expressed as the sum of a fundamental decay mode and higher order decay modes (see section 4.2.4) [52]. If s is small, the time constant of the fundamental mode is given by:

$$\frac{1}{\tau_{eff}} = \frac{1}{\tau_b} + \frac{2s}{d} \quad (4.8)$$

Similar to the bulk lifetime, the surface recombination velocity is injection level dependent :

$$s = \frac{s_n s_p (p_o + n_o + \Delta n)}{s_p(p_o + \Delta n + p_1) + s_n(n_o + \Delta n + n_1)} \quad (4.9)$$

If we assume (for p-type silicon) that $p_o >> p_1$, which is generally true for deep defect centers in the lower half of the energy gap, then the above equations reduce to $s=s_n$ and $\tau = \tau_n$ for the low level injection limit ($\Delta n << N_A$). For high level injection ($\Delta n > N_A$), we obtain:

$$\tau = \tau_n + \tau_p \quad (4.10)$$

$$s = \frac{s_n s_p}{s_p + s_n} \quad (4.11)$$

Radiative, Auger and SRH recombination occur in parallel in the bulk. Hence, τ_b is given by:

$$\frac{1}{\tau_b} = \frac{1}{\tau_{rad}} + \frac{1}{\tau_{Auger}} + \frac{1}{\tau_{SRH}} \quad (4.12)$$

The effective lifetime is given by:

$$\frac{1}{\tau_{eff}} = \frac{1}{\tau_{rad}} + \frac{1}{\tau_{Auger}} + \frac{1}{\tau_{SRH}} + \frac{2s}{d} \quad (4.13)$$

This effective lifetime is the lifetime measured in the photoconductance decay technique. Optimum sensitivity to bulk defects is obtained when τ_{SRH} and s are minimized with respect to τ_{rad} and τ_{Auger}. For an indirect gap material, this condition is easily satisfied by employing low injection levels and by passivating the surface to minimize s during the measurement.

The review presented in this section shows that in the SRH analysis, the descrip-

tion of surface recombination is completely analogous to bulk recombination. In later sections of this chapter, we will see that a complete description of surface recombination requires taking into account the effect of surface charge, an effect which has no bulk counterpart.

4.2.2 Principle of operation of radio-frequency photoconductance decay

System layout

Radio frequency photoconductance decay is an *in situ method* for measuring minority carrier lifetimes. The basic operating principle is shown in Figure 4.3 [26].

The 50 MHz rf signal is generated by a voltage controlled oscillator (VCO) and broadcast onto the wafer by a coil. The reflected signal, caused by eddy currents, is proportional to the conductance of the wafer. A coupler separates the reflected from the incoming signal; the reflected signal is then mixed with the reference signal using a double balanced mixer (DBM). The output signal is obtained from an operational amplifier (OP) which filters out the second harmonic at 100 MHz arising from the mixer and amplifies the signal's dc component. The dc component depends on the amplitudes of the reference and the reflected signal as follows:

$$V_{out} = \frac{V_o V_r cos(\phi)}{2} \tag{4.14}$$

where V_o and V_r are the amplitudes of the reference signal and the reflected signal, respectively, and ϕ is their phase difference.

The phase shifter is used to set the reference and reflected phase difference to 0° when the pulsed light is off. Thus, the signal at the output of the op amp is the component of the reflected signal, in phase with the reference branch. As a result of excess carriers, both phase and amplitude of the reflected signal undergo small changes. Because ϕ was set to 0 to start with, the phase factor in Equation 4.14 remains equal to 1 to first order, and small changes in V_r translate in proportional

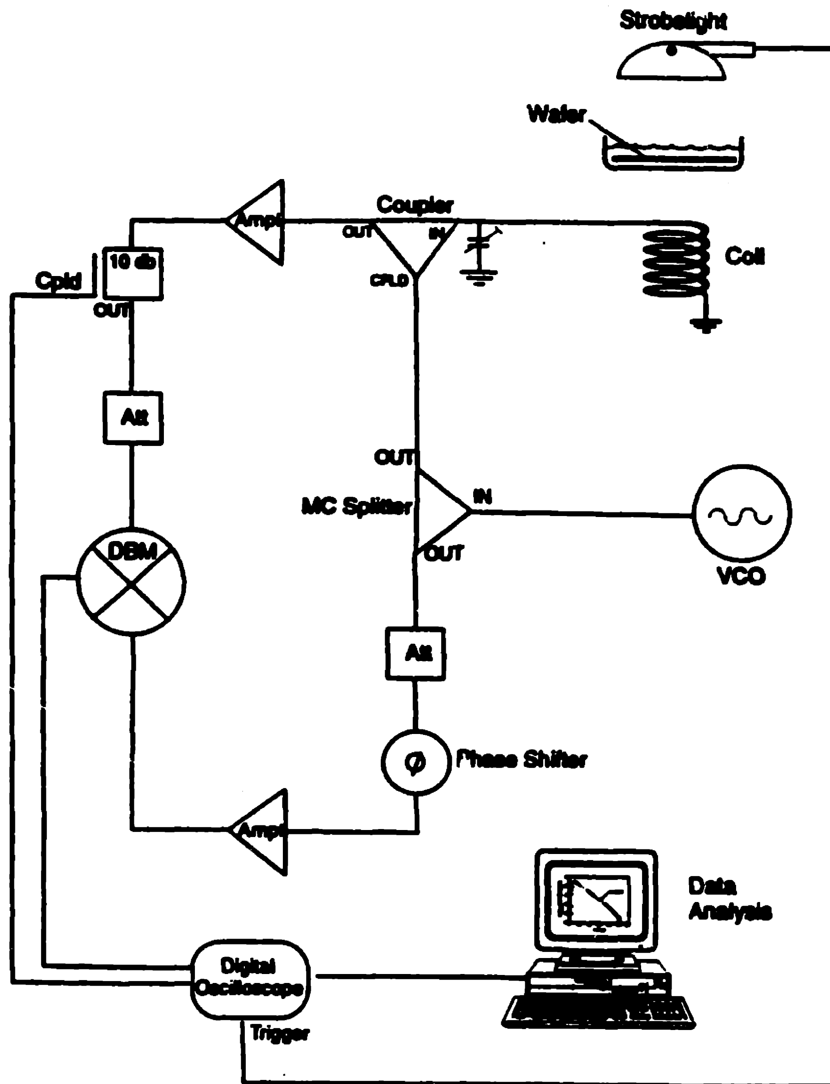

Figure 4-3: The operating principle of radio-frequency photoconductance decay.

changes in V_{out}.

Injection level effects

The reflected signal depends on the excess conductance ΔG of the wafer as follows:

$$\Delta V_r \propto \frac{d\sqrt{R}}{dG}\Delta G \tag{4.15}$$

where R is the power reflection coefficient. ΔG is proportional to the injection level Δn.

According to (4.14), we also have:

$$\Delta V_{out} \propto \frac{d\sqrt{R}}{dG}\Delta G \tag{4.16}$$

The term $\frac{d\sqrt{R}}{dG}\Delta G$ represents the coupling between the wafer and the coil. $\frac{d\sqrt{R}}{dG}\Delta G$ may be assumed to be constant for small ΔG, and depends on the wafer-coil distance and the dielectric properties of the medium in which the wafer is measured. A calibration step is required to determine the proportionality constant between ΔV_{out} and ΔG or Δn for fixed measurement conditions. Nonlinearities between ΔV_{out} and Δn can occur because of the following effects:

- High level injection ($\Delta n >$ doping density), resulting in a dependence of mobility on Δn.
- For large changes in G, $\frac{d\sqrt{R}}{dG}$ will vary with Δn.
- Large variations in G will cause large changes in the phase factor in Equation 4.14, leading to nonlinear behavior.

In all our measurements, efforts were undertaken to ensure a constant injection level. The strobe light was positioned above the teflon bath which holds the wafer, immersed in the measurement solution. The distance between the strobe light and the wafer was kept constant at approximately 15 cm. The intensity of the strobelight

was set to 0.09 mJ/pulse. Using a photocell [2], we determined the injection level resulting from this pulse intensity to be approximately [3] $5\times10^{14}\mathrm{cm}^{-3}$.

4.2.3 Measurement of surface recombination velocity

The photoconductance decay measurement provides a value for the time constant of the fundamental decay mode, τ_{eff}, which is related to the surface lifetime, τ_{surf} and the bulk lifetime, τ_{bulk} as follows:

$$\frac{1}{\tau_{eff}} = \frac{1}{\tau_b} + \frac{1}{\tau_{surf}} \quad (4.17)$$

The surface lifetime is defined as the smallest root of the following transcendental equation [52]:

$$s = \sqrt{D/\tau_{surf}}\tan\left(\frac{d}{2\sqrt{\tau_{surf}D}}\right) \quad (4.18)$$

where D is the minority carrier diffusion constant.

We have used RFPCD to measure surface recombination velocity (SRV) on high bulk lifetime wafers. As Figure 4.4 shows, the relationship between measured lifetime and SRV involves three regimes. For very high SRV (region I), carrier diffusion to the surface is the rate limiting step in the recombination process and the measured lifetime is given by:

$$\tau_{eff} = \frac{d^2}{D\pi^2} \quad (4.19)$$

which is the average time it takes takes a carrier to reach the surface.

If the sample has a high bulk lifetimes (>1 ms), there is a very long intermediate range of s values where τ_{eff} is inversely proportional to s (region II):

[2]This photocell, manufactured by SunPower Co. and provided by Dr. R. Sinton (Sinton Consulting, San Jose, CA) had close to unit external quantum efficiency in the 450 - 1000 nm wavelength range.

[3]Because of the short pulse length ($\approx 1\mu s$), the injection level Δn may be considered independent of bulk lifetime. Because we performed all of our experiments on wafers with well passivated surfaces (s=1-100 cm/s), the effect of surface recombination velocity on injection level may be neglected also.

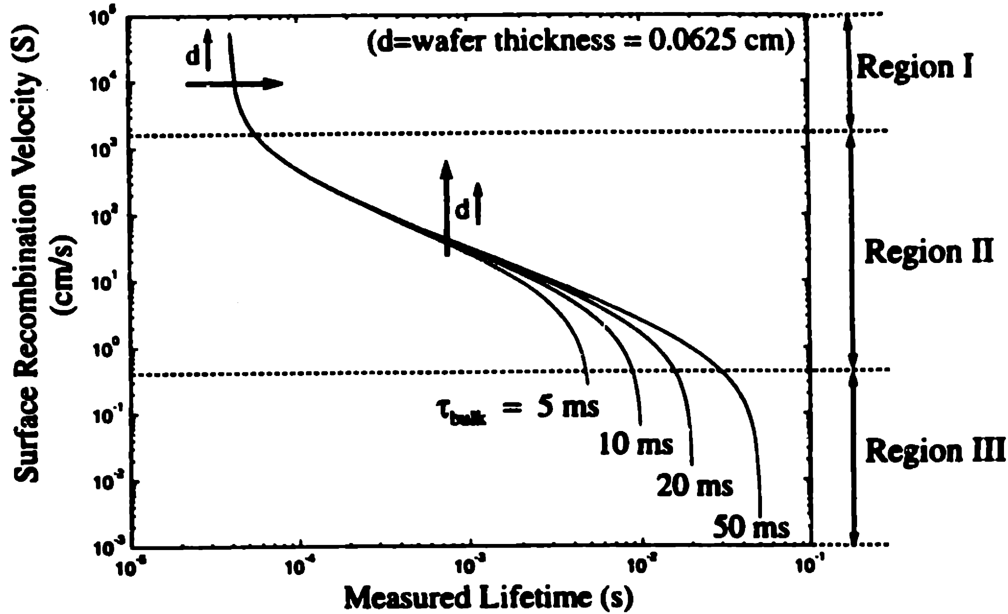

Figure 4-4: The measurement of surface recombination velocity by photoconductance decay.

$$\tau_{eff} = \frac{d}{2s} \tag{4.20}$$

Finally, for SRV smaller than d/τ_{bulk}, the measured lifetime is essentially the bulk lifetime (region III).

4.2.4 Carrier excitation by monochromatic light

So far we have only discussed the information contained in the lowest order decay mode of the photoconductance transient. If the initial carrier concentration is nonuniform, the time dependence of the excess carrier concentration can be calculated by Fourier analysis [52]. In this section, the decay of an initially nonuniform distribution, generated by a monochromatic light pulse, is reviewed.

The full one-dimensional analysis of the decay of a nonuniform distribution of excess carriers generated by a delta pulse of monochromatic light was treated in depth by Buczkowski *et al.* [58, 59] and Luke *et al.* [60]. Assuming that each

absorbed photon gives rise to one electron hole pair. the excess carrier distribution immediately after the excitation pulse is given by[4]:

$$\Delta n(t=0) = (1-R)\alpha_\lambda N_o exp(\alpha_\lambda(x-\frac{d}{2})) \tag{4.21}$$

where α_λ is the absorption coefficient at the wavelength used; d is the thickness of the wafer; R is the reflectivity of the surface, located at x=d/2; and N_o is the fluence of the laser pulse.

The time dependent excess carrier concentration for symmetrical illumination can be determined by solving the differential equation for combined diffusion and recombination :

$$(D_n\nabla^2 - \frac{1}{\tau_b})\Delta n = -\frac{d\Delta n}{dt} \tag{4.22}$$

subject to the boundary conditions (at x=±d/2):

$$-D_n\nabla(\Delta n) = s\Delta n \tag{4.23}$$

where D_n is the minority carrier diffusion length, τ_b is the bulk lifetime and s is the surface recombination velocity, which are all assumed to be independent of Δn [5].

The timedependent excess carrier concentration is given by:

$$\Delta_n(\alpha_\lambda, t) = e^{-t/\tau_b}\sum_{n=1}^{\infty} A_n e^{-\alpha_n^2 D_n t} cos\alpha_n x \tag{4.24}$$

Where the terms A_n are given by:

$$A_n = \frac{4\alpha_n(1-R)\alpha_\lambda N_o e^{-\alpha_\lambda d/2}}{(\alpha_\lambda^2+\alpha_n^2)(\alpha_n d + sin\alpha_n d)}(\alpha_\lambda sinh\left(\frac{\alpha_\lambda d}{2}\right) cos\left(\frac{\alpha_n d}{2}\right) + \alpha_n cosh\left(\frac{\alpha_\lambda d}{2}\right) sin\left(\frac{\alpha_n d}{2}\right)) \tag{4.25}$$

The coefficients α_n are defined by the transcendental equation:

[4]We have assumed $\alpha_\lambda d >> 1$.

[5]As mentioned earlier, the assumption of constant s, made here to allow analytical solution, is in fact rather restrictive.

$$\alpha_n tan(\alpha_n d/2) = \frac{s}{D_n} \tag{4.26}$$

The α_n values are the wavenumbers (cm^{-1}) of the normal modes of the carrier decay.

The higher order terms in Equation 6.14 damp out quickly, while the leading term defines τ_{eff}, the effective decay time (also sometimes referred to as the asymptotic decay time):

$$\frac{1}{\tau_{eff}} = \frac{1}{\tau_b} + \alpha_1^2 D_n \tag{4.27}$$

Buczkowski *et al.* [59] show that the amplitude of the higher order decay component is independent of the bulk lifetime, and can be used to calculate the surface lifetime if D_n, d and α_λ are known. From the knowledge of the surface lifetime and the asymptotic lifetime, τ_{eff}, the bulk lifetime can be determined. This analysis demonstrates that, in principle, the separation of bulk and surface lifetime can be achieved based on one single decay measurement with pulsed, monochromatic excitation. In practice, the separation method presented in this section is only possible under conditions where bulk and surface contribution to the effective lifetime are comparable.

In our measurements, we have consistently used high quality silicon with very high bulk lifetime (> 5 ms). For such high bulk lifetime, the contribution of the bulk lifetime to the effective lifetime can be neglected, and Equation 4.20 can be used to calculate the surface recombination velocity from the effective lifetime.

4.3 Effect of bandbending on surface recombination

4.3.1 Relationship between excess carrier density and surface bandbending

In all the material presented so far, a constant value for the surface recombination velocity s, defined by the boundary conditions (4.23), has always been assumed. However, ample evidence has been reported in the literature which shows that, in fact, s can be strongly dependent on excess carrier density [61, 62].

We have developed a straightforward model for the effect of bandbending on surface recombination, which assumes a pn-junction type photoresponse of the bandbending to excess carriers. While based on simple physics, our model sheds new light on the effect of surface charge on the surface recombination phenomenon. The effect of surface charge was pointed out previously [63], but, to our knowledge, has never been subjected to a quantitative analysis.

Our analysis is based on two assumptions:

- Surface recombination dominates over bulk recombination ($L_D >> d$).
- Surface recombination is small ($s << D/d$).

These assumptions make our model uniquely useful for the description of surface recombination in high bulk lifetime material with well passivated surfaces.

Figure 4.5 summarizes the terminology of surface bandbending. For a p-type semiconductor, $E_{Fn} - E_F$ is related to the bulk injection level by the expression:

$$E_{Fn} - E_F = \frac{kT}{q}\left(\frac{n_o + \Delta n}{n_o}\right) \quad (4.28)$$

If quasi-equilibrium holds in the space charge region (SCR), both the hole and electron quasifermi energy will be flat in the SCR. The product of electron and hole concentrations in the SCR is:

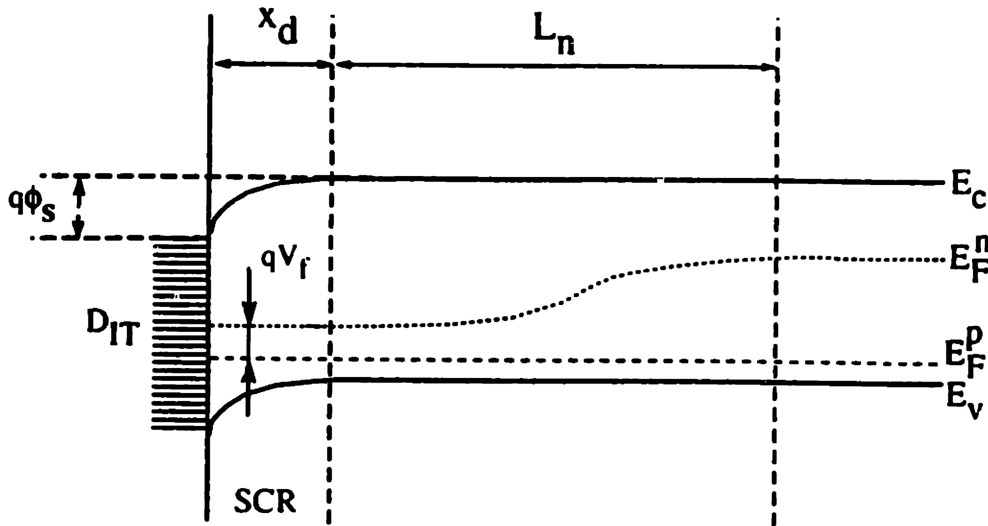

Figure 4-5: Surface band bending terminology. x_d is the space charge region (SCR) width. L_n is the minority carrier diffusion length. and ϕ_s is the bandbending potential (positive in depletion).

$$p_s n_s = n_i^2 exp\left(\frac{qV_F}{kT}\right) \tag{4.29}$$

where V_F is the separation between the quasi-fermilevels within the space charge region. Because we assumed a diffusion length in excess of the wafer thickness. and because the surface recombination velocity is small. the quasi fermi levels will be flat throughout the thickness of the wafer. remaining so as the decay progresses. For surface bands bent into depletion. as shown in Figure 4.5. low intensity illumination wil decrease the bandbending by an amount (assuming that s is small):

$$V_{oc} = \frac{kT}{q} ln(1 + \frac{\Delta n}{n_o}) \tag{4.30}$$

where Δn is the concentration of excess minority carriers. For small s. we may assume the photovoltage to equal V_{oc}, this is the open circuit photovoltage across a p-n junction under low level injection conditions.

Comparison of Equations 4.28 and 4.30 reveals that the photovoltage equals the separation between the electron and hole quasifermilevels (E_{Fp}=E_F for low level in-

jection):

$$V_{oc} = E_{Fn} - E_F \tag{4.31}$$

The surface minority carrier density carrier concentration in the dark is given by:

$$n_s = n_o exp\left(\frac{q o_s^o}{kT}\right) \tag{4.32}$$

Where $n_p^o = n_i^2/N_A$ is the minority carrier concentration in the bulk of the p-type semiconductor and ϕ_s^o is the bandbending potential in the dark (Figure 4.5). ϕ_s^o is related to the areal density of surface charge, Q (cm^{-2}), by:

$$\phi_s^o = \frac{qQ^2}{2K_s\epsilon_o N_A} \tag{4.33}$$

where Q represents both oxide charge and charge in the surface states. Since ϕ_s changes by an amount V_{oc} when the semiconductor is illuminated, we obtain for the surface bandbending under illumination, ϕ_s:

$$\phi_s = \phi_s^o - \frac{kT}{q} ln\left(\frac{n_o + \Delta n}{n_o}\right) \tag{4.34}$$

So the surface minority carrier concentrations under low level illumination are given by:

$$n_s = \frac{n_i^2}{N_A} exp\left(\frac{\phi_s}{kT} - ln\left(\frac{n_o + \Delta n}{n_o}\right)\right) \cdot \frac{n_o + \Delta n}{n_o} = n_o exp\left(\frac{q\phi_s^o}{kT}\right) \tag{4.35}$$

which is the same result as the surface minority carrier concentrations in the dark (Equation 4.32).

So if the bands are in depletion (or inversion) *the effect of low level illumination is to decrease ϕ_s, so as to keep the minority carrier concentration at the surface constant.* Note that the change in majority carrier concentration, assuming low level injection in the bulk, is given by:

$$p_s^{dark} = p_o exp\left(\frac{-q\phi_s^o}{kT}\right) \quad (4.36)$$

$$p_s^{light} = p_o exp\left(\frac{-q\phi_s}{kT}\right) = p_s^{dark} \cdot \left(\frac{n_o + \Delta n}{n_o}\right) \quad (4.37)$$

Equations 4.36 and 4.37 signify that the surface concentration of *majority* carriers at the surface scales with the *minority* carrier concentration in the bulk, if $\phi_s \neq 0$. *For a bulk injection level equal to the equilibrium concentration of minority carriers at the surface in the dark, ϕ_s becomes 0 and the bands are completely flat.* Thus, for a fully depleted surface (n_s=p_s=n_i), the injection level required to reach flat band will be very low (10^{10} cm^{-3}). Meanwhile, for a fully inverted surface (n_s=N_A), the injection level needed to reach flatband will equal the doping level.

In the case where the surface bands are in *accumulation*, the change of band bending with injection level is given by:

$$V_{oc} = \frac{kT}{q} ln(1 + \frac{\Delta p}{p_o}) \quad (4.38)$$

For low level injection, $\frac{\Delta p}{p_o} \approx 0$ and therefore V_{oc} is vanishingly small also. In conclusion, high injection levels are needed to flatten bands bent into accumulation.

4.3.2 Dependence of surface recombination rate on excess carrier density in presence of bandbending

The dependence of the surface recombination velocity on the surface carrier concentrations n_s and p_s was derived by Fitzgerald and Grove [64]. They assume a constant density of interface states, D_{it} ($cm^{-2}eV^{-1}$), throughout the energy gap; equal capture cross section for electrons and holes; and quasi-equilibrium throughout the space charge region. They find the following expression for surface recombination velocity:

$$s = \sigma v(kTD_{it}) \left(\frac{arccosh\left(\frac{p_s+n_s}{2n_i}\right)}{\sqrt{\left(\frac{p_s+n_s}{2n_i}\right)^2 - 1}}\right) \frac{N_A}{n_i} \quad (4.39)$$

As pointed out earlier, the presence of surface charge will cause the carrier concentrations at the surface to deviate from their bulk counterparts. Expressions (4.35) and (4.37) define the relationship between the concentrations of excess carriers at the surface, n_s and p_s, and Δn, the excess carrier concentration in the bulk. This dependence of n_s and p_s on Δn leads to a pronounced dependence of s (through p_s and n_s) on Δn, resulting in a nonexponential carrier decay. As shown in the next section, surface charge will lead to characteristic changes in the shape of the decay curve.

4.3.3 Effect of bandbending on minority carrier decay

Bandbending in depletion

We have numerically integrated equations (4.22) and (4.23), taking into account the dependence of s on Δn expressed by Equations (4.9) and (4.39). We assumed $\tau_b=\tau_{Auger}$, effectively neglecting SRH recombination in the silicon bulk. The excess carrier density vs time is shown in Figure 4.6. We assumed midgap surface states; a wafer thickness of 600 μm; a doping concentration $N_A=10^{15}$ cm^{-3}; an Auger recombination coefficient C= 3x10^{-34} cm^{6}s^{-1}; s_p=360 cm/s and s_n=40 cm/s.

At the highest injection levels, bulk Auger recombination is the dominant process. This mechanism does not require defect levels in the gap and its dependence on excess carrier concentration is given by Equation 4.2.

As the excess carrier density decreases further, a transition occurs to a regime where the recombination process is dominated by high-injection SRH recombination. In this regime, the surface recombination velocity is given by Equation 4.9.

As the excess carrier density falls below the bulk doping level of the semiconductor, the time constant of the carrier decreases to the minority carrier lifetime, τ_n. What happens in the final part of the decay, for excess carier concentrations lower than N_A, depends on the magnitude of the bandbending potential in the dark, ϕ_s^o. If the bands are bent into depletion, it can be shown that the asymptotic decay time depends on the band bending in the dark, ϕ_s^o, as follows:

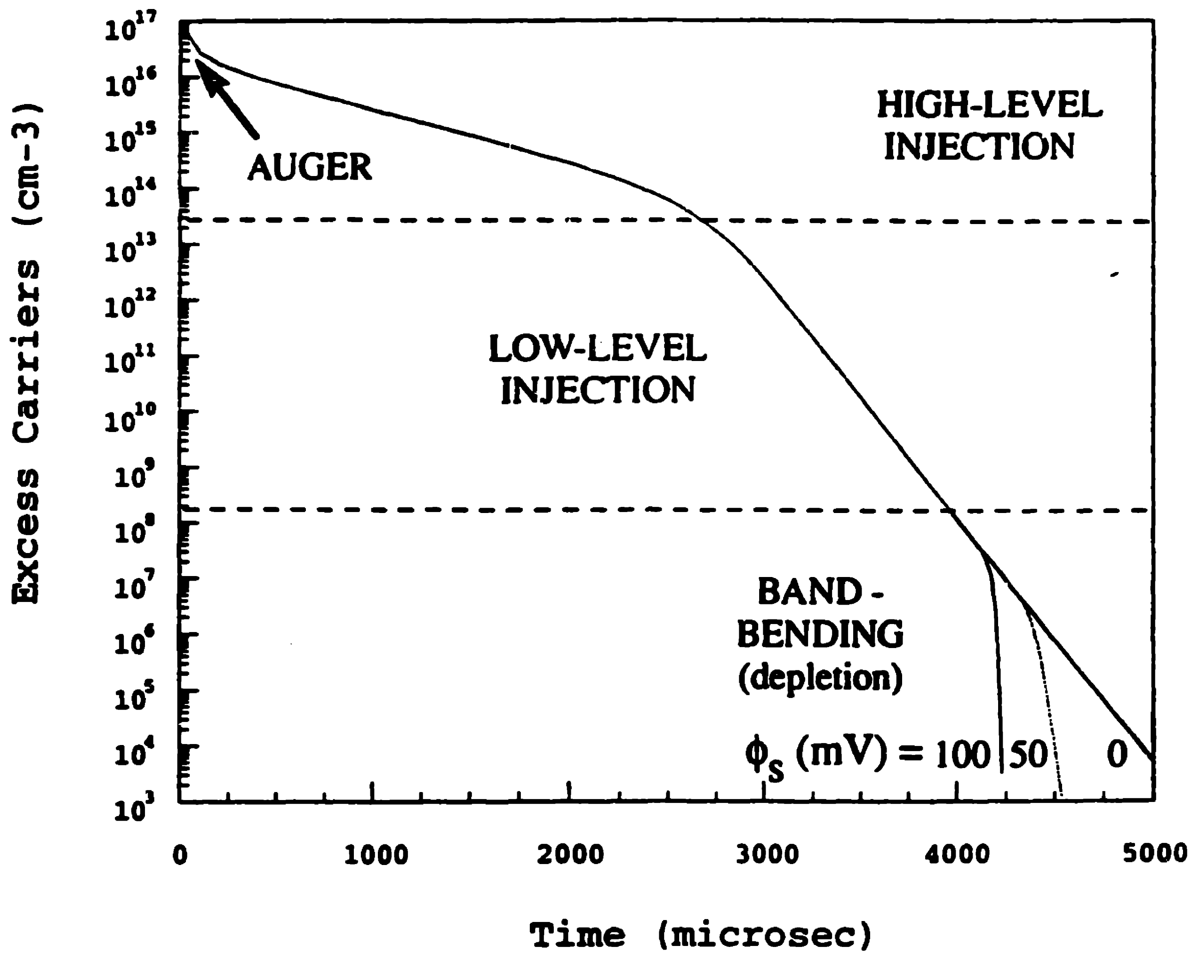

Figure 4-6: Effect of excess carrier concentration on recombination rate, in presence of bandbending in depletion.

$$\tau_a = \tau_n exp\left(-\frac{\phi_s^o}{kT}\right) \tag{4.40}$$

which means that surface recombination increases steeply in the tail part of the decay. .

As obvious from Figure 4.6, the effect of the surface charge will only manifest itself during the final part of the decay, for excess carrier densities wel below 10^{10} cm^{-3}. As discussed earlier. a low intensity background light is enough to completely abolish the bandbending in depletion, effectively eliminating its effect on the surface recombination rate. Even if the measurement were performed in the dark, the changeover in the surface lifetime would only occur at excess carrier densities well below the detection limit of the RFPCD measurement[6].

Bandbending in inversion

A similar calculation was performed to model the effect of inversion charge on the carrier decay rate (Figure 4.7). We assumed s_n=s_p=30 cm/s. The other parameters were the same as in the previous simulation. The slowest decay occurs when the surface is in full inversion (n_s=N_A). This corresponds to a bandbending potential ϕ_s^o of 580 mV. The other curves are for partial inversion. The decay curve for flatband is also shown.

In contrast with the depletion case, inversion charge can induce large changes in the surface lifetime (changes in slope in Figure 4.7) for excess carrier densities in the 10^{12}-10^{15} cm^{-3} range.

The asymptotic lifetime in the presence of inversion charge will be given by:

$$\tau_a = \tau_{fi} exp\left(\frac{-(\phi_s^o - \phi_s^{o,fi})}{kT}\right) \tag{4.41}$$

Where τ_{fi} and $\phi_s^{o,fi}$ are the surface lifetime and bandbending at full inversion, respectively.

[6]The lowest injection levels measurable with RFPCD are in the 10^{11} - 10^{12} cm^{-3} range, depending on the measurement conditions.

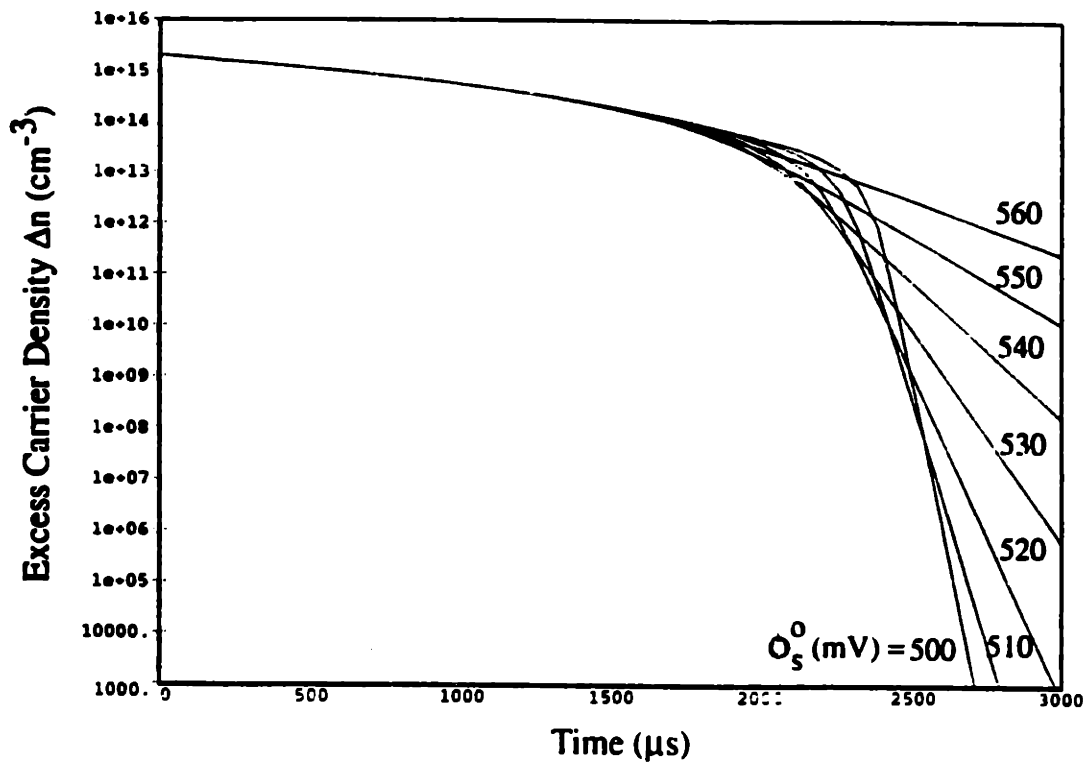

Figure 4-7: Effect of excess carrier concentration on recombination rate, in presence of bandbending in inversion.

Our analysis so far has not considered the effect of background illumination on the decay curves. It is easy to see that a background injection level of Δn will lead to an asymptotic decay time corresponding to an excess carrier concentration Δn.

4.4 The dependence of surface recombination velocity on bias potential

4.4.1 Introduction

The effect of the surface potential on the surface recombination velocity has been known since the early days of semiconductor research. In the 1950s and 1960s, this effect was employed in study of germanium surfaces, to establish gap levels associated with surface states on wet chemically treated wafers (see section 6.2.1 for a review). The extraction of energy levels from the surface potential dependence of the surface recombination velocity is based on the relationship derived by Many *et al.* [65] for a single discrete level in the gap:

$$s = \frac{N_t (c_n c_p)^{1/2} \left(\frac{n_o + p_o}{2n_i}\right)}{\cosh\left(\frac{E_t - E_i - q\psi_o}{kT}\right) + \cosh\left(\frac{-q\Psi_s - q\psi_o}{kT}\right)} \tag{4.42}$$

In this equation, N_t is the number of states per unit area, c_p and c_n are the capture probabilities per state per unit time for holes and electrons, respectively, ψ_s is the bandbending potential, referred to full depletion (fermi level at midgap), and ψ_o is given by:

$$\psi_o = \frac{kT}{2q} ln\left(\frac{c_p}{c_n}\right) \tag{4.43}$$

While at first sight Equation 4.42 seems very different from Equation 4.39, which was derived for a continuum of states in the gap, the dependence of s on ϕ_s, expressed by both equations, is in fact quite similar.

Yablonovitch [66] used a MOS capacitor structure to study the effect of surface potential on surface recombination at the Si/SiO_2 interface using the photoconductance

decay technique. He found that the recombination is dominated by centers whose electron capture cross section is about 100 times smaller than their hole capture cross section.

In our work, we have performed similar measurements on HF-immersed wafers, using a potentiostat to vary the bias potential across a silicon/HF liquid junction. This represents the first use of the photoconductance decay technique with surface potential control for *in-situ* measurement of the energy position of defect levels in the gap.

4.4.2 Experimental

We used a Gamry CMS 100 potentiostat [67] in the potentiodynamic mode to slowly scan the potential of a silicon wafer immersed in 1:100 HF with respect to a calomel reference electrode (Figure 4.8). A platinum mesh was used as counterelectrode.

After the standard MIT clean, an ohmic contact was made to a p-type wafer (type III) by clamping a copper wire against the surface and wetting the contact area with Ga-In eutectic. The wafer was positioned vertically in a teflon container. Effective lifetimes were measured continuously while the bias voltage was ramped from cathodic to anodic biasing at a rate of 5 mV/s.

4.4.3 Results and discussion

The effect of bias potential on the reciprocal effective lifetime, is shown in Figure 4.9. The reference potential E^* is arbitrary. We have assumed that the full potential bias drops across the semiconductor surface region [7]. A fit to the data with a function of the form 4.42 yields $|E_t - E_i| \approx 60$mV. We conclude that the surface recombination behavior is dominated by surface states positioned approximately 60 mV from midgap. The present analysis does not allow us to infer whether the states are above or below midgap.

[7]At small bias potentials, 1:100 HF has sufficiently high ionic strength to justify neglecting potential drops in the liquid compared to the voltage drop across the space charge region in the semiconductor.

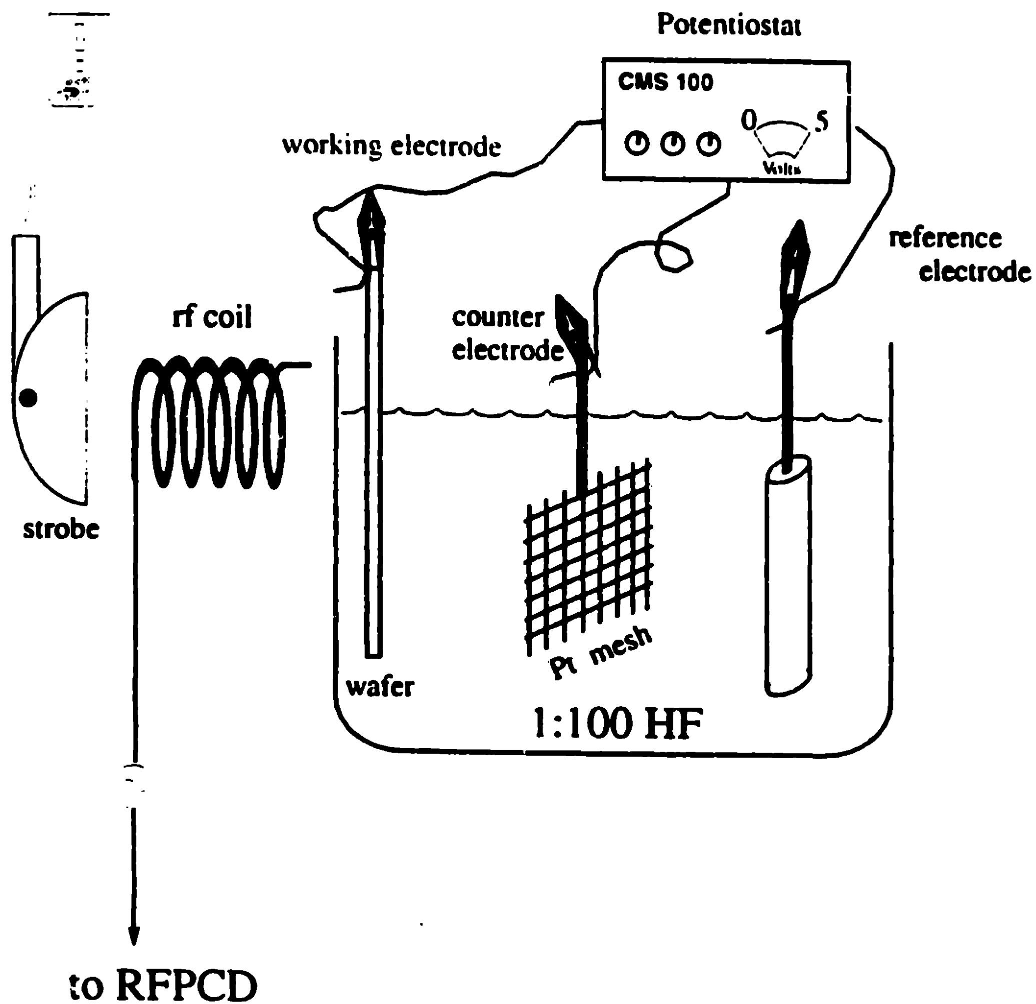

Figure 4-8: The experimental setup for the surface potential dependent lifetime measurements.

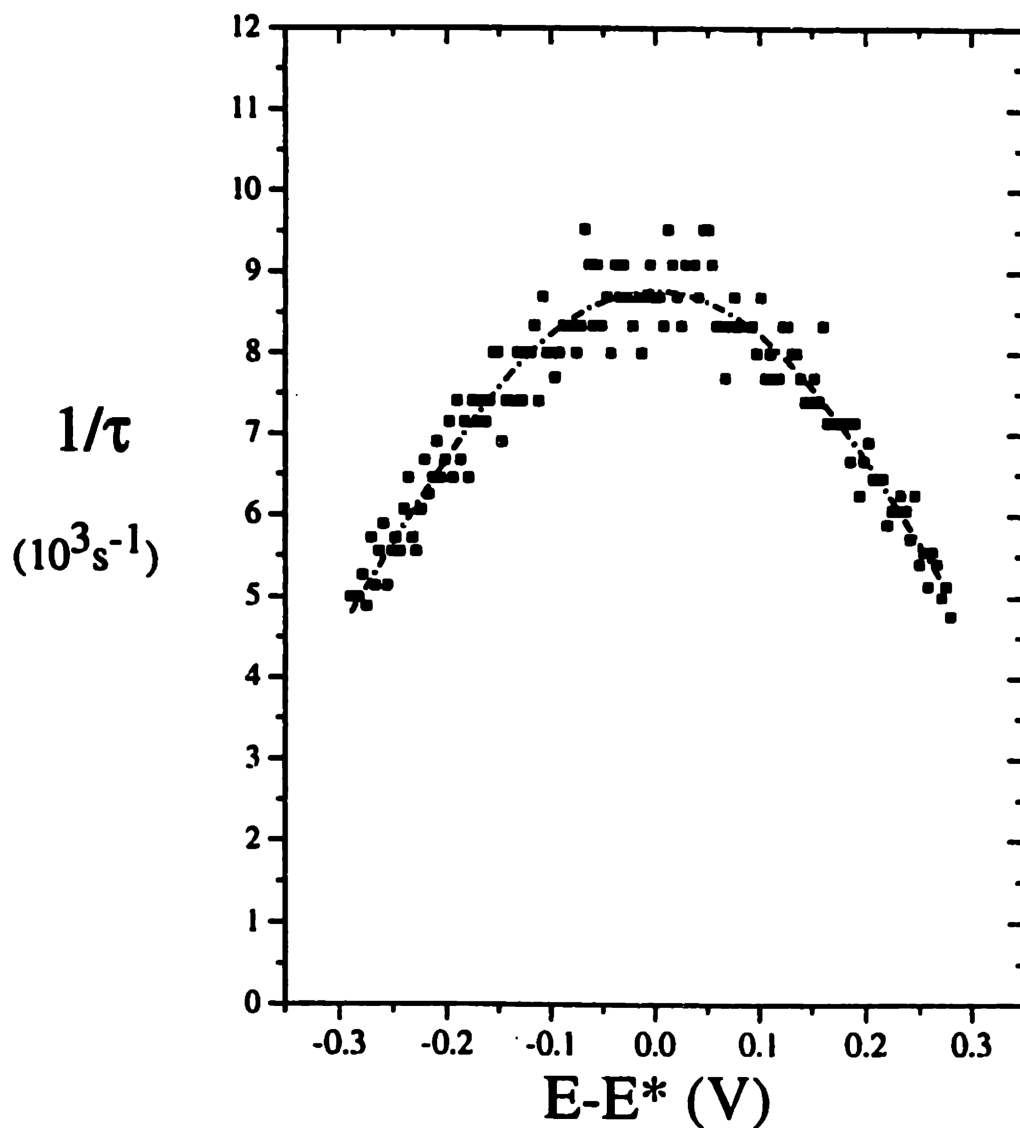

Figure 4-9: The dependence of the reciprocal effective lifetime on bias potential.

Our experiment is a convincing demonstration of the effect of bandbending on the surface recombination velocity. As discussed in Section 4.3, a variation of the surface lifetime during the decay will result if the bandbending potential ϕ_s relaxes back to its dark value ϕ_s^o during the decay. In the present experiment, the potentiostat acts to keep the bandbending at a constant value during the carrier decay, fixing s at the value set by Equation 4.42. Except for the initial part of the decay [8], excellent fits to the decay curve could be obtained with a single exponential function, proving that s is independent of Δn.

4.5 Intensity dependence of surface lifetime

4.5.1 Experimental

A verification of the model for the effect of injection level on the surface lifetime discussed in Section 4.3 is presented here [68]. To make sure the assumptions of the model were satisfied, we used high bulk lifetime thermally oxidized silicon for the experiments. The wafer (p-type (B), $N_A = 10^{15}$ cm^{-3}) were HF-last cleaned using high-purity chemicals. Cleaning and oxidation were performed at Intel Portland Technology Development. No postoxidation anneal was performed.

A 920 nm LED, pulsed at 100 Hz with a 10 % duty cycle, was used for carrier excitation. Drive currents were 1 A and 0.2 A. To measure at very low illumination intensity, the distance between the LED and wafer surface was varied.

4.5.2 Results

The decay curves measured at different intensities are shown in Figure 4.10. The decay curves exhibit a marked dependence on injection level (illumination intensity). Their concave shape on the logarithmic plot is characteristic for an *increase* in surface recombination velocity as the decay proceeds.

[8] The finite response time of the potentiostat leads to a variation in the decay time (nonexponential decay), as the bands are temporarily flattened by the high light intensity pulse.

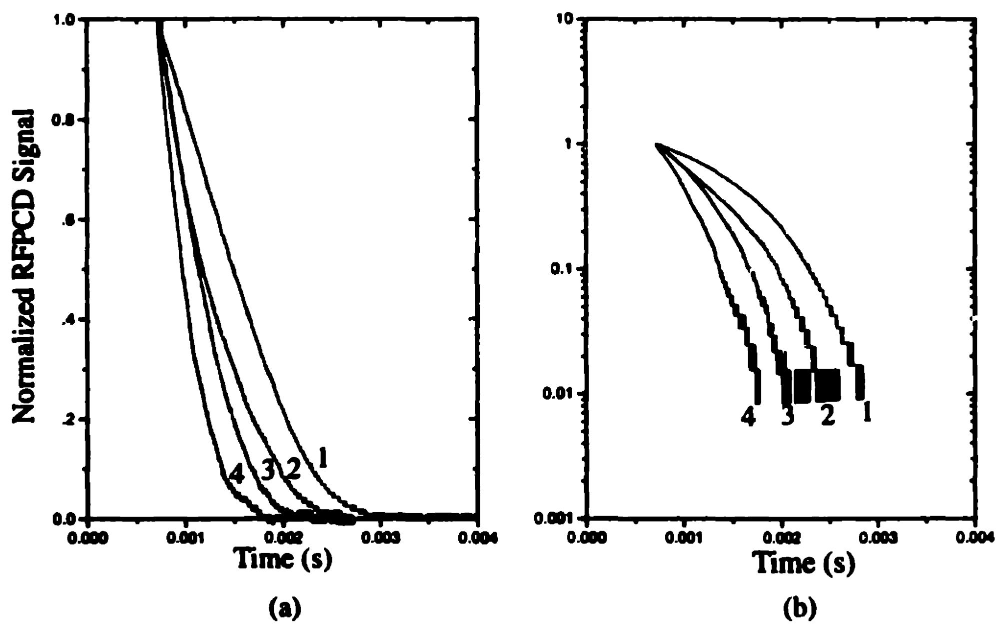

Figure 4-10: The effect of injection level on the normalized photoconductance decay transient plotted on a (a) linear and (b) logarithmic scale. The light intensity was varied by varying the distance between the LED and the wafer surface. The drive current was 1 A. The curves plotted are for relative illumination intensities (1) 1.00, (2) .0625, (3) .0156, (4).00360.

Figure 4.11 shows the variation of the initial lifetime, τ_i, with normalized illumination intensity, I/I_o. I_o (photons/cm^{2}s) is the illumination intensity obtained at 3 mm measurement distance and 1 A drive current. The illumination level was assumed to increase linearly with drive current, while being inversely proportional to the square of the measurement distance. The lifetimes were determined from the slope of the decay curve at the start of the decay. A strong variation of the effective lifetime with injection level is observed over a wide range (4 orders of magnitude) of illumination intensity. Because of the long pulse length of the LED source, the injection level in these measurements is not only dependent on illumination intensity (generation rate, G (cm^{-3}), of excess carriers), but also on the recombination rate (bulk lifetime and surface recombination velocity). Using a photocell and the PC-1D solar cell simulation package [69], we calculated an injection level of 10^{15} cm^{-3} corresponding to a relative illumination intensity I/I_o=0.2.

4.5.3 Discussion

We propose that the increase in lifetime between 0.0001 and .01 illumination intensity is caused by the presence of positive surface charge. We believe that fixed oxide charge, resulting from thermal oxidation without annealing, is causing partial inversion of the surface of the wafer under study. The surface charge causes an increase in lifetime with injection level in the low ($\Delta n << N_A$) injection level range, as shown in Figure 4.7. The asymptotic decay time is a strong function of the surface charge present. As the inversion charge decreases from full inversion to depletion, the steepness of the tail part of the decay increases rapidly.

Around I/I_o=0.01, flat band is reached, causing a plateau in the surface lifetime. As the injection level is increased beyond the doping level N_A, the initial decay time increases further as high level injection conditions are reached. In order to determine the high injection lifetime $\tau_n + \tau_p$ (Equation 4.10), we used a 24 V halogen light as background illumination during the RFPCD measurement. At the highest bias light intensity, the lifetime value reaches a value of approximately 2 ms. This measurement establishes $\tau_n + \tau_p$:

$$\tau_{hl} = \tau_n + \tau_p = 2ms \tag{4.44}$$

The surface lifetime value at flatband is τ_n $\approx$780μs (Figure 4.11) and hence τ_p $\approx$1220μs. We have therefore:

$$\frac{\sigma_n}{\sigma_p} = \frac{\tau_p}{\tau_n} \approx 1.5 \tag{4.45}$$

The slightly higher capture cross section for electrons indicates a positively charged recombination center (donor). Using a capture cross sections of 10^{-15}cm^2, we estimate an areal density of surface states of $\approx$ 5x10^9cm^{-2}.

At the very low injection end, the asymptotic lifetime provides information about the bandbending potential referred to full inversion, $\phi_s^o - o_s^{o,fi}$:

$$\tau_a = \tau_{fi} exp\left(\frac{-(\phi_s^o - \phi_s^{o,fi})}{kT}\right) \tag{4.46}$$

Based on exponential fits to the tail part of the decay curves for the lowest injection levels, we calculated τ_a $\approx$180μs. Based on 4.46, we obtain $o_s^o - \phi_s^{o,fi}$ = 38 mV. Using Equation 4.33, a value for the *positive* surface charge of 8.4x10^{11}cm^{-2} is found.

Unfortunately, we have *not* been able to obtain the surface charge value of this same wafer by an independent measurement, such as surface charge analysis (SCA), or MOS-CV. However, the paper by Deal *et al.* [70] allows us to make an estimate of the surface charge value for a given oxidation treatment. Deal *et al.* observed that the fixed oxide charge is independent of oxide thickness, the doping concentration, and the doping type. The oxidation temperature has a strong influence on the amount of fixed oxide charge (the lower the oxidation temperature. the higher the fixed oxide charge). For a Si (100) wafer oxidized at 900° C in dry oxygen, Deal *et al.* predict a surface charge of 2x10^{11}cm^{-2}.

The discrepancy between measured and predicted value is probably due to the effect of background illumination (room light) on the decay curves, as discussed in Section 4.3.3. With a background injection level Δn, the decay will first follow the curve shown in Figure 4.7; once the excess carrier concentration reaches the back-

ground injection level, the surface recombination velocity will remain constant and the decay will follow a straight line tangential to the curves shown in the plot. Thus. background illumination will lead to an underestimation of $\phi_s^o - \phi_s^{o,fi}$ and, hence. an overestimation of the surface charge.

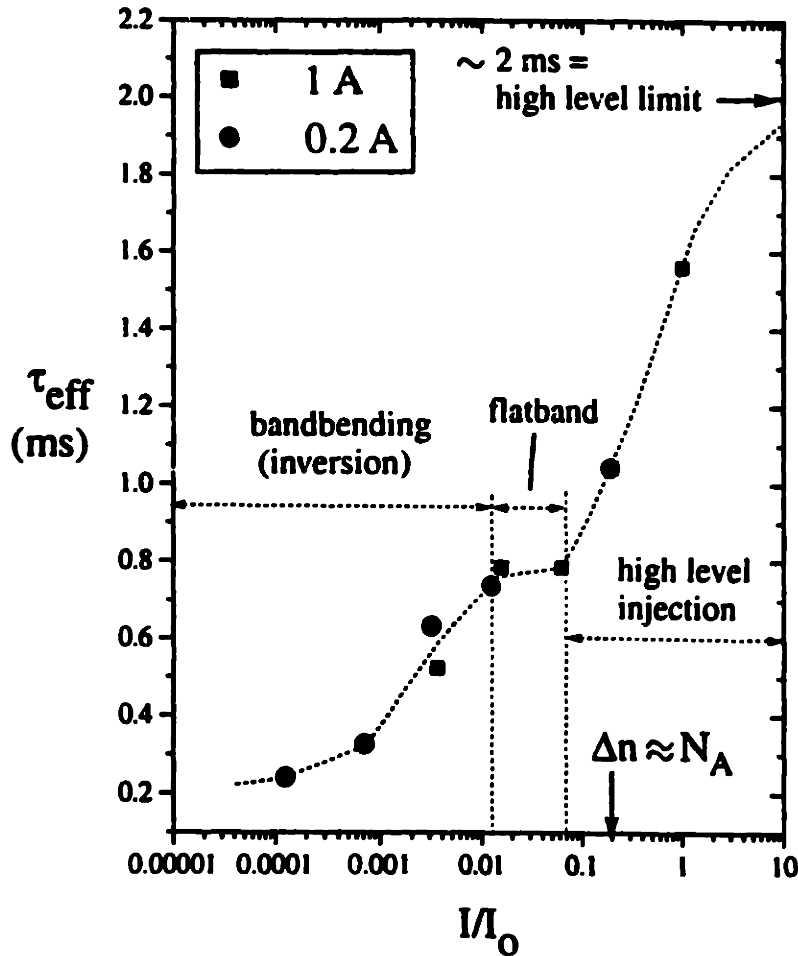

Figure 4-11: The variation of effective lifetime, τ_{eff}, with log(relative illumination intensity).

4.6 Conclusions

While in the past. surface recombination has largely been treated as an undesirable side effect in bulk lifetime measurements. we propose the use of surface lifetime measurements for control and characterization of silicon surfaces. Through the use of

material with sufficiently high bulk lifetime, this technique allows measurement of the areal density of surface defects with unprecedented sensitivity (detection limit $\approx$ $10^8 cm^{-2}$).

Earlier theoretical treatments of surface recombination failed to take into account the effect of surface charge on carrier recombination. We have developed a detailed model, based on the assumption that the photoresponse of the bands obeys pn-junction type behavior, for the dependence of surface recombination velocity on excess carrier density in the presence of surface charge. Our model applies uniquely to well passivated surfaces (s << D/d), so that quasi-equilibrium holds throughout the thickness of the wafer. We predict an increase of the instantaneous decay time with increasing injection level, as flattening the bands reduces surface recombination.

Our theory is supported by two empirical verifications. First, we demonstrate control of surface recombination using a bias potential, applied across the silicon-dilute HF liquid junction. This effect can be used to determine the position of defect states in the gap. Our work in this area represents the first use of the photoconductance decay technique for potential-dependent surface lifetime measurements.

Secondly, we have employed RFPCD, using pulsed LEDs for carrier excitation, to study the dependence of surface lifetime on injection level. The observed dependence of the surface lifetime on illumination intensity can be used to extract the ratio of capture cross sections, bandbending potential, and surface charge, as summarized in Table 4.1.

At the lowest injection levels, the presence of positive charge on a p-type wafer causes an increase in the surface recombination rate, compared to flatband. As the injection level is increased, the bands flatten and the "true" low level injection lifetime, τ_n, is recovered. The bandbending referred to full inversion, $\phi_s^o - \phi_s^{o,fi}$, can be determined from the ratio τ_n / τ_a (τ_a =asymptotic lifetime in the low level injection limit). In turn, the bandbending potential ϕ_s^o determines the surface charge. As the injection level is further increased in the flatband regime, surface recombination enters the high injection regime. We used a strong bias light to determine the high injection lifetime, $\tau_n + \tau_p$.

Quantity	Measurement
σ_n/σ_p	τ_p/τ_n
ϕ_s^o	$\phi_s^{o,fi}$-kTln(τ_n/τ_a)
Q	$\sqrt{\frac{2K_s\epsilon_o N_A \phi_s^o}{q}}$

Table 4.1: The determination of the ratio of capture cross sections σ_n/σ_p, bandbending potential ϕ_s^o, and surface charge, Q, from surface lifetime measurements.

Chapter 5

Impurity Chemisorption on Hydrogen Terminated Silicon

5.1 Introduction

In this chapter, we present the application of *ab initio* electronic structure calculations to model surface reactions of impurities with monolayer passivated silicon surfaces. Our goal is threefold: (1) to obtain insight in the reactivity of silicon surfaces terminated by different monolayers; (2) to establish guidelines for the design of new passivation chemistries and (3) to improve our understanding of the effect of different adsorbates on the electronic structure of the surface.

We focus on chemisorption reactions of halogens, oxygen, and metal ions. The research has direct implications for pre-epi cleaning, where chemisorption of organics and oxygen during air exposure following cleaning is a special concern. Because of the extraordinary influence of halogen and oxygen surface chemistry on the adsorption behavior of reducible ions from cleaning solutions on silicon, the reaction chemistry described in this chapter will be of great use in Chapter 6, which discusses metal deposition from HF.

Recent successes of atomistic modeling [71] have raised the hopes of circumventing difficult experimental problems by computational methods. Of all modeling techniques, *ab initio* or "first principles" methods, while by far the most timeconsuming,

have the greatest appeal because they describe the chemistry of materials at the highest possible level, and their accuracy is in principle only limited by the level of theory used. During the last decade, continual decreases in the cost of computing power have greatly expanded the application domain of *ab initio* methods, by making accurate calculations on large systems affordable. An important asset of first principles techniques lies beyond their usefulness for the modeling of chemical bonding and structure. Because *ab initio* methods are based on the full solution, of the electronic structure problem of a solid, they provide information on electron states, and, hence, a material's electrical and optical properties.

Ab initio methods are frequently used to obtain information on the energetics and mechanistics of surface reactions. In our work, we have used the Hartree-Fock method for single point calculations on relatively small clusters (9 silicon atoms). Minimal energy geometries were calculated using empirical potentials. We have focused our attention on the effect of bond order and bond polarity on reaction kinetics.

5.2 Background

5.2.1 Halogen adsorption

The high affinity of halogens for covalent semiconductor surfaces results from their electron configuration. By accommodating an unpaired electron from the dangling surface bond in their valence cloud, halogens achieve the noble gas configuration in their outer shell, forming strong bonds with the silicon surface atoms. The surface chemistry of halogens on semiconductor surfaces is a topic of considerable practical importance to semiconductor processing, because halogens play a key role in silicon etching. Halogens compounds such as HBr, HI, HCl, and Cl_2, F_2 and XeF_2 have been used for gas-phase etching of silicon[72]. Iodine, dissolved in ethanol [73] or methanol [74] has been demonstrated to provide effective passivation of the silicon dangling bond. Passivation by bromine dissolved in methanol was found to be less stable than by iodine [26].

Van de Walle *et al.* [75], using local density functional theory in combination with *ab initio* pseudopotentials to study silicon etching by fluorine, showed that insertion of atomic fluorine into Si-Si bonds becomes possible because of relaxed steric constraints in the near-surface region. Trucks *et al.* [76] used total energy calculations at the Hartree-Fock level to study the mechanism of silicon etching and hydrogen passivation in HF solutions. They showed that while hydrogen termination is thermodynamically less favorable than termination by fluorine, H is the predominant surface species because its displacement by fluorine involves a large energy barrier.

5.2.2 Oxygen adsorption

The initial stage of native oxide growth on silicon, a popular topic in surface science, is of both fundamental and practical interest. Oxygen chemisorption on hydrogen terminated surfaces is known to lead to increases in the contact resistance of tungsten contacts deposited by CVD [12], as well as degradation of epilayer quality. While most theoretical work has focused on the mechanism of oxygen chemisorption on bare, reconstructed surfaces, which are prepared by annealing in ultra high vacuum, impurity chemisorption on hydrogen terminated surfaces prepared by HF dipping is a major concern for low temperature CVD processes [77].

On the theoretical side, Hoshino *et al.* [78] found theoretical and experimental evidence for adsorption of molecular oxgen as a precursor to native oxide growth on bare, 2x1 reconstructed Si(100). Batra *et al.* [79] performed multiconfiguration self consistent field calculations to show that dissociative chemisorption is energetically more favorable, with atomic oxygen in the first-layer bridging position as the most stable adsorption geometry. Miyamoto *et al.* [80], using gaussian basis sets with the local density approximation for exchange and correlation, studied the insertion mechanism of atomic oxygen in bond-centered positions between the first and second layer atoms.

The growth of native oxide on HF-passivated silicon has been the subject of a great many experimental studies in recent years. Several studies, based on XPS (X-ray photoelectron spectroscopy) and MIR-IR (multiple internal reflection infrared spec-

troscopy) measurements, suggest that H-passivation degrades only slowly in cleanroom air[12, 81, 82, 83, 84, 85, 86, 87]. XPS studies [81, 82] show that a monolayer of oxide is formed after 10-12 hours of exposure to cleanroom air. However, the use of a nitrogen ambient during wafer and N_2-sealing during wafer transfer was reported to significantly lower the contact resistance of W/n^+ Si contacts, suggesting that the initial stages of native oxide growth take place much earlier than suggested by the XPS and MIR-IR data. Hence, the general use of controlled ambients during wet cleaning and wafer transfer has been proposed [12]. Further support for this hypothesis is provided by free exciton photoluminescence (PL) studies on HF-passivated silicon, which revealed an immediate change in the PL spectrum when wafers were exposed to oxygen or cleanroom air [87]. The authors concluded that oxygen instantaneously attacks H passivation.

5.3 Computational approach

5.3.1 *Ab initio* electronic structure methods

Over the years, silicon has become one of more popular systems for *ab initio* studies, mainly because of the relevance of atomistic processes for its performance as an electronic device material. The computational methods typically used can be subdivided in two classes: calculations on supercells, typically using the local density functional method (LDF) [89, 90] to include correlation and exchange; and real-space calculations on clusters. A popular method for real space calculations is the Hartee-Fock method, which constructs the molecular wavefunction as a Slater determinant of spin orbital functions to include exchange. In quantum chemistry, the Hartree-Fock method is often combined with many-body perturbation theory (Möller-Plesset) or configuration interaction (CI) to include correlation. A disadvantage of the Hartree-Fock method is that computation times scale rapidly with system size ($t \propto N^{2.7}$ versus $t \propto N^{2.2}$ for LDF [91]), making calculations on large systems and heavy atoms time-consuming.

Because localised bonding is thought to play a dominant role in the chemical processes occurring at the silicon surface, cluster calculations have become a well established research tool for studying surface processes on silicon. Today, several powerful ab initio molecular modelling packages are commercially available, most of which are chiefly used by chemists for mechanistic studies of chemical reactions. Gaussian 94, a powerful commercial Hartree-Fock package [92] originally developed by Pople and coworkers at Carnegie-Mellon, is used in the present research for single point calculations on medium-sized clusters [1]. Gaussian 94 uses linear combinations of atomic orbitals to construct the molecular wave function. This program has been used succesfully in the past to explain the mechanism of hydrogen passivation of silicon in HF [76] and to model adsorption of molecular oxygen on bare silicon [78].

While the Hartree-Fock method does not include electron-electron correlation effects, the method was selected because our main goal was to gain insight in the nature of the silicon-impurity bonds, not to calculate accurate geometries or total energies. The poor scaling of the Hartree-Fock method with system size was not considered an issue, because we used small clusters and performed only single point calculations cluster with fixed geometry. As mentioned earlier, we used empirical potentials to establish the lowest energy geometry of the cluster[2].

5.3.2 The Hartree-Fock approximation

The Hartree-Fock approximation is a well established method in quantum chemistry for solving the time-independent Schroedinger equation of a molecular system (Equation 5.1):[3]

[1]Calculations were performed on a Cray C90 at the Pittsburgh Supercomputer Center, and a DEC Alpha/OSF-1 workstation at MIT.

[2]Geometry optimizations using empirical potentials were performed on Cerius2 [93], a user friendly molecular modeling package. Cerius2 was also used to visualize the results of Hartree-Fock electron density calculations.

[3]A comprehensive discussion of the Hartree-Fock method and related techniques can be found in [94].

$$(\frac{\hbar^2}{2m}\sum_{i=1}^{N}\nabla_i^2 + \frac{1}{2}\sum_{i\neq j}\frac{e^2}{|r_i - r_j|} - \sum_{i,I}\frac{Z_I e^2}{|r_i - R_I|} + \frac{1}{2}\sum_{I\neq J}\frac{Z_I Z_J e^2}{|R_I - R_J|})\Psi = E\Psi \qquad (5.1)$$

In this equation, the terms represents the kinetic energy of a system of particles, and the electron-electron, electron-nucleus and nucleus-nucleus contribution to the potential energy, respectively. Without simplifying assumptions, the Schroedinger equation for a molecule is a many-body problem which cannot be solved exactly, except for the smallest *atomic* systems.

In the Hartree-Fock method, the solution to Equation 5.1 is made tractable by making a number of simplifying approximations.

- (1) The Born-Oppenheimer approximation states that the movement of the nuclei can be treated independently from the electronic motion problem [4], allows separation of nuclear and electronic coordinates:

$$H^{elec}\Psi^{elec}(\vec{r},\vec{R}) = E(\vec{R})\Psi^{elec}(\vec{r},\vec{R}) \qquad (5.2)$$

where $E(\vec{R})$ represents the total electronic energy and $\vec{R}$ is the vector of the nuclear coordinates.

- (2) The electronic Schroedinger equation is then solved for solutions of the form:

$$\Psi(\vec{r_1},...,\vec{r_n}) = \prod_{i=1}^{n}\phi_i(\vec{r_i}) \qquad (5.3)$$

where $\phi_i(\vec{r_i})$ are molecular spin orbital functions. By assuming solutions of the form (5.3), electron-electron correlation is implicitly neglected.

- (3) To accommodate Pauli's exclusion principle, the molecular wave function is then constructed from the N molecular spin orbital functions as a Slater determinant:

[4]This assumption is plausible, since the mass of a proton or neutron is roughly 1800 times the electron mass.

$$\Psi(\vec{r_1},...,\vec{r_n}) = \frac{1}{\sqrt{N!}} \begin{vmatrix} \phi_1(\vec{r_1}) \cdots \phi_N(\vec{r_1}) \\ \vdots \\ \vdots \cdots \phi_q(\vec{r_i}) \cdots \vdots \\ \vdots \\ \phi_1(\vec{r_N}) \cdots \phi_N(\vec{r_N}) \end{vmatrix} \tag{5.4}$$

One approach to allow numerical solution of the Hartree-Fock equations, is to expand the molecular orbital functions in terms of atomic-orbital-like functions χ_μ:

$$\phi_i = \sum_\mu c_{\mu_i} \chi_\mu \tag{5.5}$$

Where the index μ runs over the constituent atoms; χ_μ are atomic-like orbitals. These atomic-like orbitals are expansions of atomic orbital functions in terms of simple gaussians g_p:

$$\chi_\mu = \sum_p d_{\mu_p} g_p \tag{5.6}$$

Simple gaussians are functions of the form:

$$g(\alpha, \vec{r}) = cx^n y^m z^l e^{-\alpha r^2} \tag{5.7}$$

Using this formalism, the solution of Equation 5.1 is reduced to the solution of an eigenvalue equation in $\overline{\overline{C}}$, the matrix of the expansion coefficients c_{ij}:

$$\overline{\overline{F}} \cdot \overline{\overline{C}} = \overline{\overline{S}} \cdot \overline{\overline{C}} \cdot \overline{\overline{\epsilon}} \tag{5.8}$$

where $\overline{\overline{F}}$ is known as the Fock matrix, $\overline{\overline{S}}$ is the overlap matrix, and $\overline{\overline{E}}$ is a diagonal matrix whose elements ϵ_i represent the orbital energy of molecular orbital χ_i. Because the Fock matrix itself depends on the molecular orbital expansion coefficients c_{ij}, Equation 5.8 must be solved iteratively. The computation of the Fock matrix involves the computation of complex multicenter integrals, whose numerical evaluation is greatly simplified by the expansion of the molecular orbitals in gaussian

basisfunctions through Equations 5.5 and 5.6. Based on the variational principle, the total electronic energy will decrease monotonously if the Hartree-Fock algorithm converges.

5.3.3 Cluster choice

In most of our calculations, we used Si_9H_{14}-type clusters to study the reactions between impurities and a monohydride group on the Si (100) surface (see Figure 5.1). Some calculations on a larger cluster ($Si_{17}H_{22}$) were performed to study the effect of cluster size on the electronic structure results. The Si_9H_{14} cluster models two atoms from the top silicon layer and four second-layer, two third-layer and one fourth-layer silicon atom. The backbonds to the silicon lattice are saturated by hydrogen terminator atoms. Hydrogen is chosen as a bond terminator, because the silicon-hydrogen bond is close to nonpolar, mimicking the silicon-silicon bond. The Si_9H_{14} cluster was used earlier by Chabal and coworkers) for analysis of vibrational spectra of hydrogen atoms on 2x1 Si(100)-H [95]. Its small size notwithstanding (none of the silicons are fourfold coordinated), we have found the Si_9H_{14} cluster to be an accurate model for surface bonding on Si(100), allowing correct predictions of trends in impurity bonding.

The monovalent termination of Si (100) represents but one of the many possible surface configurations. Typical (100) surfaces, prepared by HF dipping, are microscopically rough and covered with a mixture of mono-, di-, and trihydrides [32] . However, a highly regular monohydride termination on (100) silicon can be produced by high temperature annealing in a hydrogen ambient ("hydrogen bake"). This ideal Si(100)-H 2x1 surface, which consists of silicon dimers with one hydrogen terminating each silicon, has a greatly reduced reactivity compared to wet chemically prepared, HF-passivated silicon [96]. While the assumption of monovalent termination is implicit in all our calculations, the proposed reaction mechanisms apply equally well to other surface groups; attack of the monovalent group will generally proceed much slower than analogous reactions involving di- and trivalent silicons because of increased steric constraints.

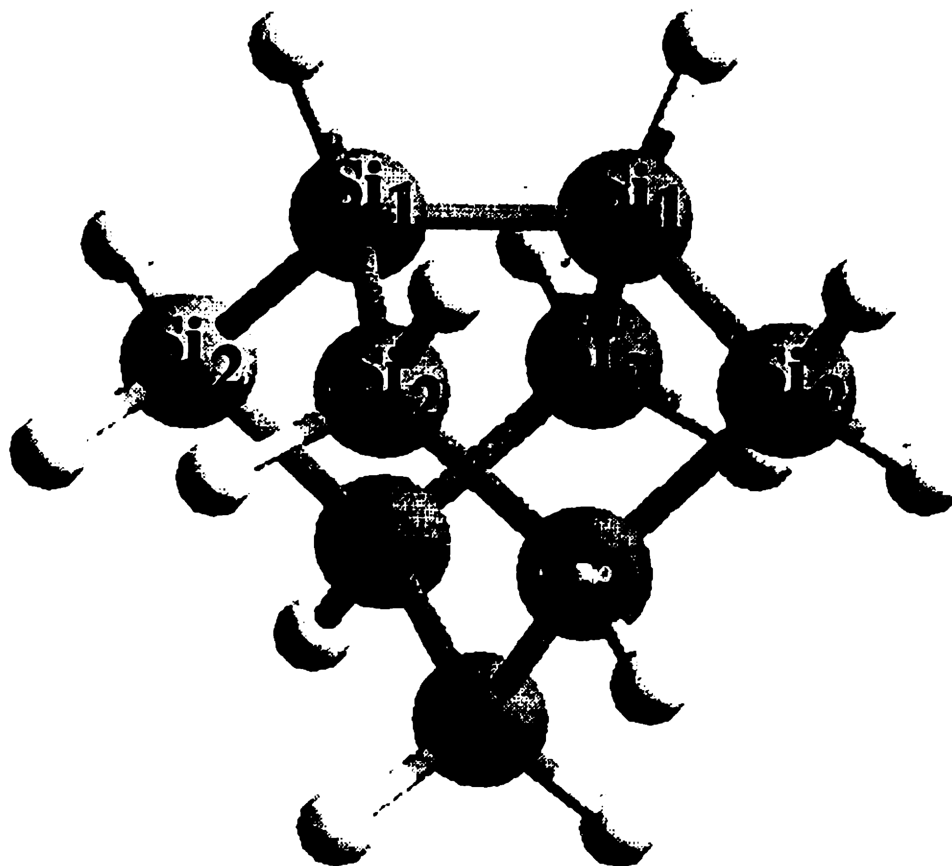

Figure 5-1: The Si_9H_{14} cluster, used to model monovalent termination of the silicon (100) surface. The top and second layer silicon atoms are indicated.

For all our computations, we optimized the cluster geometry (bond distances and bond angles) prior to the Hartree-Fock single-point calculations using empirical potentials based on the universal force field developed by Rappé *et al.* [97] and implemented in Cerius2. Next, for the single point Hartree-Fock calculations on clusters containing atoms up to chlorine , we used the 6-31 G* polarized basis set. 6-31 G* is a double zeta basis set with polarization functions added to the heavy atoms. This basis set is becoming the standard for calculations involving up to medium-sized systems [98]. Calculations on clusters with heavier atoms were performed using the LANL2DZ basis set[5]. A clear discussion of the effect of basis set choice on the results of Hartree-Fock calculations can be found in Ref. [98].

5.4 Halogen chemisorption on Si(100)-H

5.4.1 Character of the silicon-halogen bond

We have studied the bonding of different impurity species on silicon (100) surfaces using the Hartree-Fock approach as outlined above. We used the $Si_9H_{12}X_2$ cluster to model monovalent termination different impurities. Figure 5.2 shows the total valence electron density obtained for the $Si_9H_{12}F_2$ and $Si_9H_{12}Cl_2$clusters. The very large electron density around the F atom is explained by the higher electronegativity and the shorter bond length compared to Cl termination.

Table 5.1 summarizes some of the results obtained from single-point Hartree-Fock calculations. The charge on the impurity atom (X=F, Cl, Br, I, OH) and the top silicon (Si_1, Figure 5.1) is obtained by a Mulliken population analysis [6]. The bond order n_{12} (or overlap between the atomic basis functions χ_μ's centered on different atoms) is a measure of the silicon-impurity bond strength.

The charge on the top silicon and halogen atom is consistent with the electroneg-

[5]The LANL2DZ basis set [88] uses effective core potentials (ECP) for nuclei heavier than Cl, treating the electrons near the nucleus in an approximate way.

[6]Mulliken population analysis computes atomic charges projecting the total electronic density on each of the basic functions χ_μ centered on a given atom.

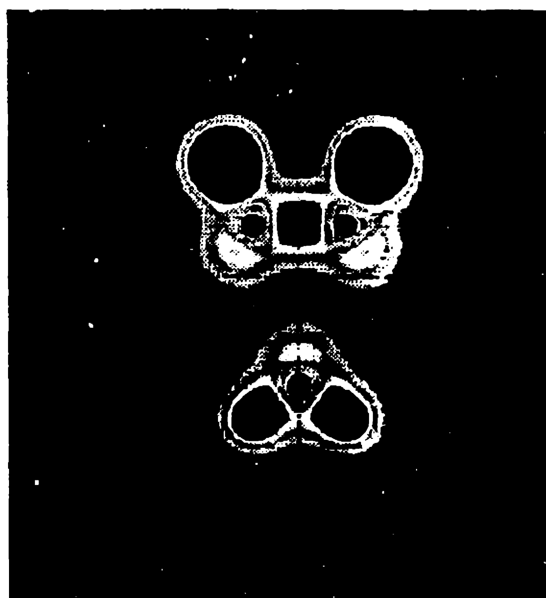

(a)

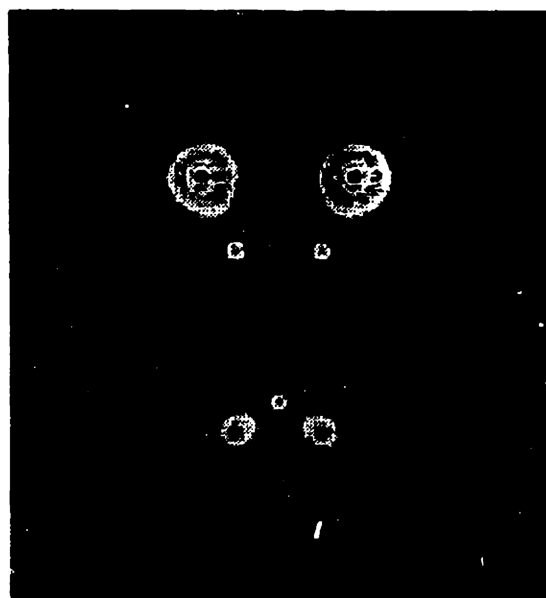

(b)

Figure 5-2: Total valence electron density maps for (a) $Si_9H_{12}F_2$ and (b) $Si_9H_{12}Cl_2$. The slice is defined by the two top silicon and the lowest lying (fourth layer) silicon.

ativity differences between silicon and the different halogens. As Z (atomic weight) of the halogens increases, the atomic polarisability increases, because the core electrons are effective screeners of the nuclear charge. This effect explains the rapid increase in bond polarity from F over Cl to Br. The low polarity of the Si-I bond is obvious from the very small negative charge on the iodine terminator atom (0.06 electrons, 0.02 less than the charge on the hydrogen terminator). For Br and I, the charge on the top silicon (Si_1) is negative, indicating that these halogen atoms draw electrons from the deeper lying atoms to the top silicon layer.

X	q_X	q_{Si_1}	n_{12}	$\Delta\chi$
H	-0.08	0.01	0.332	0.3
F	-0.49	0.53	0.260	2.1
Cl	-0.34	0.19	0.295	1.3
Br	-0.22	-0.03	0.265	1.1
I	-0.06	-0.24	0.257	0.7
OH	-0.39	-0.46	0.302	1.7

Table 5.1: Net charge on halogen atom, q_X; net charge on top silicon atom, q_{Si1}; order of bond between top and second layer silicon atoms, n_{12}); and difference in Pauli electronegativity, $\Delta\chi$. All data except $\Delta\chi$ were obtained from single point Hartree-Fock calculations on $Si_9H_{12}X_2$ clusters.

The *charge* on the top silicon and the *bond order* between the top and second layer silicons provide important information on the stability of a given surface termination in different types of ambients. The low charge on the top layer silicon (q_{Si_1}=0.01)

and the high bond order between the top and second layer silicons (n_{12}=0.332) are the main reason behind the extraordinary stability of the monohydride termination on Si (100).

5.4.2 Stability of halogen termination in different ambients

Stable passivation of silicon surfaces has been reported for each of the halogen species F, Cl, Br and I [99, 100, 101, 102]. Passivation by a solution of iodine in methanol has been proposed as an alternative to hydrogen passivation by HF [74]. For application in IC processing, a passivation layer has to be resistant to exposure to the cleanroom ambient, containing oxygen, water and trace hydrocarbons; furthermore, compatibility with aqueous environments is desirable. The purpose of this section is to elucidate the breakdown mechanisms of halogen passivation layers in different ambients and formulate conditions for stable passivation, based on the Hartree-Fock results shown in Table 5.1 We propose two distinct mechanisms for the attack of halogen passivation: silicon backbond insertion and hydrolysis of the silicon-halogen bond. Both reaction types are discussed briefly below. We focus on the effect of Si-X bond polarity on the relative reaction rates of different chemisorbed halogens.

Silicon backbond insertion

The more polar the bonding between the top and second layer silicon, the more vulnerable the surface will be to attack by small, polar molecules, such as HF and OH^-, which possess both electrophilic and nucleophilic properties. The instability of fluorine termination in HF was already pointed out by Trucks *et al.* The successive attack of the bonds between the top and the second layer silicon atoms by successive insertion of HF molecules occurs by the following reactions (Figure 5.3):

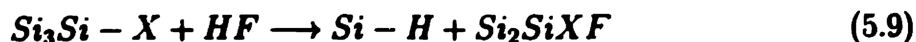

$$Si_3Si - X + HF \longrightarrow Si - H + Si_2SiXF \tag{5.9}$$

$$Si_2Si - XF + HF \longrightarrow Si - H + Si - SiXF_2 \tag{5.10}$$

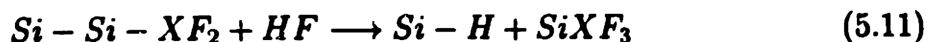

$$Si - Si - XF_2 + HF \longrightarrow Si - H + SiXF_3 \quad (5.11)$$

In neutral and basic solutions, attack by the hydroxyl ion, OH^-, leads to analogous reactions.

As the charge on the top silicon increases, the attack by the polar HF molecule will occur more readily. The strength of the back bond, expressed by the bond order n_{12}, is indicative of the barrier height associated with the backbond breaking process. Table 5.1 shows that for all the halogens the bond order n_{12} is lowered significantly compared to the hydrogen case; we conclude therefore that significant backbond weakening is caused by all of them. Based on the results listed in Table 5.1, we predict relative rate constants $k_F > k_{Cl} > k_{Br} > k_I$ for the backbond insertion reaction. For Br and I, the insertion reaction will be sluggish as the charge on the top silicon is negative. Meanwhile, passivation by I and Br is still less stable than for H, due to the reduced strength of the backbond (smaller bond order (n_{12})).

Hydrolysis of halogen termination

In aqueous ambient, chlorine and fluorine termination will hydrolyze according to the reactions (Figure 5.4):

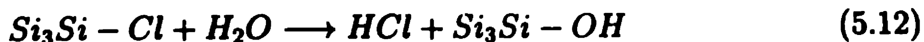

$$Si_3Si - Cl + H_2O \longrightarrow HCl + Si_3Si - OH \quad (5.12)$$

$$Si_3Si - F + H_2O \longrightarrow HF + Si_3Si - OH \quad (5.13)$$

The hydrolysis reaction introduces a silanol group (Si-OH). Silanol groups are highly reactive; their role as precursors for native oxide growth will be discussed in the next section. Silanol groups are quickly attacked by HF, leading to etching of the top silicon layer, analogous to reactions 5.19-5.11.

Because the Si-I and Si-Br bonds are less polar, their hydrolysis in water is expected to proceed much more slowly, with rate constants $k_{Br} > k_I$. By substituting

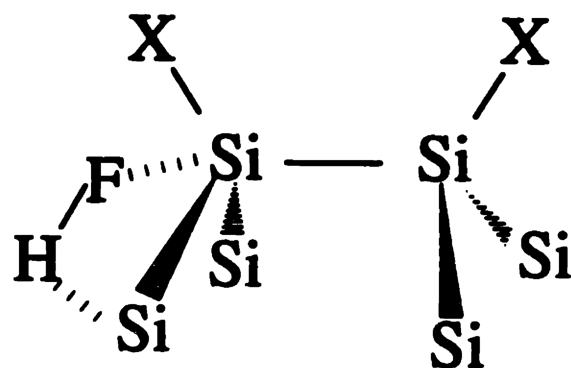

Figure 5-3: Passivation attack by backbond insertion.

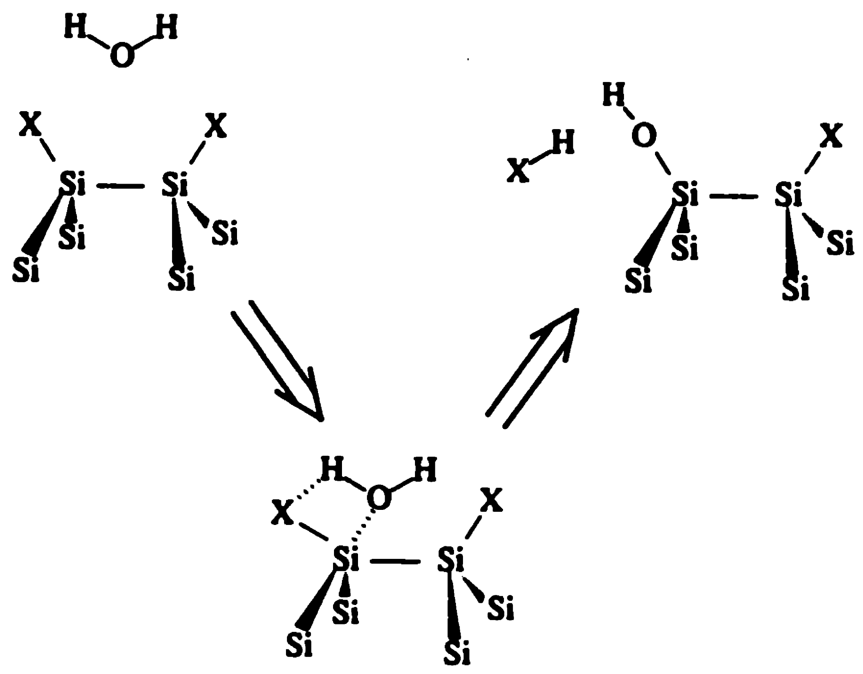

Figure 5-4: Passivation attack by hydrolysis of the surface bonds.

a less polar molecule such as an alcohol (ROH) for water, the hydrolysis reaction can be further suppressed. The work of M'saad [26] illustrates these predictions. M'saad discovered that electronic passivation of silicon by bromine and iodine, dissolved in methanol solution, is possible; however, the stability of bromine termination was found to be less than for iodine. The higher polarity of the Si-Br compared to the Si-I bond, resulting in a faster hydrolysis by the CH_3OH molecule, explains why passivation by Si-Br is less stable than Si-I.

Moisture in ambient air will cause the same hydrolysis reactions to take place, be it at slower rates. The absence of a hydrolysis reaction for Si-H, is another reason why hydrogen passivation is more stable in aqueous ambient than Si-I. Similarly, chlorine passivation prepared by gas exposure is stable in dry O_2 but rapidly etches a monolayer of silicon in the presence of water [103].

5.5 Oxygen chemisorption on Si(100)-H

5.5.1 Chemisorption mechanism

Based on earlier theroretical work [80], there is general agreement that the final stage of the oxygen chemisorption reaction involves the formation of so-called bridgebonded oxygen atoms on the top silicon layer. There is also mounting evidence that water molecules play a crucial role in the oxidation reaction [12]. Based on this evidence, we propose a two-step reaction mechanism for the oxidation of Si(100)-H at room temperature in the presence of O_2 and moisture. The reaction mechanism is illustrated in Figure 5.5. The first step in the oxidation process is slow, and involves insertion of O_2 into the Si-H bonds to form Si-OH:

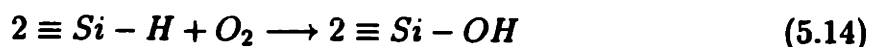

$$2 \equiv Si - H + O_2 \longrightarrow 2 \equiv Si - OH \qquad (5.14)$$

The slow kinetics of this reaction are a result of the low polarity of the Si-H bond and the need to dissociate the oxygen molecule.

We propose that condensation of the silanol groups, to form "bridging" oxygen

and water, is catalyzed by water molecules:

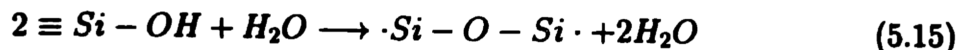

$$2 \equiv Si - OH + H_2O \longrightarrow \cdot Si - O - Si \cdot + 2H_2O \quad (5.15)$$

The net result of reaction is the formation of one bridging oxygen (Si-O-Si), two dangling bonds (Si·), and the removal of one water molecule (Figure 5.5).

This mechanism strongly supported by the report that a large fraction of the oxygen atoms, present in a native oxide, grown in water. originate from water molecules rather than dissolved O_2 [104]. More generally, the present reaction will occur with polar adsorbates other than -OH as well. Later in this chapter, we will present our own experimental confirmation of the introduction of dangling bonds by O_2 exposure on a water dipped in 48 % HF [105]. In this case, physisorbed water was suspected to catalyze the oxidation reaction during O_2 exposure. First, we present some examples of the use of electronic structure calculations to obtain information on the electronic structure of the silicon surface.

5.5.2 Effect of chemisorbed impurities on the electronic structure of the hydrogen passivated surface

Hydrogen, halogen and hydroxyl termination

We performed Hartree-Fock calculations on $Si_9H_{12}X_2$ clusters representing monovalent Si-H, Si-F, Si-Cl, Si-I and Si-OH termination of Si(100). These clusters are the analogues of the Si_9H_{14} cluster (Figure 5.1), with the terminators atoms of the top silicons replaced by X (X=F, Cl, Br, I, OH). The orbital energies obtained from the Hartree-Fock calculations are shown in Figure 5.6. The orbital energy levels consist of occupied and virtual levels, separated by an energy gap. The size of the gap is a function of the cluster size, and converges to the true bandgap of silicon (1.1 eV) if the calculation were performed on a large enough cluster. The difference between the highest occupied molecular orbital (HOMO) energy and the lowest unoccupied molecular orbital (LUMO) energy defines the bandgap of the cluster. Because of the

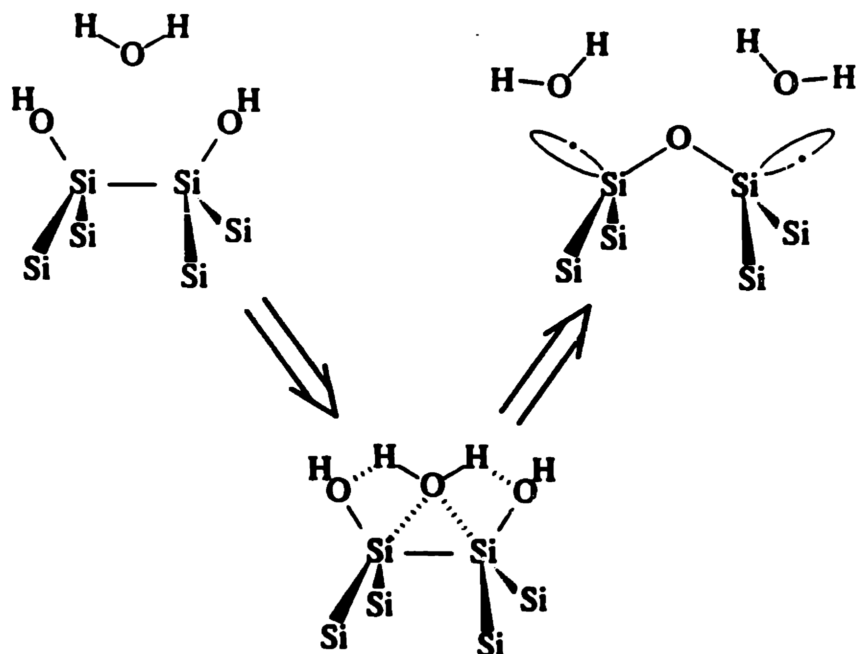

Figure 5-5: The catalysing role of water in the condensation of surface silanols. This reaction introduces a bridging oxygen and two dangling bonds.

relatively small size of the clusters studied here, the bandgap shown in Figure 5.3 is far greater than the bandgap of silicon (1 Hartree = 13.6 eV).

The results demonstrate that none of the surface groups has a significant influence on the energy spectrum of the cluster. Because each of the terminator atoms forms stable bonds with silicon, the bonding and antibonding levels of the surface bonds lie so far apart, as to not introduce energy levels in the "bandgap" of the cluster.

Bridging oxygen and silicon dangling bonds

We performed Hartree-Fock calculations on a cluster representing the final stage of native oxide growth as proposed in Section 5.5.1 (atomic oxygen in the first-layer bridging position and two silicon dangling). Figure 5.7 shows the cluster, $Si_9H_{14}O$, and its orbital energies. These levels are associated with orbitals that are centered on the top silicons; both are an admixture of atomic 3p, 4s and 4p levels. We conclude that these levels are the orbitals associated with the well known "dangling" surface bonds.

Experimental evidence for the introduction of surface states as a result of native oxide growth is presented in Section 5.7.2 of this chapter.

5.6 Metal chemisorption on Si(100)-H

5.6.1 Chemisorption mechanism

Metal adsorption on hydrogen terminated silicon occurs via two distinct steps. First, metal ions are physisorbed from solution. This process can be represented by the reaction:

$$M^{z+}_{solution} \longrightarrow M^{z+}_{silicon} \tag{5.16}$$

The equilibrium adsorption level, $\Gamma_{M^{z+}}$, is given by the Gibbs adsorption equation [106]:

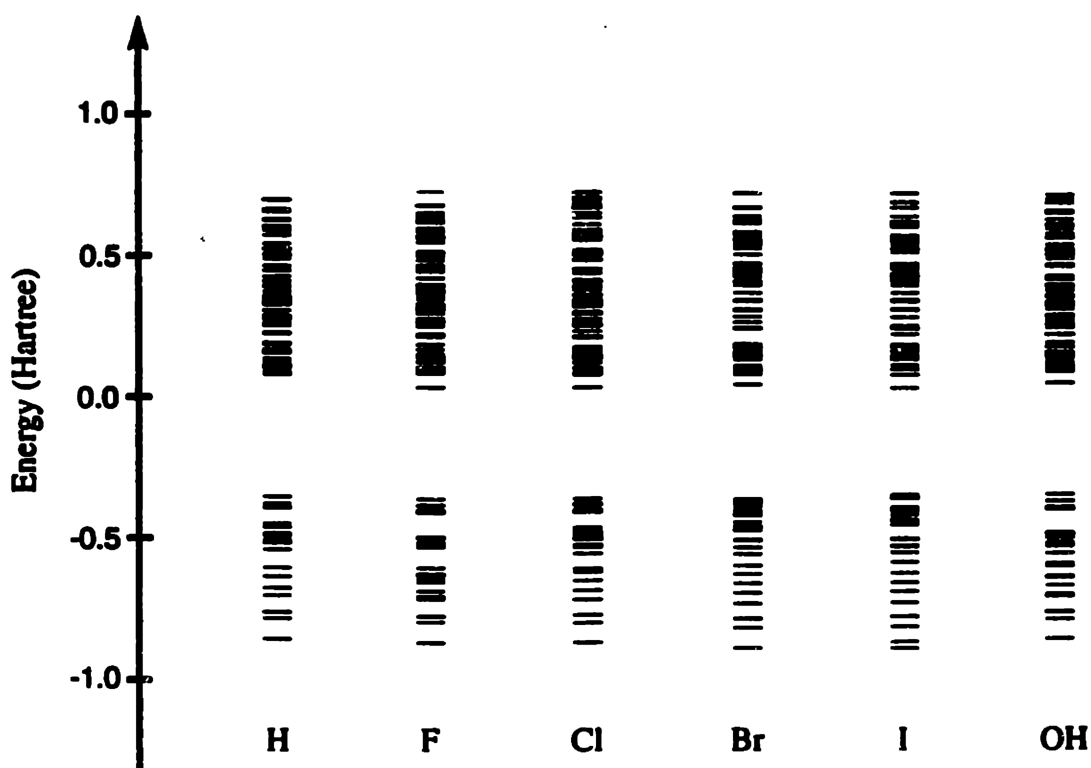

Figure 5-6: Orbital energies for Si_9H_{14}; $Si_9H_{12}F_2$; $Si_9H_{12}Cl_2$; $Si_9H_{12}Br_2$; $Si_9H_{12}I_2$; $Si_9H_{12}(OH)_2$. Only the energy values near the HOMO and LUMO level are shown.

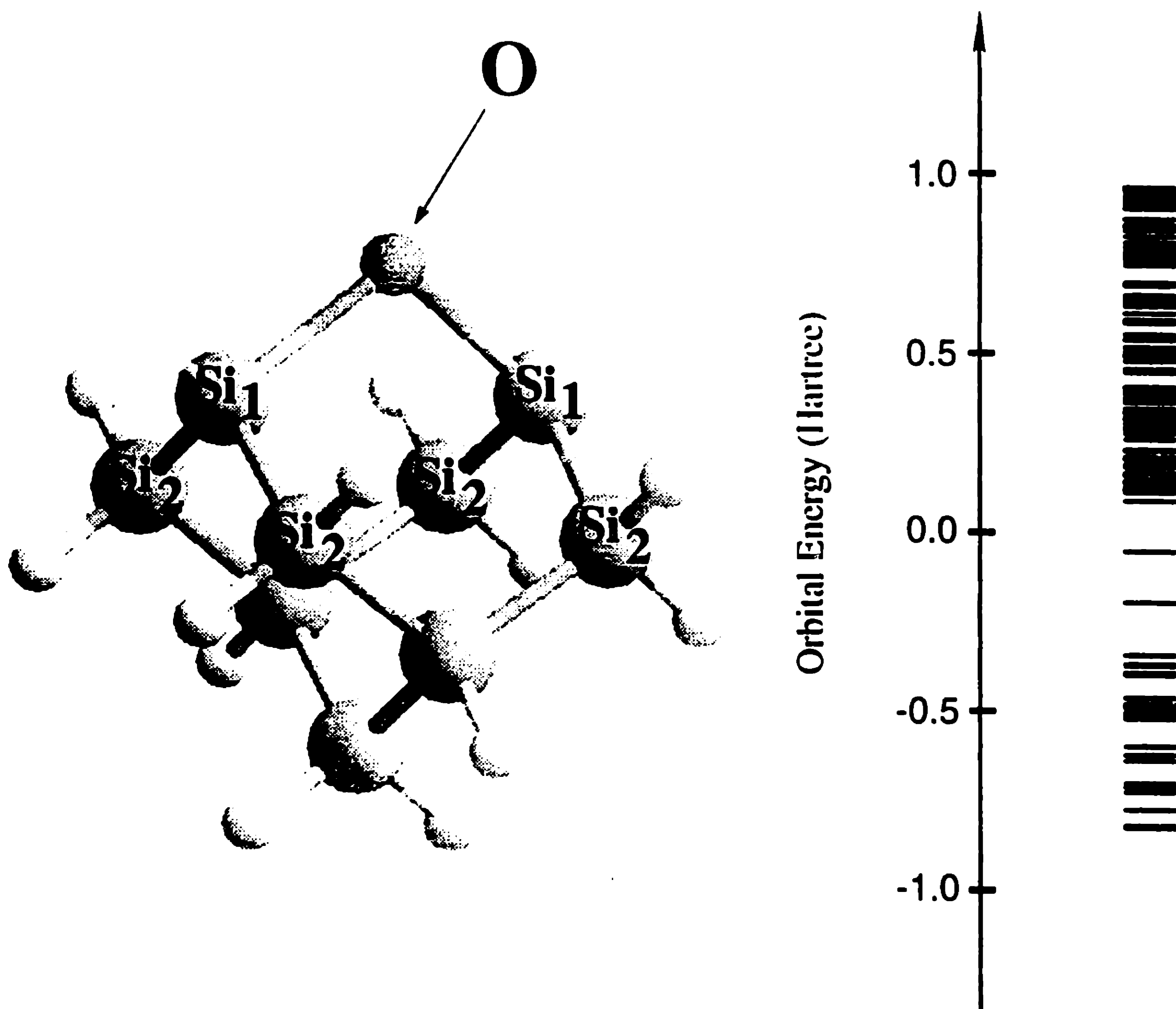

Figure 5-7: The $Si_9H_{12}O$ cluster and its orbital energy levels. Only the energy values near the HOMO and LUMO level are shown.

$$\Gamma_{M^{z+}} = -\frac{1}{RT}\left(\frac{d\sigma}{dlna_{M_{z+}}}\right) \tag{5.17}$$

In a second step, the metal may undergo reduction:

$$M^{z+}_{silicon} + ze^- \longrightarrow M^o_{silicon} \tag{5.18}$$

where the electrons are provided by simultaneous dissolution (oxidation) of the silicon.

The discussion of the thermodynamic and kinetic requirements for the latter reaction to take place at an appreciable rate will be postponed until the next chapter. Here we wish to discuss the impact of chemisorbed metallic impurities on the electronic structure of the hydrogen terminated silicon surface.

5.6.2 Effect of chemisorbed copper on the electronic structure of the surface

Because of the important role of copper chemisorption in this research, we performed a Hartree-Fock calculation on a cluster containing a single copper atom bonded to the silicon surface as shown in Figure 5.8. Because copper has valence 2, divalent bonding of the copper atom (to two surface silicon atoms) was assumed.

The orbital energy spectrum for the $Si_9H_{12}Cu$ cluster is shown in Figure 5.9. For comparison, the energy spectrum of the Si_9H_{14} cluster is also shown. Because the cluster has a net spin 3 (quadruplet state), the orbital energies of exhibit spin degeneracy (*i.e.*, the spin up and spin down orbitals have different energies). As in the case of the bridge-bonded oxygen, we observe deep states in the bandgap of the $Si_9H_{12}Cu$ cluster, which can be expected to enhance the rate of excess carrier recombination. The midgap copper level, which is expected to be the dominant recombination center, is occupied, and hence will behave as a donor in p-type material. The corresponding orbital is localised on the surface copper atom and has strong Cu3s character, with considerable admixing of Cu5p and Cu2s orbitals. We conclude that

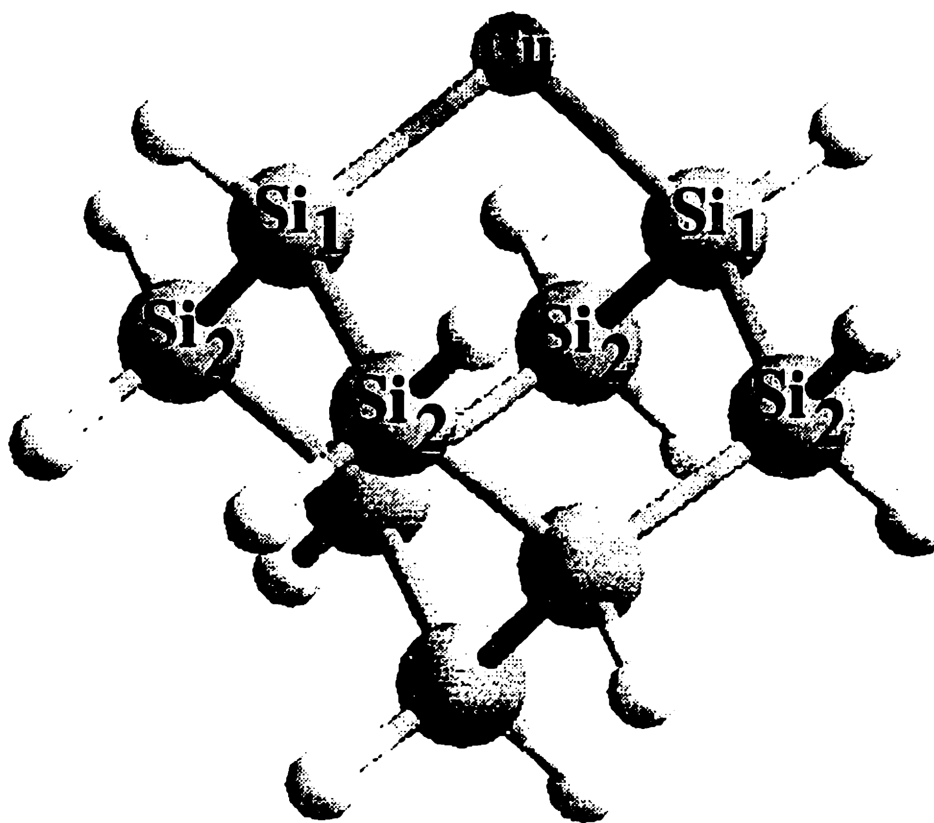

Figure 5-8: The $Si_9H_{14}Cu$ cluster used to model the bonding of an individual copper atoms to (100) silicon.

chemisorbed metal atoms can introduce deep levels in the silicon bandgap.

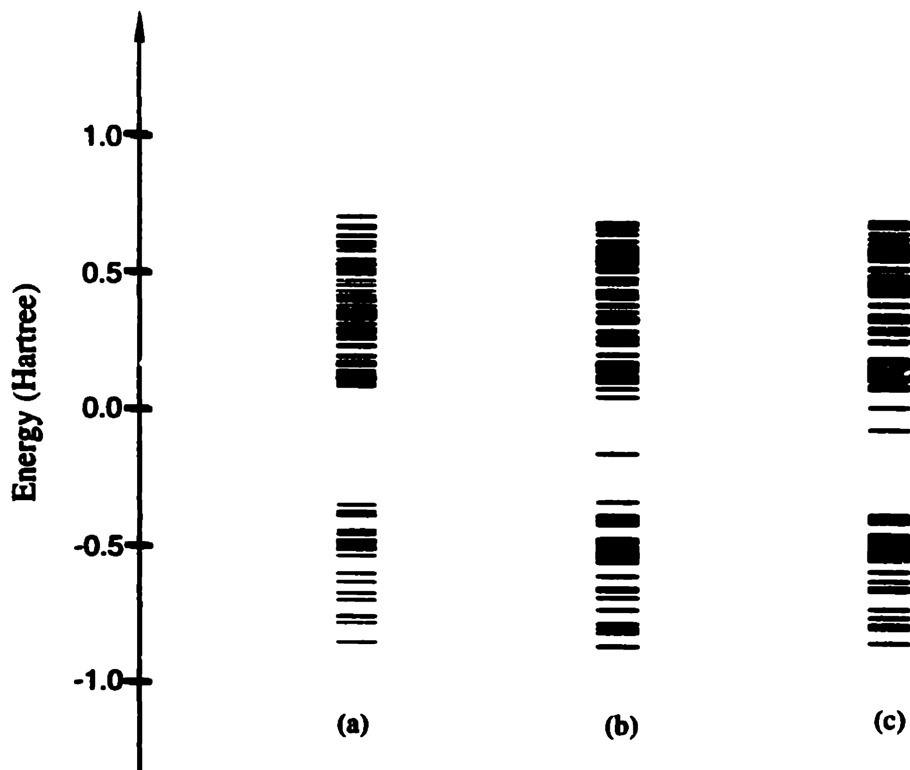

Figure 5-9: Orbital energies for (a) Si_9H_{14}; (b) $Si_9H_{14}Cu$ (alpha electrons) and (c) $Si_9H_{14}Cu$ (beta electrons)

The fact that both metal atoms and silicon dangling bonds introduce surface states in the gap are at the basis of our use of lifetime measurements to detect surface reaction involving metals, oxygen, and halogens. The detection of native oxide growth using *in situ* surface lifetime measurements is discussed in the next section; detection of metal deposition will again be postponed until the next chapter.

5.7 *In situ* measurements of silicon surface reactions using RFPCD

5.7.1 *In situ* monitoring of chemical oxide etching in HF

Experimental

A p-type, SC2-last FZ wafer was immersed in 1:100 HF while its effective lifetime was measured continuously using RFPCD.

Results and discussion

Figure 5.10 shows the measured lifetime and the calculated density of surface states, based on the relationship:

$$N_T = \frac{d}{2\sigma v_{th}\tau_s} \tag{5.19}$$

A capture cross section, σ_n, of 10^{-15} cm^2 was assumed. As shown in Figure 5.10, the surface state density obeys a single exponential decay, indicative of first order reaction kinetics.

As pointed out earlier, the replacement of the chemical oxide by a monolayer of atomic hydrogen in HF is a two step process. In the first step, SiO_2 is rapidly etched by HF molecules. Further reaction leads to removal of silicon as SiF_6^{--}, and oxygen as water[6]. The final OH groups are removed from the surface by the reaction :

$$Si - OH + HF \longrightarrow Si - F + H_2O \tag{5.20}$$

As discussed in Section 5.4.2, the highly polar Si-F bond weakens the silicon backbonds, resulting in the subsequent attack of the backbonds by HF molecules. One layer of silicon is etched and replaced by a monolayer of hydrogen [76].

Since neither hydroxyl nor fluorine introduce gap states. we conclude that the high initial value of N_T is caused by unsaturated surface bonds (Si·). These "dangling" bonds react with H^+ and F^- in solution:

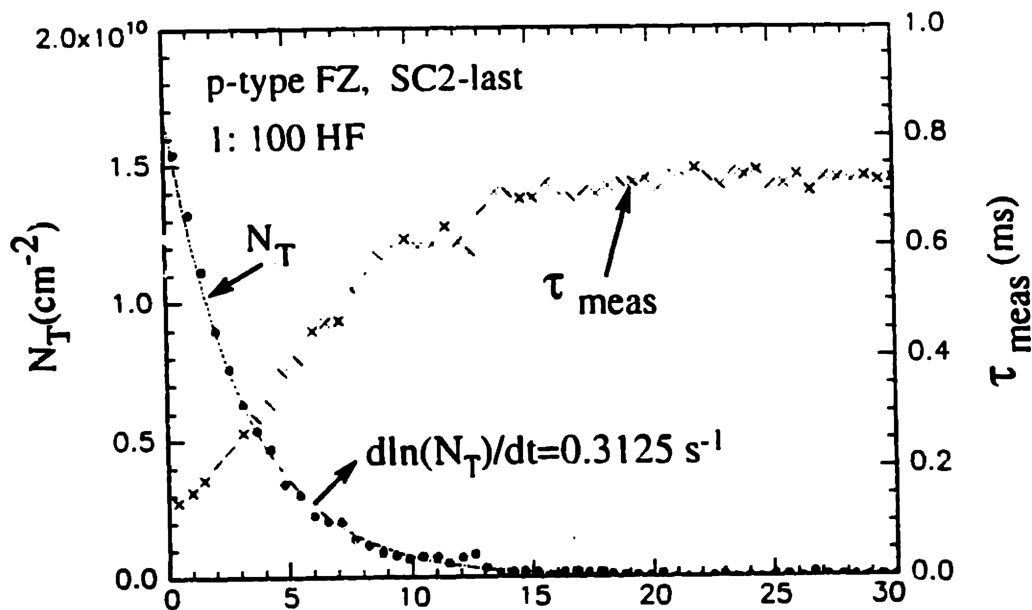

Figure 5-10: The effect of oxide etching and hydrogen termination buildup on the surface lifetime and surface state density of a p-type FZ wafer. The surface state density obeys a single exponential decay with rate constant k_f=0.3125 s^{-1}. A minority capture cross section of 10^{-15} cm^2 was assumed.

$$Si \cdot + H^+ e^-_{cb} \longrightarrow Si - H \qquad (5.21)$$

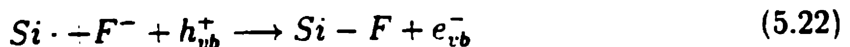

$$Si \cdot + F^- + h^+_{vb} \longrightarrow Si - F + e^-_{vb} \qquad (5.22)$$

The relatively low concentration of F^- and H^+ [7] explains the relative slowness of reactions 5.21 and 5.22 . This is also obvious from the relatively slow increase in lifetime shown in Figure 5.10. The first order kinetics observed suggest a simple rate equation (assuming that the surface concentrations of H^+ and F^- do not change and that N_T=[Si·]):

$$\frac{dN_T}{dt} = -k_f N_T \qquad (5.23)$$

Fitting the lifetime results to Equation 5.23 yields a first order rate constant.

[7] Due to its low pK_a value (3.2), most HF is present in undissociated form.

k_f=0.3125 s^{-1}, for the forward reactions 5.21 and 5.22.

Significance

In this section, we have demonstrated, for the first time, the use of RFPCD for *in situ* kinetic studies of surface reactions on silicon. The ability to monitor the etching and passivation reaction by probing the electronic properties of the silicon surface is unique and has significant potential for application in the fabline.

5.7.2 Measurement of O_2 adsorption on Si-H

Experimental

We studied the reactivity of the H-passivated silicon surface in different ambients. An n-type silicon wafer was cleaned and immersed in 48 % HF for surface lifetime measurement. The HF immersed wafer was placed in a glovebox which was purged with N_2. Subsequently, the wafer was removed from the 48 % HF solution and its minority carrier lifetime was monitored continuously.

Results

Figure 5.11 shows the temporal change of the minority carrier lifetime. The measured lifetime drops from 6.0 ms, measured in 48 % HF, to 1.8 ms, immediately after exposure to nitrogen. The decrease in lifetime during the first 200 seconds and the ensuing increase is characteristic for wafers passivated in 48 % HF. This behavior is not observed for wafers passivated by dilute (1-10 %) HF. After 300 seconds of N_2 gas flow, the lifetime is stable. A stable lifetime is also observed when the passivated wafer is exposed to argon.

After 1250 s, the gas supply was switched from N_2 to O_2. An immediate decrease in lifetime is observed. Two kinetic regions are present as shown in Figure 5.11a: (1) a region of rapid lifetime decrease during the first 40-50 seconds of oxygen exposure (Region I), and (2) a region of slower decrease, lasting more than 10 minutes (Region II). The surface state density vs exposure time, assuming a cross section for surface

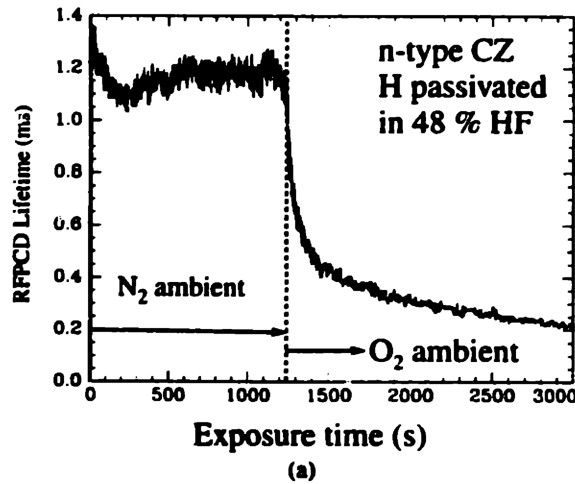

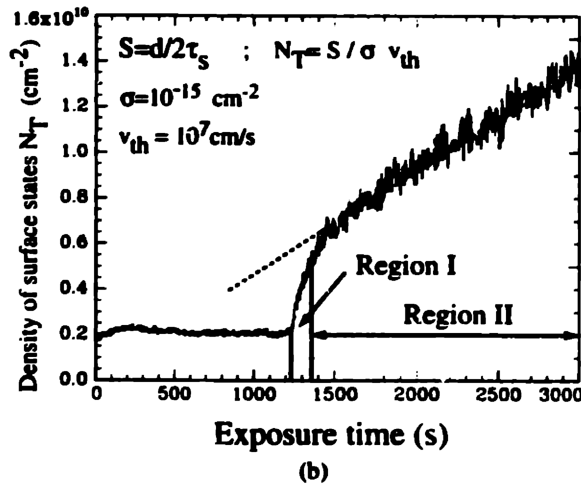

Figure 5-11: (a) The effect of oxygen exposure on the effective lifetime of an n-type CZ wafer. The measurement was started immediately after the wafer was removed from the 48 % HF solution. (b) The density of surface states corresponding to the lifetime measurement shown in Figure 5.11a. A minority capture cross section of 10^{-15} cm^2 was assumed.

recombination of 10^{-15} cm^2, is shown in Figure 5.11.

Discussion

Elsewhere, region I was attributed to the rapid oxidation of poorly passivated sites resulting from structural surface imperfections [26]. The linear decrease in the density of surface states, observed in region II, is discussed here.

As discussed in Section 5.5.1, the condensation reaction of the Si-OH groups to form two silicon dangling bonds and a bridging oxygen occurs rapidly in the presence of moisture:

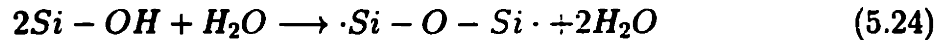

$$2Si - OH + H_2O \longrightarrow \cdot Si - O - Si \cdot + 2H_2O \quad (5.24)$$

where $\cdot Si - O - Si \cdot$ represents a bridging oxygen atom bonded to two silicons with one dangling bond each. The water molecules which catalyze the oxidation reaction are believed to be present on the wafer surface in physisorbed form after the 48 % HF exposure step.

As was pointed out, the formation of Si-OH groups is a slow process because of the high energy barrier associated with the homolytic cleavage by insertion in two Si-H bonds (reaction 5.14 and Figure 5.5). Therefore, in the presence of moisture, the rate of formation of surface states is essentially the same as the rate of formation of Si-OH bonds, because each Si-OH rapidly undergoes a condensation reaction (5.24), introducing a single surface state.

Therefore, the slope dN_T/dt in region II of Figure 5.11b can be used to calculate the sticking coefficient, f, for O_2 on Si(100)-H:

$$f = \frac{\frac{dN_T}{dt}}{2\Phi_o} \quad (5.25)$$

where Φ_o, the flux of oxygen molecules impinging on the surface, is given by:

$$\Phi_o = \frac{p}{\sqrt{mRT}} = 6.8x10^{23} cm^{-2} s^{-1} \quad (5.26)$$

(p=1 atm, m=molecular weight of O_2, R=ideal gas constant, T=300K). From the slope in Figure 5.11b, we determine a sticking coefficient of $f = 3.5 \times 10^{-18}$ for the slow process. This provides a estimate for the barrier height of the Si-H an O_2 bond breaking and Si-OH bond formation process: $-kT\ln f$=1.2 eV. This large barrier height for oxygen chemisorption expresses the extraordinary stability of a hydrogen terminated silicon surface compared to bare silicon.

Significance

Our measurement demonstrates, for the first time, that native oxide growth on HF-passivated silicon (100) starts instaneously upon oxygen exposure. While the RFPCD method does not allow the extraction of chemical information, it boasts an extraordinary sensitivity ($\approx 10^8$ surface states cm^{-2}). Other advantages are its measurement speed and noninvasiveness.

5.8 Conclusions

In this chapter, we discussed the kinetics of surface reactions on monolayer terminated Si (100) based on the results of electronic structure calculations at the Hartree-Fock level. The reactivity of chemisorbed halogens towards polar molecules such as water and HF easily gives rise to etching by backbond insertion (in HF) and the formation of silanol groups by hydrolysis (in air and water). The kinetics of both reactions for the different halogens can be understood based on the bond polarity and bond order of silicon-halogen bons.

Alternative passivation strategies, based on the use of media less polar than water, hold some promise because the suppression of the hydrolysis reaction stabilizes the surface bonds. Nevertheless the bond order results indicate that back bond weakening is a factor for all of the halogens. Even iodine passivation is therefore unlikely to provide a higher resistance to backbond attack than Si-H.

We discussed two ways in which dangling bonds can be introduced. Surface silanols undergo a condensation reaction, catalyzed by moisture, which leads to a

bridgebonded oxygen atom and two silicon dangling bonds. The surface states, introduced by the dangling bonds, are close to midgap and can therefore be detected by means of surface lifetime measurements. Chemisorption of reducible metals such as Cu also introduces surface states, which are due to orbitals localised on the metal atom. Both results will be of significant value for interpreting our experimental results, presented in later chapters.

We presented two examples of the use of RFPCD for *in situ* monitoring of surface reactions on silicon during wet cleaning. An *in-situ* RFPCD study of the etching of SiO_2 and subsequent passivation by hydrogen in dilute HF was used to establish the rate constant of the passivation reaction. We also used RFPCD to study oxygen chemisorption on (100) silicon following passivation in 48 % HF. We used this measurement to calculate a sticking coefficient for oxygen chemisorption. Based on the value of the sticking coefficient ($f = 3.5 \times 10^{-18}$), we obtain an estimate for the energy barrier associated with the chemisorption reaction of O_2 on hydrogen terminated silicon (1.2 eV).

The mechanism for native oxide growth proposed in the present chapter predicts neglegible native oxide growth in the absence of water. While exposure to dry air will introduce Si-OH groups, the formation of "bridging" oxygens will not occur. Removal of physisorbed water molecules from hydrogen passivated surfaces and reduction of moisture in cleanroom air to prevent native oxide growth are therefore promising alternatives to the use of a nitrogen "blanket" during surface preparation.

Chapter 6

Metal Deposition from Hydrofluoric Acid Solutions

6.1 Introduction

The deposition of trace metals from liquid ambients on silicon is a phenomenon with interesting fundamental aspects. In the present chapter, we focus on metal deposition from HF solutions. Deposition from oxidizing solutions will be addressed in the next chapter. Because metal deposition from HF involves charge transfer from the semiconductor to ions in solution, a deep understanding of surface physics and electrochemistry of silicon immersed in HF solutions is required to unravel the various factors affecting the deposition rate. Building on concepts introduced in Chapter 4, we will present a comprehensive thermodynamic model for the deposition reaction. Application of our model has led us to a detailed experimental study of the mechanisms of copper deposition from HF. Based on our experimental results, we suggest new ways to limit contamination risk by improved control over the factors affecting the deposition rate.

We have paid special attention to the effect of surface metals on the surface lifetime, measured by RFPCD. We will demonstrate the use of lifetime measurements to detect metallic contaminants at levels well below the detection limit of existing surface analysis methods. Furthermore we present their use for em in situ studies

to elucidate the mechanisms of metal deposition. To validate our concern with the measurement of extremely low surface contaminant levels. we have also studied the impact of trace metals on the dielectric strength of ultrathin oxides.

6.2 Background

6.2.1 The germanium years

The interest in the chemical basis of surface defects on semiconductors dates back to the early 1950s. In those days, the principal hurdle opposing the breakthrough of germanium as an device material lay in the difficulty of achieving a stable surface passivation, and intensive research efforts were aimed at identifying preparation routes for stable germanium surfaces. The results from this era have been the subject of in-depth reviews by Frankl and Many *et al.* [107, 65]. This early work has provided valuable backgrounds for starting our own investigations in the silicon area. In this section, we highlight some of the milestones in the research carried since since the germanium era.

Brattain and Bardeen (1953) of Bell Laboratories were the first to investigate the interplay between the electrical properties and the surface chemistry of semiconductors. They studied the effect of different gaseous ambients on the surface potential of etched germanium [108]. By cycling an etched germanium surface through a sequence of ambients (the so-called Bardeen-Brattain cycle) they observed surface potential changes, which were explained using the concept of "slow surface states". The many questions which their seminal work left unanswered motivated a host of investigations in the 1950s and 1960s into the electrical properties of etched germanium.

Wang and Wallis (1957) [109] measured the effect of changes in the surface potential on the surface recombination velocity of CP-4 etched germanium. They interpreted their results by assuming the presence of two sets of surface recombination centers, characterized by discrete levels in the germanium bandgap. Many and Gehrlich [110] combined SRV with field-effect measurements to study the effects of

different ambients and different temperatures. They, too, proposed the presence of a discrete spectrum of surface states to explain the changes in surface recombination velocity and surface charge with surface potential.

Frankl (1962) [111, 112] first reported the influence of low levels of deposited copper on the surface state density of etched germanium surfaces. On hydrophobic surfaces, the initial effect of copper on the density of recombination centers is relatively small, but subsequent exposure of the contaminated surface to an oxidizing ambient introduces surface recombination centers. In contrast, the exposure of KOH-treated germanium to a copper containing solution immediately gives rise to a strong increase in surface recombination velocity.

Boddy and Brattain [113] measured the semiconductor-liquid junction capacitance as a function of surface potential. For copper-treated surfaces, they observed an excess capacitance in addition to the contribution from the semiconductor space charge region. They demonstrate the possibility of determining the energy levels of discrete bandgap states using field- and temperature dependent measurements.

Memming (1964) [114] pointed out that the density of adsorbed copper atoms is much higher than the density of surface states and explained this by a deposition mechanism based on decoration of pre-existing surface defects. Margoninski and Gavron (1966) [115] concluded that copper exposure had little effect on the energy or density of the recombination centers, but considerably increased their capture probability for holes. Matsas *et al.* (1970) [116] investigated the formation of surface states on germanium by gold and silver. Gold was observed to drastically increase the surface recombination, while the effect of gold could be neutralized by coadsorption of silver. However, silver itself was not observed to affect surface recombination. The validity of the description of the copper-treated germanium surface in terms of a discrete set of surface states has since been questioned by Fitzgerald and Grove (1968) [64].

6.2.2 Semiconductor electrochemistry

The variety of novel phenomena observed at the semiconductor/liquid interface called for the development of a firm theoretical framework to accommodate the new physics of semiconductor/electrolyte surfaces. In the '60s and '70s, Gerischer [117, 118] and Morrison [119, 120, 121] made important contributions to the theoretical description of the semiconductor surface in terms of bands, surface states and ion levels in solution. Morrison suggested the use of redox potentials as approximations for the ion levels in solution, using the value of the standard hydrogen potential on the vacuum scale to allign ion and band energies. Gerischer proposed tunnelling between electron states in the semiconductor and ion levels in solution as the dominant mechanism for interfacial charge transfer.

6.2.3 Metal-decorated semiconductors for liquid-junction photovoltaics

A surge of interest in the chemistry and physics of metals on silicon surfaces developed in the late '70s and early '80s in the photovoltaics (PV) research community. Attracted by the prospect of using the semiconductor/liquid junction to separate photoexcited carriers, several research groups set out to design redox solution systems capable of carrying the photogenerated current via a photocathode into an external circuit, a process known as photoelectrochemical energy conversion. PV research focused on ways to *improve* the efficiency of liquid junction solar cells by decorating the surface with nanometer-sized noble metal clusters, deposited from solution [1]. Metal clusters can perform very effectively as "scavengers" of photoexcited holes, quickly transferring them into the redox system in solution. Decoration of the semiconductor surface with microscopic metal clusters can therefore increase internal quantum efficiency and reduce photocorrosion of the semiconductor anode by photoholes. Allongue [122] reviewed the results of these research. Large number of

[1]This type of plating reaction, where the electrons for the reduction reaction are supplied by oxidation of the electropositive substrate, is oftentimes (incorrectly) referred to as *electroless plating.*

semiconductor/metal systems were investigated, including GaAs, InP, GaP, Si, and TiO_2 decorated with Ru, Pt, Pd, and Cu. Even though different applications are targeted here, our research builds on the same scientific knowledge base contained as the photoelectrochemical solar cell research.

6.2.4 Metallic contamination in silicon wafer cleaning

The tendency of copper and the noble metals to deposit from HF solutions onto the surface of semiconductors has been realized since the early days of semiconductor technology. In fact, the preferential deposition of copper on the n-type regions of a junction is widely used to decorate junctions by immersion in a copper nitrate/HF solution [123]. Since the introduction of VLSI, the deleterious effect of residual metallic contaminants in front-end processing has been realized. Due to the recent trend towards HF-last processes for pre-gate cleaning, trace metal deposition from dilute HF has attracted much attention in recent years. Copper, a common background contaminant with a high tendency to deposit from dilute HF solutions, has been investigated quite thoroughly in this context [124, 125, 126, 127, 128, 43, 44].

Among the various authors, there is a general agreement that copper and the noble metals deposit onto silicon by an electrochemical reduction mechanism, which involves simultaneous oxidation of the silicon by dissolution:

$$M^{z+} + ze^- \longrightarrow M^o \qquad (6.1)$$

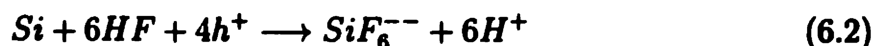

$$Si + 6HF + 4h^+ \longrightarrow SiF_6^{--} + 6H^+ \qquad (6.2)$$

This mechanism explains why deposition is only observed for copper and the noble metals, which have the highest standard oxidation potentials. AFM and SEM observations revealed that copper is present on the wafer surface as nanometer sized precipitates, while gold forms monolayer deposits. Pitting of the silicon surface (the so-called "MIP", metal-induced pit), as a result of localised silicon etching (reaction 8.2) underneath metallic precipitates has been confirmed by AFM, lending further

support to a straightforward corrosion-like deposition mechanism.

Teerlinck et al. [128] studied the effect of doping type and illumination level on copper deposition. They observed several orders of magnitude difference between the deposition rate in the dark and under high intensity illumination, while no significant differences between n and p-type could be detected. Large effects of trace amounts (ppb) of bromine and/or chlorine on the copper deposition level have been reported [125].

Several authors have reported that the copper deposition is rate controlled by ion diffusion through the stationary boundary layer [43, 44]. However, a major deficiency of most of the cited research is that very high copper concentrations (1-50 ppm) were used to facilitate observations by SEM and AFM. Indeed. since the highest copper concentrations in a high purity wafer cleaning environment are typically three orders of magnitude lower, the relevance of these results to today's wafer cleaning technology have been questioned.

6.3 Model for metal deposition onto hydrogen-terminated silicon from HF solutions

6.3.1 Thermodynamics of metal reduction at silicon

A simplified model for the energetics of metal ion reduction at the the semiconductor/electrolyte interface is shown in Figure 6.1. By relating both the energy levels of the ions and the silicon bandedges to the vacuum level. the allignment of the ion levels in solution with the silicon bands can be determined. The energy levels of ions in solution depend on their concentration in solution and are given by the Nernst relationship[2]:

$$E = -eE_{o,vac} - \frac{eRT}{nF} ln \left(\frac{M_{ox}}{M_{red}} \right) \tag{6.3}$$

[2]Because the solutions are extremely dilute in the metal ion, we may assume that activities equal concentrations.

where E is energy level of the electron when "occupying" an ion in solution; $E_{o,vac}$ is the oxidation potential of the ion at standard concentration (1 M), measured on the vacuum scale; and M_{ox} and M_{red} are the molarities of the oxidized and the reduced form of the ion.

The representation of redoxlevels and semiconductor bands on the same energy scale is due to Morrison [121], and has the great advantage of combining the formalisms of classical electrochemistry (redox levels) and surface physics (energy bands and surface states). Morrison's approach is a somewhat simplified version of the formalism proposed by Gerischer [3] [118]. Gerischer introduced a so-called "Fermi level in solution", essentially the equilibrium Nernst potential of the redox couple on the vacuum scale [4]. The driving force behind the interfacial charge transfer reaction is given by the difference between the "fermi level in solution" and the usual fermi energy inside the semiconductor.

Charge in surface states will cause the carrier concentrations in the bulk to deviate from the values in the bulk of the semiconductor. Upward bandbending, indicative of negative surface charge, lowers the position of the fermi level inside the semiconductor with respect to the ion levels; hence the driving force for electron transfer into solution is decreased. Similarly, positive surface charge will lead to an increase in the driving force for ion reduction.

Our calculation of the alligment of redox couples with the silicon bands, as shown in Figure 6.1, is based on the following assumptions:

- The concentration of metal ions in solution is 1 ppb.
- All calculations were performed for dark conditions (E_F=E_{Fn}=E_{Fp}).
- A value of the standard hydrogen potential (SHP) on the vacuum scale of 4.5 V was assumed [129].

[3] Like Morrison, we will neglect the shift in energy position ('reorganization energy') which occurs as a result of the electron transfer.

[4] Because the "electrons in solution" are bound to ions, the fermi nomenclature is somewhat controversial.

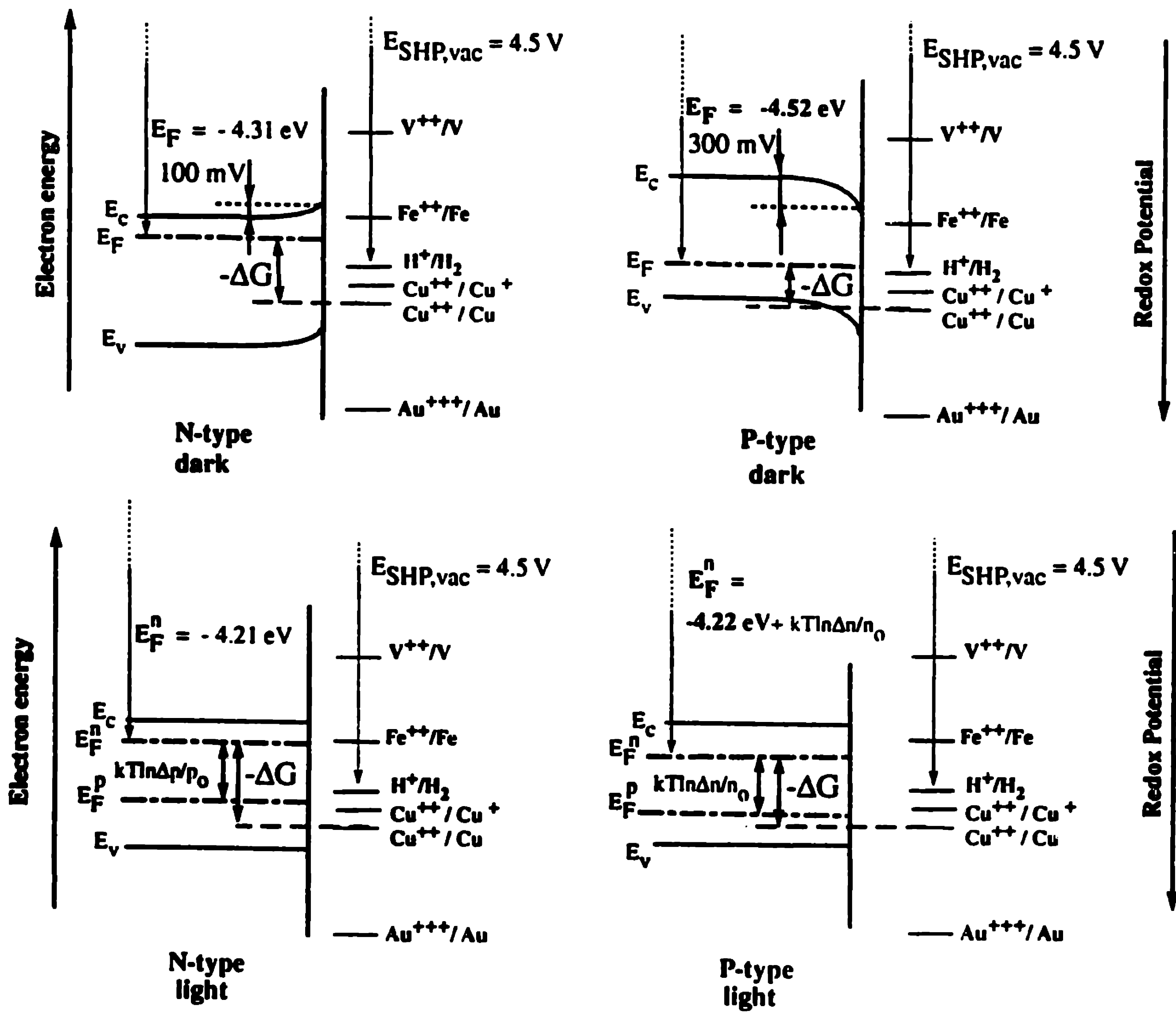

$$\frac{\Delta G}{n} = -(E_C + kT\ln(N_A/N_C) - e\phi_S + kT\ln(\Delta n/n)) + (eE_{SHP,vac} - eE^{o}_{M^{z+}/M} - e\frac{RT}{nF}\cdot\ln M^{z+})$$

Figure 6-1: A simple band model for the reduction of metal ions from solution.

- The dopant concentration is $N=10^{15}$ cm^{-3} (light doping), resulting in E_c-E_f=300 mV for n-type and E_f-E_v=280 mV for p-type.

In order to obtain the correct value of the bandbending potential in the dark, we have performed photovoltage measurements on wafers immersed in 1:100 HF solution using a potentiostat [67]. High frequency, high intensity light pulses from a Strobotac 1538-A strobe light [5] were used to flatten the bands. while the open circuit potential (OCP) was measured using a calomel reference an Pt counter electrode. Because the surface recombination is small for silicon immersed in dilute HF ($\approx$ 10 cm/s), the difference between the dark and light OCP values provides a good estimate of the bandbending potential, ϕ_s. The following estimates for the bandbending potential in the dark were obtained: ϕ_s=300 mV on p-type wafers (type III) and ϕ_s=100 mV for n-type (type I) (positive values are defined as bandbending into depletion).

From Figure 6.1, we immediately conclude that reduction of ions from solution will only occur for ions with a sufficiently positive standard reduction potential. Because the ion energies depend on the ion concentrations by Equation 6.3, the driving force for deposition will decrease as the ion concentration is reduced also. As discussed in Chapter 4 of this thesis, the effect of very low intensity illumination will be to flatten the bands [6]. For n-type bands in depletion, flattening the bands will lift up the quasi fermi level for the electrons and, hence, increase the driving force for ion reduction [7] For p-type bands is depletion, flattening the bands will not affect the quasi fermi level for the electrons, when the surface recombination velocity is small. For illumination beyond flatband, the quasi fermi levels will move up with respect to the ion levels, regardless of doping type, and the effect of the light will therefore be to increase the driving force. Detailed calculations of the driving force will be presented later in this chapter.

The band diagram shown in Figure 6.1 only represents the energetics of the *ca-*

[5] Quad-Tech (Marlborough, MA).

[6] We are making the same assumptions as stated in Section 4.3.1.

[7] We assume reduction occurs by a conduction band mechanism. If the charge transfer from the valence band, the hole quasi fermi level hav to be considered to determine the driving force for deposition.

thodic reactions [8] The question arises whether driving forces calculated based on the banddiagram are "real". since they do not include the anodic halfreaction. Because in this work we only consider low concentrations of metal ions in solution (10 ppb - 1 ppm), we may in general assume that the anodic reaction (silicon dissolution) will not limit the rate of the reduction reaction. In this case the free energy change of the cathodic halfreaction, as obtained from the banddiagram, will effectively control deposition.

6.3.2 Kinetics of metal reduction at silicon

According to Gerischer [118], the reduction of a metal ion from solution occurs by tunneling of an electron from a filled electron state in the semiconductor to an empty ion level, at the same energy, in solution. The filled electron state can be:

- a state in the conduction band;
- a filled surface state with an energy level in the gap:
- a state in the valence band, in which case the electron capture process by the ion in solution is equivalent to the injection of a hole into the valence band.

Because of the low positions of the gold levels on the vacuum scale, we predict that gold reduction will occur by hole injection into filled valence band states. Because the energy level of the ion in solution overlaps with a high density of filled valence band states, rapid reduction of the ion is expected following physisorption.

Because copper is present as a divalent ion in HF solution [127], its reduction must necessarily involve to separate reduction steps, $Cu^{++} + e^- \longrightarrow Cu^+$ and, subsequently, $Cu^+ + e^- \longrightarrow Cu^o$. Thus, representation of the copper reduction reaction on a band diagram requires the consideration of two distinct ion levels, as shown in Figure 6.1.[9]

[8] If no *anodic* reaction (equation 6.2) were present to provide the electrons consumed by the metal reduction, charge inbalance between the substrate and the solution would result, giving rise to a large potential which opposes further deposition.

[9] Unfortunately, the precise position of the Cu^{++}/Cu^+ redox level with respect to the silicon bands cannot be established precisely, because of the $\frac{[M_{ox}]}{[M_{red}]}$ ratio is not known. For convenience, we will assume $\frac{[M_{ox}]}{[M_{red}]}=1$.

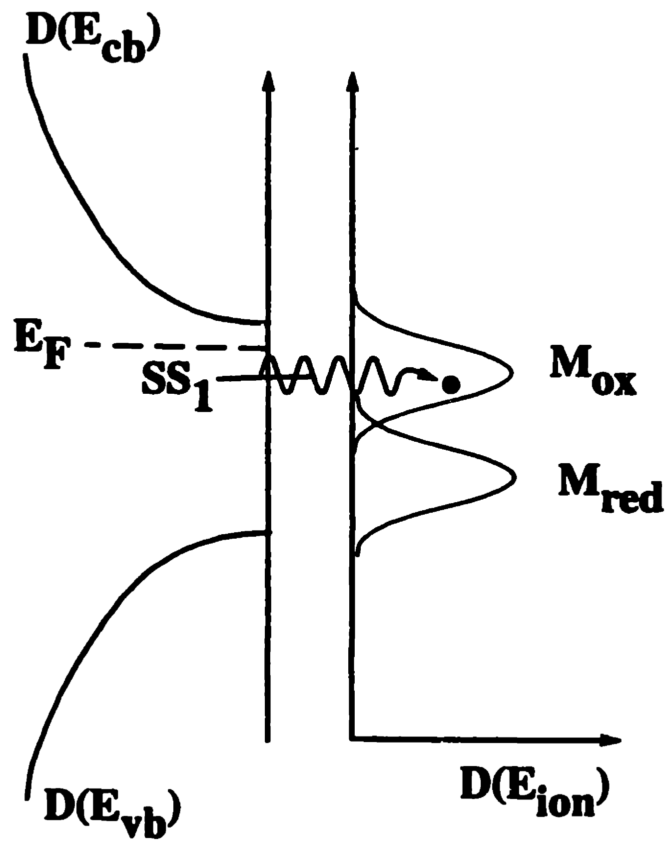

Figure 6-2: The Gerischer mechanism for oxidoreduction reactions at the semiconductor/electrolyte interface.

From the study of copper electrodeposition on metallic substrates, it is well known that the first step is rate limiting in the overall reduction process [130]. Since the redox level of the rate limiting step, $E_{Cu_{++}/Cu_{+}}$, is near the middle of the silicon bandgap, charge transfer necessarily involves surface states. The low density of surface states (of the order of 10^9 cm^{-2}) for silicon immersed in dilute HF leads us to expect a much lower reduction rate for copper, than for gold ions.

6.3.3 Growth of metallic precipitates on silicon

In the previous sections we focused on the reduction reactions of metal ions at the silicon/cleaning solution interface. For certain metals, notably copper, this reduction reaction cannot occur atom by atom because of the small driving force, and reduction occurs by nucleation of metallic clusters. The presence of these clusters introduces a second deposition mechanism: reduction of metal ions at the metal/solution interface. The deposition of metal ions on existing nuclei will be balanced by silicon dissolution, as expressed by the following corrosion reaction for the case of copper:

$$Si + 6F^{-} + 2Cu^{++} \longrightarrow SiF_6^{--} + 2Cu \tag{6.4}$$

Because of the high driving force of this reaction (ΔG^o=-160.4 kcal/mol) the kinetics of ion reduction at the copper precipitate/solution interface will usually be limited by ion diffusion in the liquid.

6.4 Experimental results

6.4.1 Deposition tendencies for various metals

Experimental

After the standard MIT clean, wafers were immersed for 10 minutes 1 % HF solutions deliberately contaminated with 1 ppm Fe, V, and Cu, and 100 pb Au respectively. Before and after immersion, minority carrier lifetime measurements were performed

in 48 % HF using RFPCD. Care was taken to limit the exposure to ambient air to a few seconds during transfer between solutions.

Results and discussion

The results of these experiments are shown in Figure 6.3 and Table 6.1. Figure 6.3 shows the time dependence of the effective lifetime measured in 48 % HF for V, Fe and Cu exposure; Table 6.1 shows the standard reduction potential, E^o; the exposure step; the lifetime measured after the exposure to 48 % HF and the thermodynamic driving force, for the respective ion concentrations in solution. To calculate the driving force, we started from the band allignments shown in Figure 6.1. We assumed a doping level of $10^{15}cm^{-3}$, and an injection level, resulting from normal cleanroom lighting, of $10^{13}cm^{-3}$ [10] The calculation is further based on concepts discussed in Chapter 4 and on the measured values for the bandbending on n- and p-type material in the in the dark (Section 6.3.1).

For Fe and V, the lifetime recovers to the original high (5.0 ms) after exposure to the contaminated solution. For Cu (Figure 6.3 and Table 6.1) and Au (Table 6.1) there is a clear lifetime decrease as a result of the immersion in the contaminated solution. Since the deposition of copper and gold from dilute HF onto silicon was reported earlier [131, 132, 124], we conclude that the reduction of of metal ions through reaction (6.1) introduces surface states in the silicon bandgap, which give rise to a degradation of the effective lifetime. After the RFPCD measurement, TXRF analysis of the the copper contaminated wafer revealed a surface Cu concentration, N_{Cu}, of 15.10^{10}atoms/cm^2, confirming that Cu deposits from dilute HF solution. For Fe and V, no lifetime decrease is observed and we conclude that these ions, while likely physisorbed at low concentrations onto the hydrogen terminated surface, do not undergo reduction.

[10]This value is an estimate, obtained by a photocell measurement.

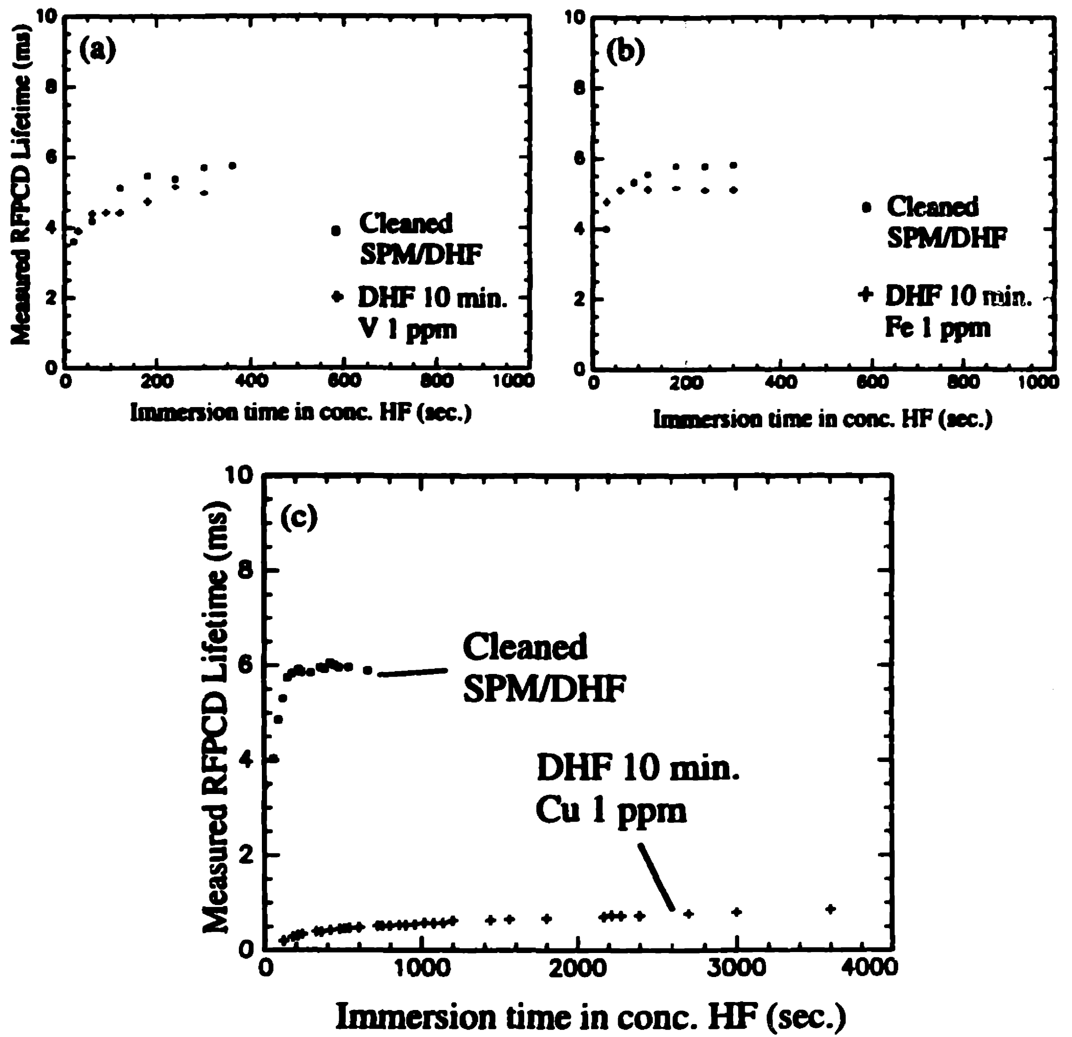

Figure 6-3: The effect of immersion in a contaminated solution on the surface lifetime. The wafers were immersed in 1:100 HF solutions containing 1 ppm of V, Fe and Cu ions respectively.

Redox system	E°	Exposure	τ_{meas}	ΔG (meV)
Au^{+++}/Au	1.692	100 ppb, 5 min.	0.028 ms	-1,402
Cu^{++}/Cu	0.337	1 ppm, 10 min.	0.220 ms	-259
Fe^{++}/Fe	-0.440	1 ppm, 10 min.	5.0 ms	520
V^{++}/V	-1.175	1 ppm, 10 min.	5.0 ms	1,258

Table 6.1: Standard reduction potential, surface lifetime, 1:100 HF exposure conditions, and calculated driving force for the cathodic reaction.

Significance

The deposition tendency (as established by the RFPCD measurement and TXRF) of the various ions is in excellent agreement with the thermodynamic driving force, as calculated based on the banddiagram (Figure 6.1). Our model is based entirely on measurable physical quantities (doping level, doping type, illumination level, band-bending potential and ion concentration in solution) and tabulated thermodynamic properties (E° of the metal and the value of the standard hydrogen potential on the vacuum scale).

6.4.2 *In situ* detection of copper deposition from HF

Experimental

After performing the standard MIT clean, an n-type wafer was immersed in 1:100 HF and the lifetime measured. After 250 seconds, a controlled amount of copper ions was added so as to obtain a copper concentration of 10 ppb in the measurement solution.

Results and discussion

The effect of the copper deposition on the measured lifetime is shown in Figure 6.4. As the copper deposition reaction proceeds, the measured lifetime decreases as a result of surface states introduced by the copper. To eliminate the possibility that the small amount of nitric acid, added to the measurement solution together with the copper ions, might be the cause behind the lifetime decrease, we replicated the measurement, adding the same amount of nitric acid *without* the copper. The lifetime remained high and stable, proving that the lifetime degradation is due to copper deposition.

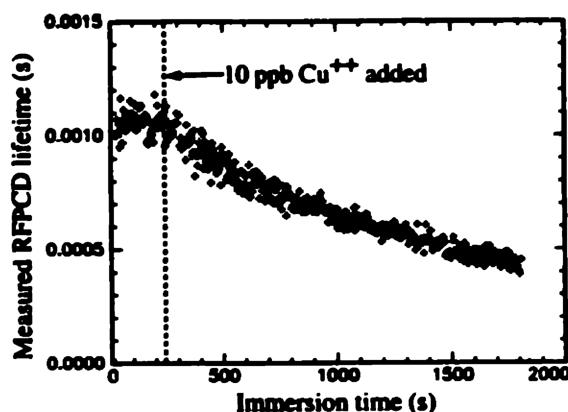

Figure 6-4: In-situ detection of copper deposition from a 1:100 dilute HF solution.

Relevance

Our discovery that surface lifetime measurements can be used to detect low levels of metals on silicon surfaces while immersed in a dilute HF solution is of considerable technological interest. Integrated into an industrial wet bench, RFPCD can be used for *in situ* monitoring of cleaning effectiveness, eliminating the need for frequent TXRF measurements on "monitor" wafers to control bath purity. To assess the applicability of RFPCD as an in-line surface purity monitor, the detection limit of the RFPCD measurement for surface metals and the relationship between surface lifetime and metal coverage are important issues, which will be dealt with in detail in later sections.

6.4.3 Effect of chloride ion on copper deposition from HF

Experimental

After performing the standard MIT clean, an n-type wafer was immersed in 1:100 HF and the lifetime measured continuously. After 800 seconds, a controlled amount of chlorine ions was added as HCl (Section 3.5.4) so as to obtain a chlorine concentration of 2 ppm in the measurement solution. After 1000 seconds, copper ions (10 ppb) were added to the solution as described earlier. The wafer was left exposed to the copper containing solution for 3200s, before being removed for TXRF analysis. In a second experiment, a n-type wafer underwent the same treatment, except that no chlorine was added to the solution. Care was taken to ensure that the same amount of nitric acid was added with the copper ions for both experiments [11]. After completion of the TXRF analysis, several 10x10 μm AFM images were taken from the center area of both wafers. Typical AFM images for each of the wafers are shown in Figures 6.6 and 6.7.

Results and discussion

As shown in Figure 6.5, addition of chloride to the measurement solution instantaneously reduces the surface lifetime. As discussed in Chapter 5, chlorine forms a polar bond with the silicon, weakening the silicon backbond. Since termination of the silicon by chlorine does not introduce states in the bandgap, the decrease in surface lifetime after chloride addition must be the result of surface states, introduced by dangling surface bonds. The observed appearance of surface states upon chlorine addition suggests that chlorine inserts in the silicon backbond, introducing a dangling bond (Si·):

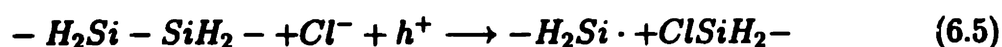

$$-H_2Si-SiH_2-+Cl^-+h^+\longrightarrow -H_2Si\cdot+ClSiH_2- \quad (6.5)$$

[11]Nitric ions are oxidizing and reduce the deposition rate by pulling the silicon bands downward with respect to the energy levels of the ions in solution. Failure to maintain the nitric acid concentration (typically a few ppm, due to the addition of the AAS solution (Section 3.5.4) constant in both experiments, might have led to differences in the deposition rate due to nitric, not chloride, ions.

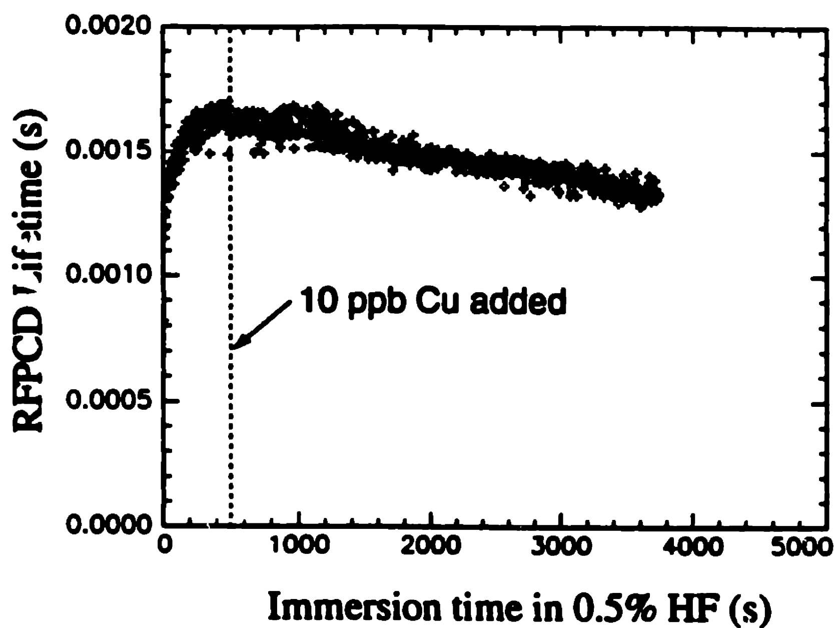

(a)

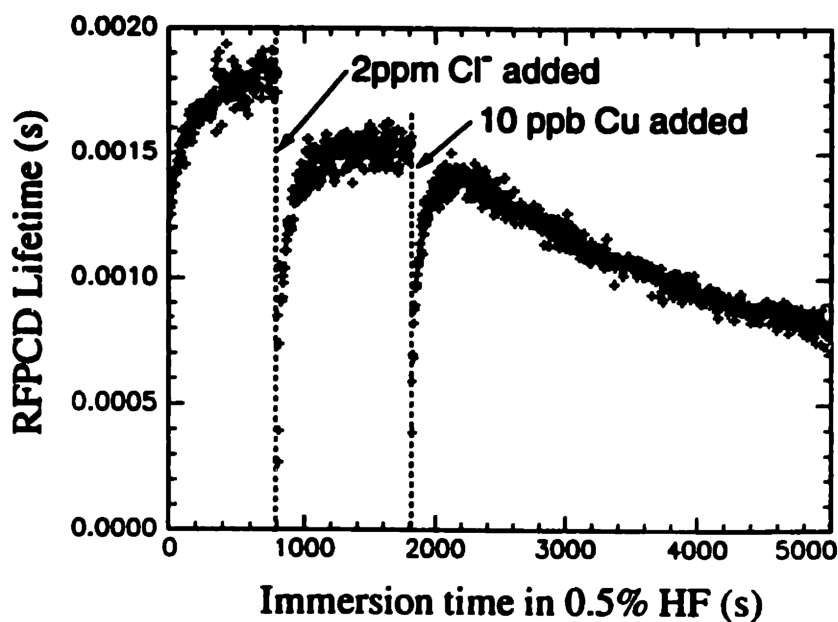

(b)

Figure 6-5: Effect of chloride ion on copper deposition from dilute HF. (a) Wafer exposed to 10 ppb Cu^{--}. no Cl^{-}; (b) wafer exposed to 10 ppb Cu^{++} and 2 ppm Cl^{-}.

Once a surface silicon is bound to Cl, it is quickly etched because the remaining backbonds are broken by insertion of HF, as discussed in Chapter 5. To explain the gradual recovery of a high lifetime, shown in Figure 6.5b, we propose that surface states are being removed from the gap, by the following reaction:

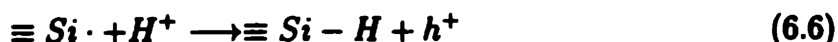

$$\equiv Si \cdot + H^+ \longrightarrow \equiv Si - H + h^+ \tag{6.6}$$

A closer study of the decrease in lifetime as copper deposits reveals an effect of chlorine on the copper deposition rate. Indeed, with 2 ppm chlorine, the surface lifetime decrease occurs at about twice the rate compared to the no chlorine case. Even though both wafers where exposed to the copper containing solution for the same amount of time, the final copper level was determined by TXRF to be $(360\pm250)\text{x}10^{10}\text{cm}^2$ for the wafer immersed in the solution containing 10 ppb copper and 2 ppm chloride ions, as compared to $(58\pm41)\text{x}10^{10}\text{cm}^2$ for the wafer exposed to the 10 ppb solution [12].

As shown in Figure 6.6 and 6.7, AFM analysis of both wafers after the TXRF measurement revealed that copper is present on the wafer as precipitates, with the density of precipitates highest for the wafer exposed to chlorine contamination [13].

A decrease of the overpotential of the $\text{Cu}^{++} + 4e^- \longrightarrow \text{Cu}^+$ reaction was reported earlier [130]. This effect might well explain the increased deposition rate of copper in the presence of chlorine ions, as reported here. An alternate possibility is that a reduction in the overpotential of the anodic reaction (increase in the silicon dissolution rate, as expressed by reactions (5.9)-(5.11)) lowers the rest potential of the silicon, thereby increasing the thermodynamic driving for copper deposition.

[12] The errors are standard deviations over the 5 TXRF measurements (center point + 4 symmetrical positions.)

[13] This observation proved consistent over 5-6 different images taken for both wafers at random locations near the centerspot.

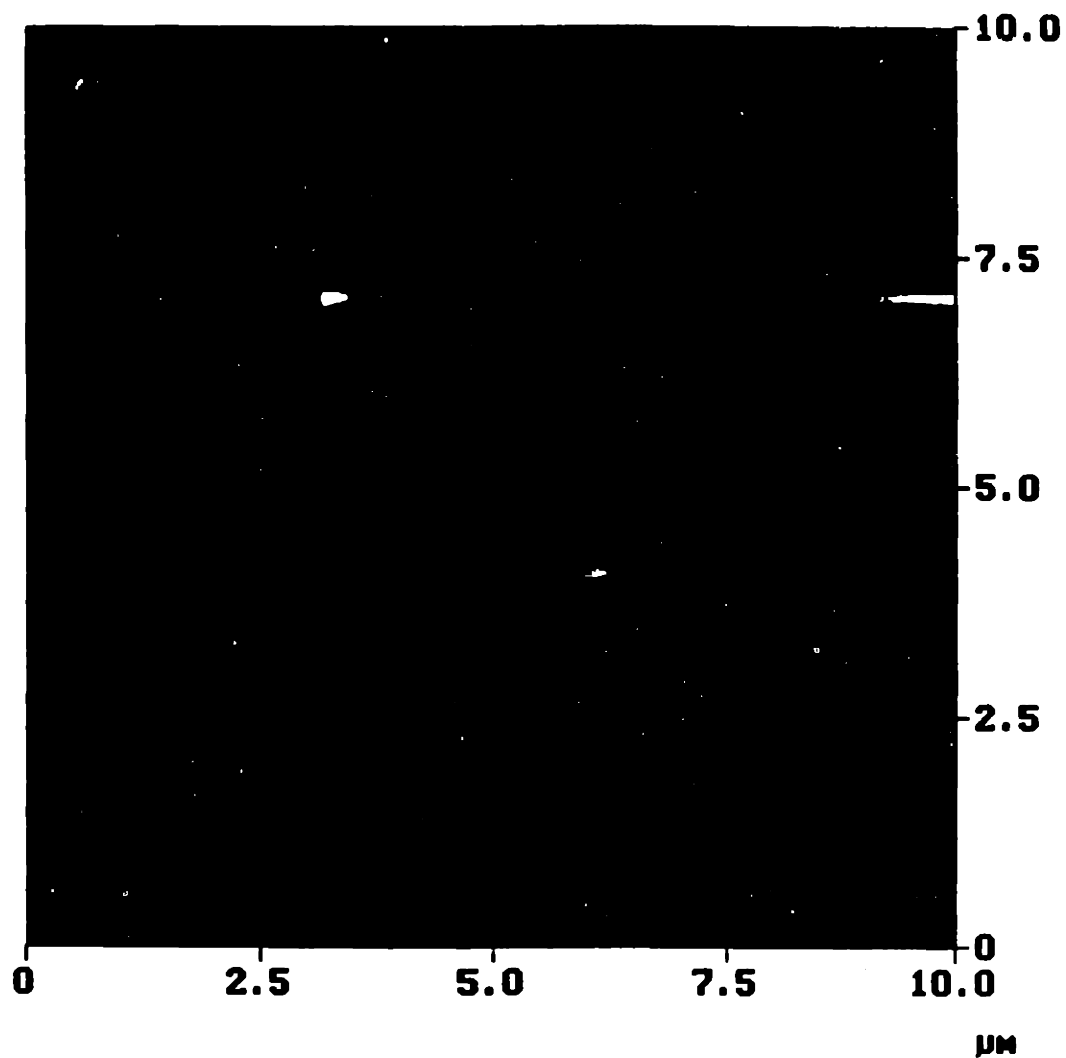

Figure 6-6: 10x10μm AFM image of the sample exposed to 10 ppb Cu in 1:100 HF for 3200s. 2 ppm Cl^- added to solution.

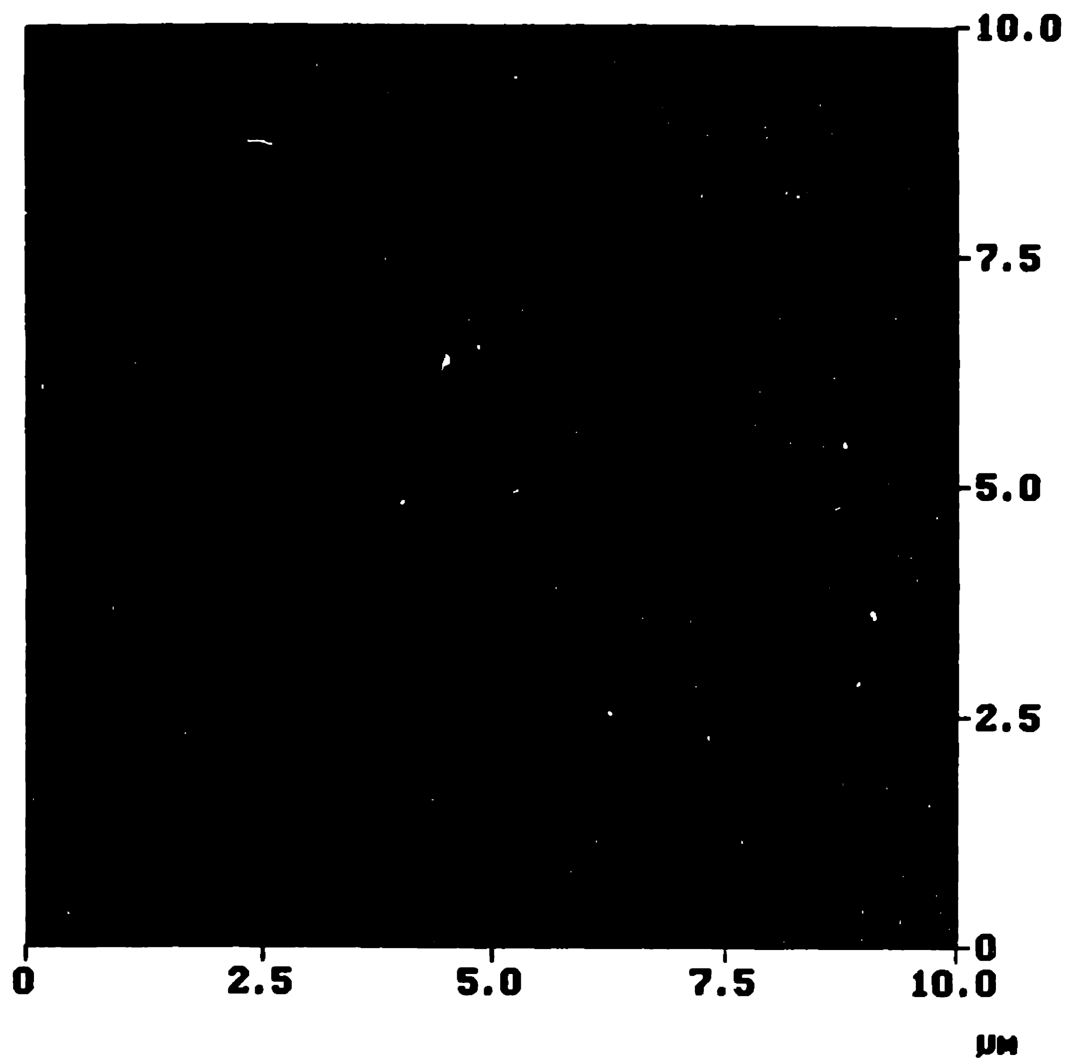

Figure 6-7: 10x10μm AFM image of the sample exposed to 10 ppb Cu in 1:100 HF for 3200s, no Cl^- added.

Relevance

A strong dependence of the copper deposition rate on the presence of various anionic species was reported by Aomi [125]. Notably Br^- and Cl^- where observed to strongly enhance copper deposition, whereas HNO_3 was observed to reduce the deposition rate. To our knowledge, the measurements reported here represent the first confirmation on the effect of chloride ions on the copper deposition rate.

The effect of chlorine on the deposition rate is reflected in the *in situ* surface lifetime results also. These were shown to be in qualitative agreement with AFM and TXRF data. The detection limits of the surface lifetime measurement will be investigated in greater detail in later sections of this chapter.

6.4.4 In situ detection of gold deposition from HF

Experiment

Because of the strong effect of gold on the surface lifetime, as obvious from Table 6.1, we performed an *in situ* RFPCD measurement to compare its deposition kinetics to copper. A p-type wafer, prepared in the usual way, was immersed in 1:100 HF and the lifetime measured continuously. As shown in Figure 6.8, the addition of 10 ppb gold to the measurement solution results in a precipitous drop in the surface lifetime. Comparison of Figure 6.8 with Figure 6.5b indicates a much faster lifetime degradation, by roughly two orders of magnitude, by gold than by copper ions in solution [14].

Results and significance

The much higher deposition rate observed for gold ions is in excellent agreement with our predictions, based on thermodymamic and kinetic arguments, presented earlier in this chapter. Ready deposition of gold from HF solutions on to silicon, was

---

[14]Because Au^{+++} was added as $AuCl_3$, we have to take into account the possible effect of chloride ions (about 2 ppm) on the gold deposition rate. A comparison should therefore be made with the copper experiment where 2 ppm chlorine was deliberately added.

reported earlier by Kuisl *et al.* [132] and Chazalviel *et al.* [131]. Chazalviel, using photovoltage spectroscopy techniques, also reported the introduction of surface states by the chemisorbed gold. AFM studies of gold deposition on silicon have revealed deposition by monolayer growth [133], consistent with the atom-by-atom deposition mechanism suggested earlier.

6.4.5 Dependence of gold deposition rate and surface lifetime on immersion time

Experimental

Both n and p-type wafers (type II and III) were exposed to 1:100 HF solutions containing gold concentrations ranging from 10 ppb to 100 ppb, while exposure times were varied between 5 seconds and 1 minute. Wafer preclean and preparation of the contaminated solution was performed in the usual way. In a related set of experiments, p-type wafers (type II) were immersed for times ranging from 15 s to 1 min. to solutions containing 10 and 50 ppb, and analyzed with TXRF.

Results and discussion

The surface lifetime results, measured with RFPCD, are summarized in Figure 6.9. Figure 6.10 shows the gold coverage obtained from the TXRF measurements on the p-type wafers. Both the lifetime and the TXRF results are consistent with an atom-by-atom deposition process, as predicted from the allignment with the silicon bands. The deposition reaction is limited by diffusion in the liquid, as expressed by the Cottrell equation:

$$N_{Au}(t) = 2 \cdot D^{1/2} C \pi^{-1/2} t^{1/2} \tag{6.7}$$

Since $N_T = N_{Au}$ for atom-by-atom deposition, this explains the $t^{-1/2}$ dependence of the surface lifetime, as seen in Figure 6.9.

We have used the literature value for the diffusion constant of the $Au(CN)_4^-$ ion

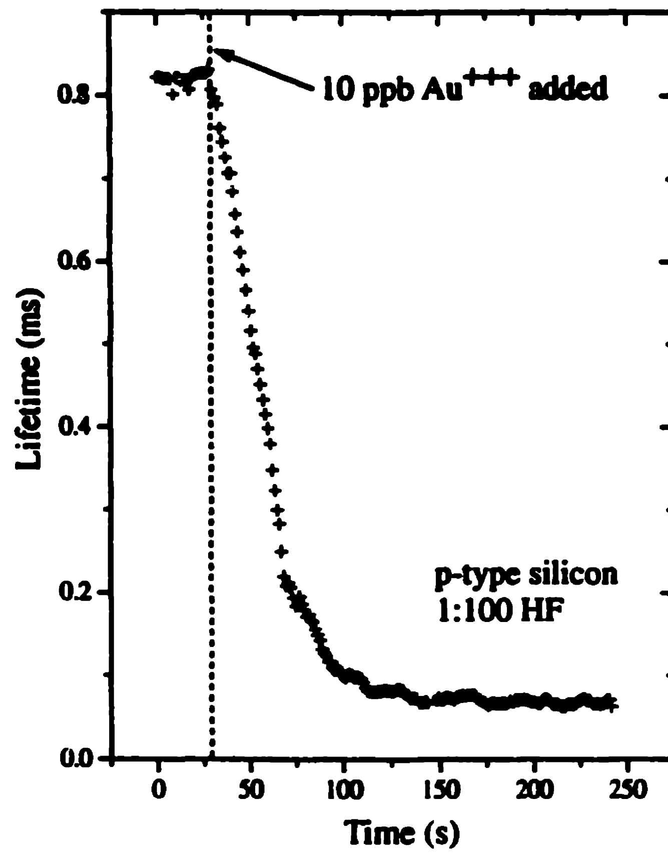

Figure 6-8: In-situ detection of gold deposition from a 1:100 dilute HF solution.

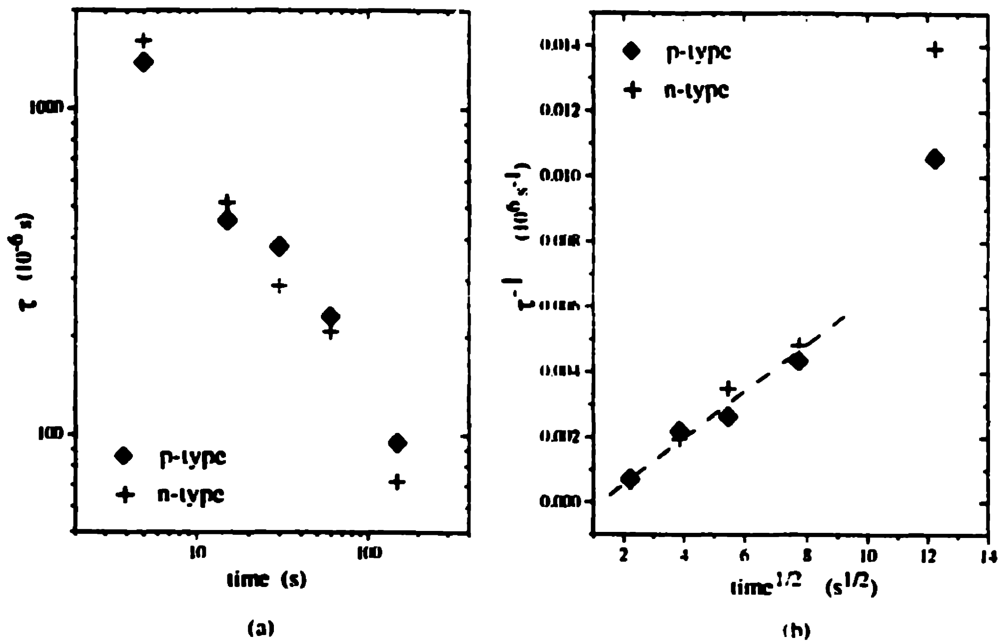

Figure 6-9: Variation of surface lifetime, τ, with immersion time, t, plotted as (a) log τ vs log t and (b) $1/\tau$ vs $t^{1/2}$. The solutions contained 10 ppb Au^{+++} as $AuCl_3$. The wafers were measured by immersion in 48 % HF immediately after the contamination treatment.

($9.7 \times 10^{-6} cm^2/s$ [134]) to determine the cross section for minority capture, σ, from a fit of the Cotrell equation to the surface lifetime data. We obtain a value $\sigma_n^{Au} = \sigma_p^{Au} \approx 10^{-17}$ cm^{-2}. When the wafer is left in the solution for longer times and the solution is stirred, the Cotrell equation does not hold anymore because the stagnant layer is disrupted. In that case, a larger deposition level is observed than expected based on the diffusion limit. This explains the deviation from the Cottrell equation for the longest exposure time (Figure 6.5 b).

6.4.6 Effect of doping type on copper deposition rate

The surface state mechanism proposed earlier in this chapter for the copper deposition reaction suggests a dependence of the copper ion reduction rate depending on the density and filling of surface states. The filling of the surface states depends on the position of the fermi level in the gap, and, hence, on the driving force for deposition. To further investigate the details of this mechanism, we performed a series of experiments to analyse the effect of various factors on the deposition rate. The factors considered are summarized in Table 6.2.

Experimental

Clean wafer surfaces were prepared using the standard MIT cleaning treatment described in Section 3.6.3 of Chapter 2 [15]. Cleaned wafers were exposed to HF solutions containing controlled amounts of Cu^{++} ions. After the exposure step, the wafers were placed in 48% HF for RFPCD measurement. No DI rinsing was performed between the exposure to the copper containing solution and the measurement. Care was taken to minimize the exposure to ambient air to a few seconds during transfer between solutions. After a short (typically 2 minutes) stabilization period, RFPCD measurements were taken under low level injection conditions. Lifetime values were obtained by single exponential fit to the full decay curve. Next, the wafers were briefly rinsed in DI water, dried in a nitrogen gun, and stored in Fluoroware^{TM} single wafer carriers

[15]Type I (n-type) and type II (p-type).

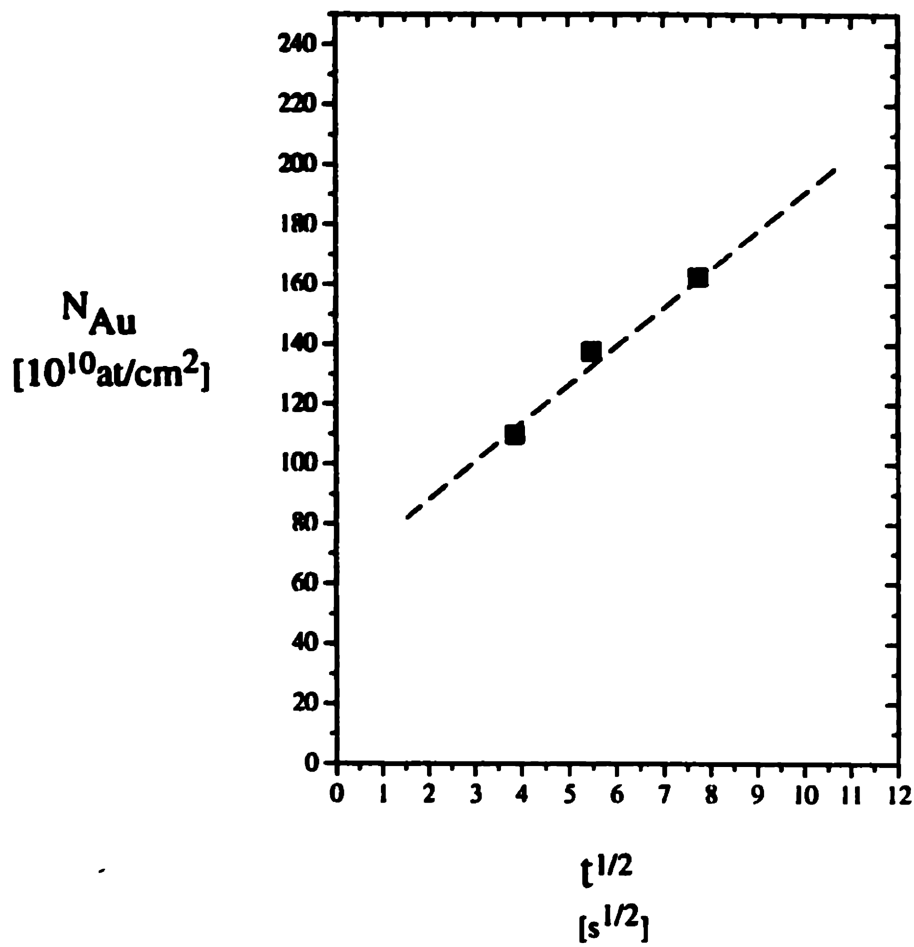

Figure 6-10: Variation of gold coverage, determined by TXRF, with immersion time.

Variable	Values
doping type	n,p
exposure time	1, 5, 30 min.
illumination	on, off
copper concentration	30, 100, 400 ppb
HF concentration	1:100, 1:10, undiluted
Air exposure	yes,no
Pt contact	open circuit, closed circuit

Table 6.2: Factors investigated in copper deposition study.

for TXRF measurement. Surface copper concentration was measured by TXRF [16] at 5 points (centerspot + 4 symmetrical locations 30 mm off-center). We also performed elaborate AFM to study the morphology of copper deposits. ICP-MS was used to verify the accuracy of copper ion concentrations in solution and to ascertain the absence of other metallic contaminants in appreciable amounts.

Results and discussion

Figure 6.11 shows the effect of copper concentration in solution on surface copper concentration for n and p type silicon immersed for 300s in 1:100 HF under cleanroom illumination. Surface copper concentrations are averages over the 5 measurement points; errorbars shown are standard deviations.

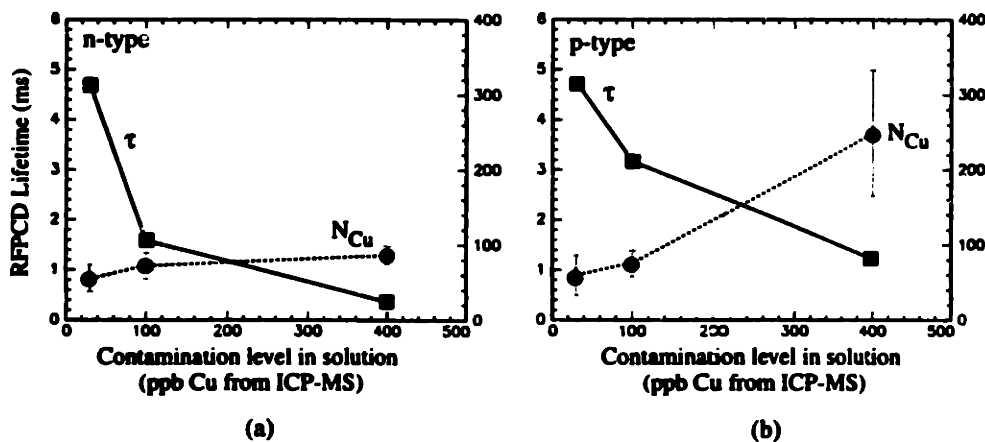

Figure 6-11: The effect of copper concentration in 1:100 HF solution on lifetime and deposition level for (a) n and (b) p-type wafers. All wafers were immersed for 5 minutes.

A salient difference between n and p-type silicon is the deposition level at high (400 ppb Cu^{++}) in solution. For p-type, N_{Cu}, the concentration of copper atoms on the silicon surface, varies roughly linearly with C_{Cu}, the concentration of copper ions in HF. Meanwhile, for n-type, N_{Cu} saturates to a value of around 10^{12} atoms/cm^2 for n-type. We believe this effect is due to the slowness of the silicon dissolution reaction

[16] The detection limit of TXRF for copper is around 0.5×10^{10} atoms/cm^2.

on n-type material (Equation 6.2). Because the equilibrium concentration of holes is extremely low on n-type material (even when the bands are bent into depletion), copper deposition may become rate limited by reaction (6.2) because of the need to maintain charge balance between anodic (silicon dissolution) and cathodic (copper deposition) reactions.

Comparison of deposition rate with earlier work

The apparent linearity between C_{Cu} and N_{Cu} for p-type material suggests the possibility that, in absence of a rate limiting step resulting from silicon dissolution, the deposition process might be diffusion-limited, as suggested elsewhere based on experiments at higher copper concentrations in solution [43, 44]. We can calculate the diffusion-limited value based on the Cottrell relationship, which expresses the diffusion limit for a planar Fickian diffusion problem [17]:

$$N_{Cu}(t) = 2 \cdot D^{1/2} C \pi^{-1/2} t^{1/2} \tag{6.8}$$

where D is the diffusivity of the ion in solution, t is the exposure time, and C is the concentration (cm^{-3}) of ions in solution. For 400 ppb copper in solution ($C = 3.8 \times 10^{15}$ cm^{-3}) we calculate $N_{Cu} = 2 \times 10^{14}$ cm^2 after 300s immersion, using $D_{Cu^{++}} = 7.8 \times 10^{6}$ [43]. This value for N_{Cu} is a factor 80 larger than our measured value on p-type material (Figure 6.11). These results indicate that at low (ppb) levels of copper in solution, the deposition reaction occurs much more slowly than the limiting value imposed by the diffusion limit. This observation tells us that reduction rate of copper ions at low ppb levels in solution is very slow compared to the rate observed in earlier experiments using much higher (ppm) levels of copper in solution [126, 43, 44].

The high reaction rates reported in the literature suggest a different reaction mechanism at high copper concentrations in solution. At the low copper concentrations used in our experiments (ppb levels) copper reduction is bound to be dominated by

[17] We can apply the relationship for a one dimensional diffusion problem even when copper deposition occurs on a 2D array of point sinks, as long as the diffusion length, $\sqrt{Dt}$, is considerably larger than the average distance between the point sinks.

precipitate nucleation at the silicon/solution interface, rather than growth of existing precipitates. At higher copper levels, nucleation is fast [43, 44]. As discussed in Section 6.3.3, growth of the nuclei by ion reduction at the Cu/solution interface is expected to rapid also, because copper ions can capture electrons from a continuum of states in the copper metal, much like gold ions when depositing on silicon. Copper ion diffusion to the Cu/solution interface or, for high copper concentrations in solution, the anodic reaction are likely to be the only factors limiting the deposition rate.

6.4.7 Effect of doping type on precipitate size

Effect of doping type on surface lifetime

Because RFPCD measures surface defects, we expect an inverse relationship between surface lifetime and the areal density of copper precipitates. Since levels deposited on n-type material from the 400 ppb solution give rise to a much greater degradation of τ than the higher copper levels deposited on p-type from the same solution (Figure 6.11), we expect a finer distribution of copper precipitates on the n-type wafer. This difference between n and p-type is consistent with our expectation, that nucleation should be faster on n-type, because of the higher driving force (greater filling of surface states); hence a denser precipitate distribution should result than on p-type. On p-type, growth is expected to be more rapid than on n-type, because the anodic reaction (silicon dissolution rate) proceeds faster as a result of the higher concentration of holes at the surface.

AFM analysis of precipitate density

To verify our hypothesis, we have performed extensive AFM analyses on the n and p-type wafers exposed for 5 min. to the 400 ppb copper solutions. The 400 ppb wafers were selected because, for these wafers, the difference in lifetime response between n and p-type was the most pronounced. Pictures were randomly selected from the center area of the wafer, previously analyzed by TXRF. Picture sizes varied between

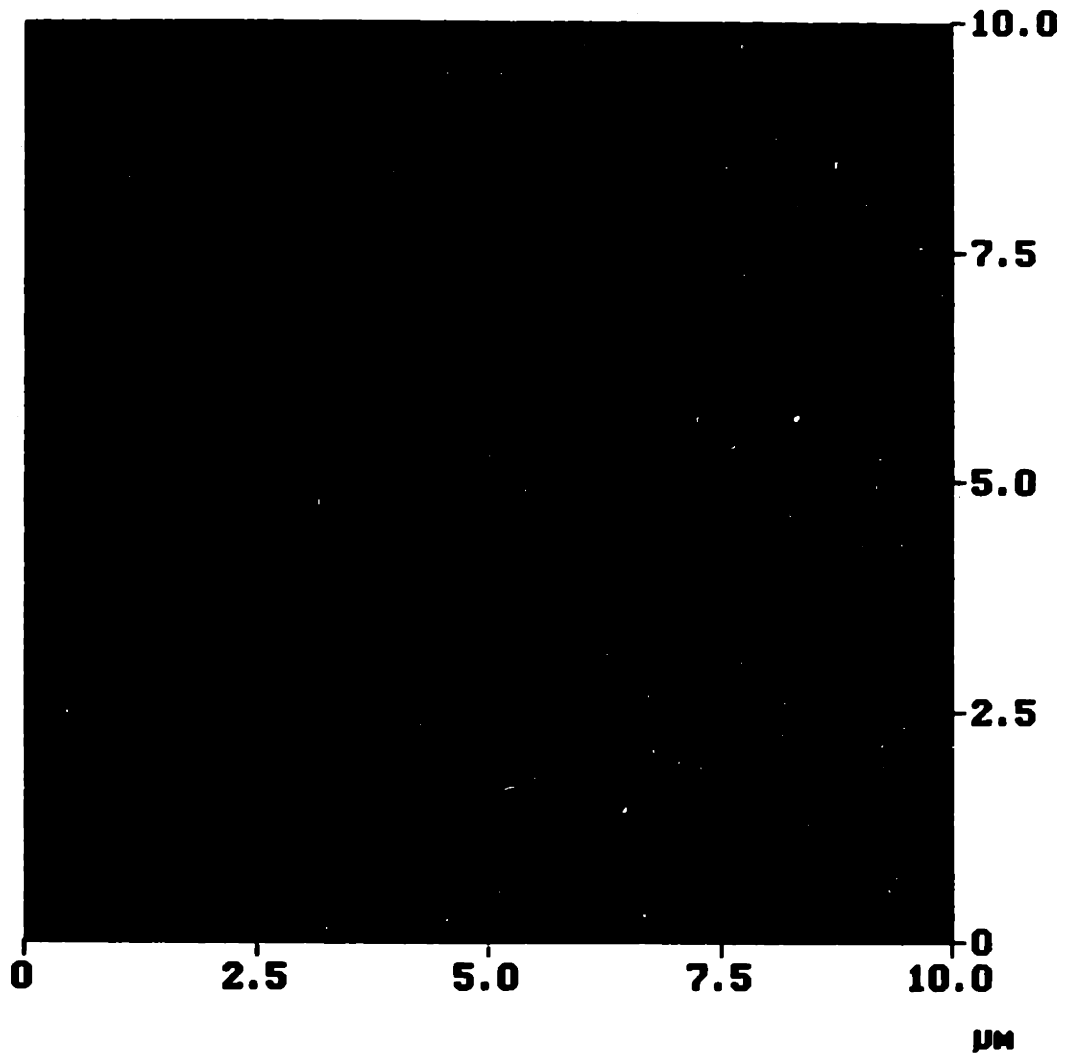

Figure 6-12: AFM image of a n-type wafer immersed for 5 minutes in 1:100 HF containing 400 ppb Cu^{++}.

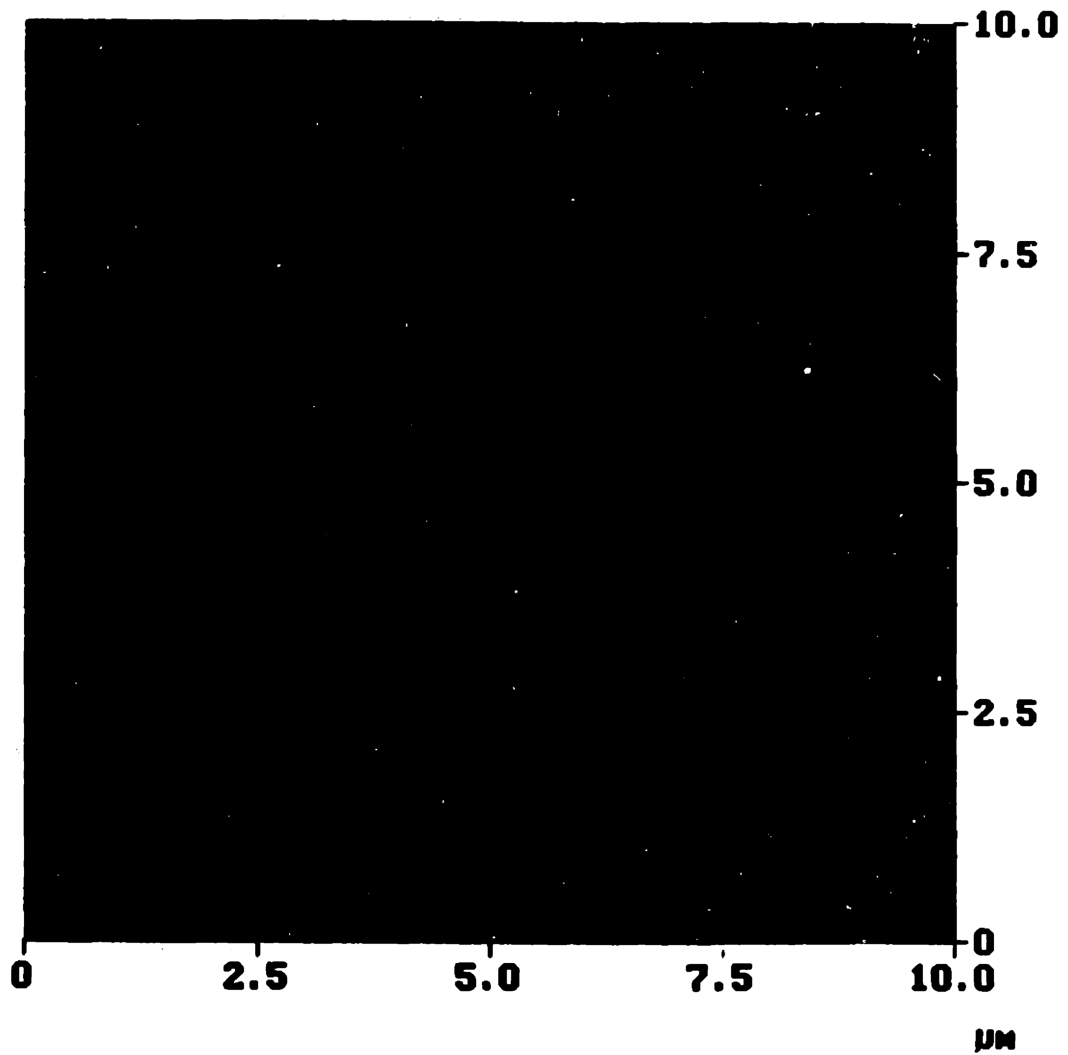

Figure 6-13: AFM image of a p-type wafer immersed for 5 minutes in 1:100 HF containing 400 ppb Cu.

1x1 and 5x5 μm. Figures 6.12 and 6.13 show typical AFM images for the two wafers. A coarser precipitate distribution is observed for the p-type sample. Since the surface lifetime is inversely related to the density of surface defects, we expect a coarser distribution to have a lesser effect on the surface lifetime than a fine distribution of smaller precipitates.

We used the grain size algorithm on the AFM instrument to determine the grain size distribution for both samples. Surface roughness on the prime wafer material we used was so low (typically 2 Åor less) that precipitates as small as 1 nm could reliably be discerned from peaks in the roughness distribution. Precipitate size distributions corresponding to the images shown in Figures 6.12 and 6.13 are shown in Figures 6.14. Our conjecture that precipitates on the p-type wafer have a coarser distribution than on the n-type wafer, is confirmed.

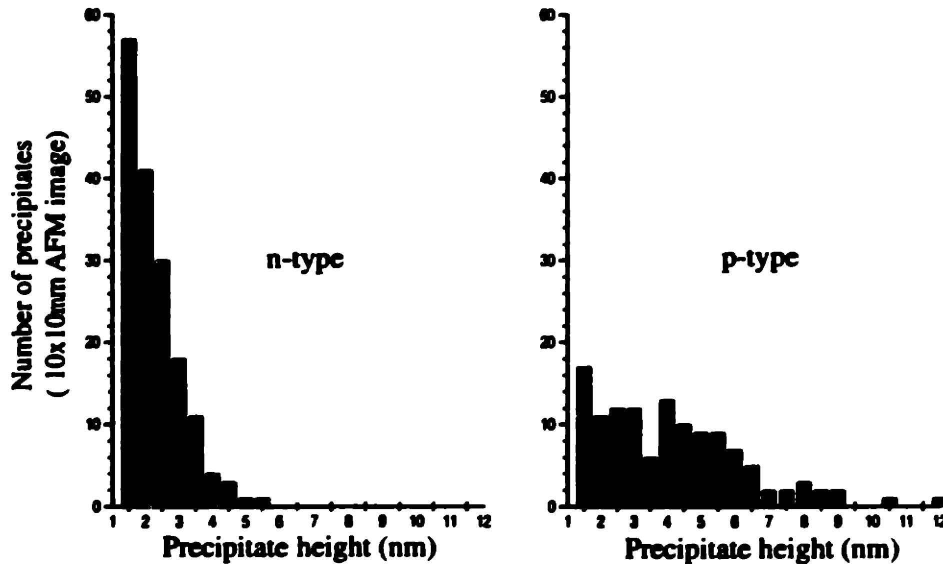

Figure 6-14: Precipitate size distribution of the wafers immersed for 5 minutes in 1:100 HF containing 400 ppb Cu^{++}.

To estimate the areal precipitate density, it is necessary to calculate the average precipitate volume for both size distributions. Based on the overall distribution from multiple images obtained from the same wafer, we calculated the average volume

from the precipitate height distribution height by assuming the precipitates to have a hemispherical shape[18]. The average precipitate size is obtained as:

$$V_{av} = \frac{\sum_i^n 2\pi r^3}{n} \tag{6.9}$$

Where n is the total number of precipitates in the population (the number of copper atoms per nm^3 equals 85). The areal density of precipitates, N_{ppt}, can then be calculated as:

$$N_{ppt} = \frac{N_{Cu}}{85 \cdot V_{av}} \tag{6.10}$$

where V_{av} is expressed in nm^3.

The results of the volume integrations is shown in Tabel 6.3.

	n-type	p-type
τ_{meas} (μs)	379	1231
Cu (cm^{-2})	(86.8±11.6)x10^{10}	(248±84.0)x10^{10}
V_{av}	2.23x10^3	24.2x10^3

Table 6.3: Results of AFM analysis of precipitate density on p and n-type wafers immersed for 5 min. in 1:100 HF solution containing 400 ppb Cu^{++}.

The average precipitate size is about 10 times larger on the p-type wafer than on the n-type. Based on the amount of copper measured by TXRF, we can estimate the areal density of precipitates, N_{ppt}, to be roughly three times smaller on the p

[18]As discussed in Section 3.3, the large lateral dimensions of the precipitates on the AFM pictures are an artefact of the AFM technique, being determined by the tip shape rather than by the true lateral dimensions of the precipitate. For lack of information about the true aspect ratio, we have assumed hemispherical precipitates.

than on the n type wafer. The minority carrier capture cross section per cluster is approximately $2x10^{-14}cm^2$.

Discussion

The analyses performed on the wafers exposed to 400 ppb Cu^{++} have given us important insights on the deposition mechanism and as well as the interpretation of the RFPCD measurement:

- the doping type has a drastic impact on the morphology of the copper deposits; on the p-type we analyzed, fewer precipitates are formed, but because they are, on average, 10 times larger in size, the total amount of copper deposited is greater for p-type;
- the RFPCD results are consistent with the AFM data on the areal density of copper precipitates;
- comparison of the deposition rate to the diffusion limited reaction rate leads us to the conclusion that kinetics of copper reduction at the silicon/solution interface is slow. Even on p-type silicon, where the anodic reaction is not expected to be rate limiting, copper deposits at roughly 1/80 of the diffusion limited reaction rate.

Conclusion

Our AFM observations have shown, for the first time, a difference in the deposition mechanism between n and p-type. This difference is expected based on the difference in driving force (thermodynamics) and filling of surface states (kinetics). *Nucleation* occurs more easily on n-type because the areal density of filled surface states is higher (driving force is larger); on p-type, the nucleation is slower (driving force is smaller), but growth is more rapid, because the kinetics of the anodic reaction is faster. On p-type material one therefore observes fewer, but larger sized, precipitates. This difference in deposit morphology was shown to be reflected in the RFPCD measurement.

For larger precipitate sizes, the sensitivity of the RFPCD technique to the surface copper level is degraded as the lifetime scales inversely with the *density* of precipitates, not with their size (volume).

6.4.8 Effect of HF concentration on copper deposition rate

Experimental

We varied the HF content of the spiked HF solutions from a dilution ratio 1:100, to undiluted 48% HF. Both n and p type wafers were exposed for 5 minutes to HF solutions containing 30 ppb Cu^{++}.

Results and discussion

The results of these experiments are shown in Figure 6.15. A marked decrease in the deposition rate with increasing HF concentration is observed. Effects of HF concentration on metal deposition rate were reported earlier by Nagahara *et al.* [135]. Increasing the HF concentration has a number of effects which can be expected to influence the rate of metal deposition.

One might argue that increases in HF concentration will increase complexation of the metal ion by fluoride, resulting in a slower deposition rate because, once complexed, the metal ion is not available for physisorption. In 1:100 dilute HF, the fraction of complexed copper is negligible, because almost all of the HF molecules are undissociated and the fluoride concentration, $[F^-]$, is small [6]. As the concentration of HF is increased, its degree of dissociation is decreased further but the total fluoride concentration rises nevertheless, so that more copper is complexed to form CuF^+ and CuF_3^- [127]. However, Schouterden [136] reports that copper deposition occurs more rapidly from buffered HF than from dilute HF, even though a larger fraction of the copper ions is complexed in buffered HF. Therefore, it seems likely that the effect of HF concentration is due to pH differences, *not* differences in complexation. As the HF concentration increases, the pH decreases; hence, the silicon bands will be lowered as the H^+/H_2 redox level in solution decreases. The lowering of the bands with respect

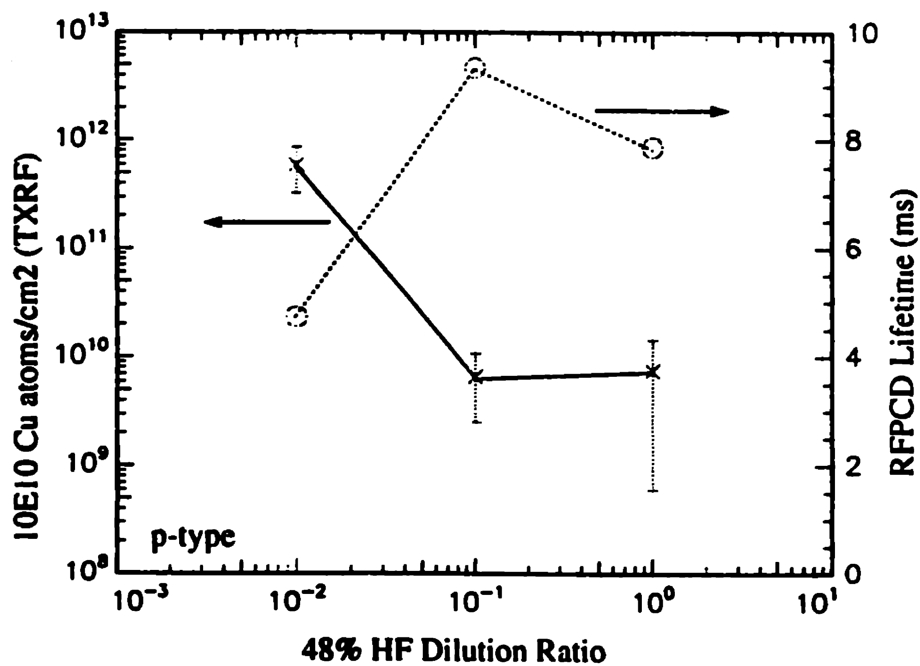

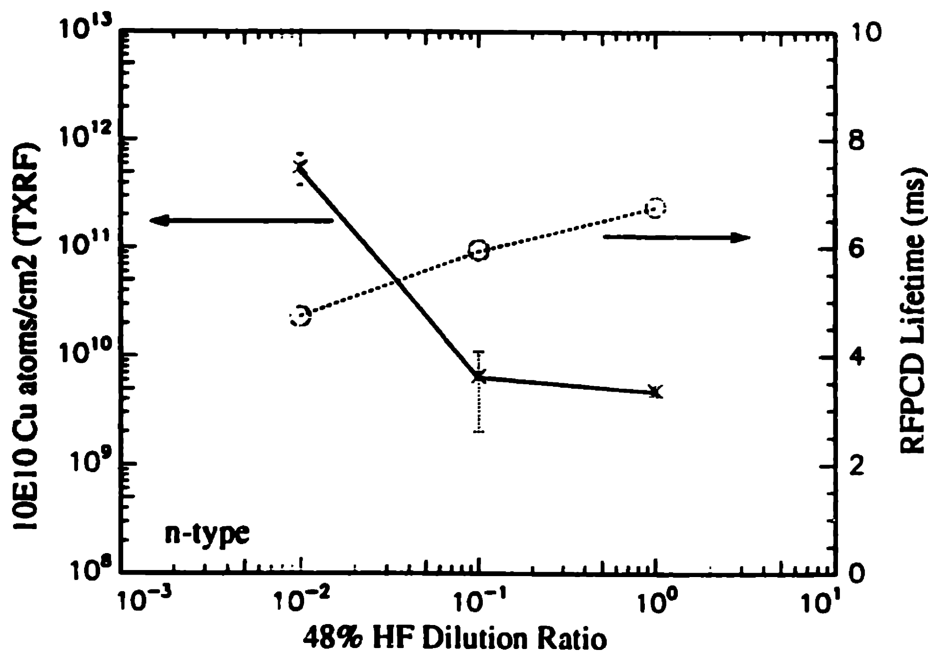

Figure 6-15: The effect of HF concentration on copper deposition level and lifetime. The wafers were immersed for 5 minutes in solutions containing 30 ppb Cu^{++}. Lifetimes were measured in 48 % HF immediately after the contamination treatment.

to the copper levels in solution reduces the deposition tendency.

Capture cross section at low ($< 10^{10}$ cm^{-2}) coverage

The 1:10 and 48 % HF exposed wafers offer a good opportunity to relate the surface lifetime measured by RFPCD to copper level, determined by TXRF, in the very low coverage range ($< 10^{10}$ cm^{-2}). We calculated minority carrier capture cross sections on n and p type material using the familiar expression (Equation 4.21). The results are summarized in Table 6.4. We obtain a cross section of approximately 8.5x1010^{-17} cm^2 for hole capture on n-type, and 5.6x1010^{-17} cm^2 for electron capture on p-type. The larger cross section per copper atom on n-type is consistent with the smaller cluster size (higher nucleation rate and smaller growth rate), expected for n-type material.

type	treatment	τ_{meas} (μs)	Cu (10^{10}at/cm^2)	σ^{Cu} ($10^{-17}cm^2$)
n	5 min. 1:10 HF, 30 ppb Cu^{++}	5956	0.65	8.07
n	5 min. 48 % HF, 30 ppb Cu^{++}	6758	0.48	9.63
p	5 min. 1:10 HF, 30 ppb Cu^{++}	9334	0.66	5.48
p	5 min. 48 % HF, 30 ppb Cu^{++}	7871	0.75	5.71

Table 6.4: Cross section for minority carrier capture per copper atom on the silicon surface, for $< 10^{10}cm^{-2}$ copper coverage.

6.4.9 Impact of ambient exposure on copper-induced surface lifetime degradation

Experimental

The results presented so far always involved experiments where the lifetime measurement in 48 % HF was performed immediately following the copper deposition treatment. We performed a set of experiments similar to the ones described earlier, where the wafers were left exposed to the cleanroom atmosphere for several hours before measuring the surface lifetime in concentrated HF. Wafers were first cleaned using the standard MIT clean and then exposed to 1:100 HF solutions containing a controlled amount of metal ions, prepared in the usual fashion. After removal from the contaminated solution, the wafers were left exposed to the cleanroom for several hours (no rinsing was performed). For measurement, the wafers were immersed in 48 % HF until the lifetime stabilized (typically a few minutes).

Results

The results of these experiments are shown in Figure 6.16. Figure 6.16a shows the variation of surface lifetime with copper concentration in solution and immersion time for n-type wafers. Figure 6.16b shows the same information for exposure of both n and p-type material to 50 ppb in solution.

The difference between these surface lifetime results and earlier measurements, without the intermediate ambient air exposure, is remarkable. Comparison of Figure 6.16 to Figure 6.11 reveals a drastic reduction in the surface lifetime resulting from the ambient exposure. On n-type material, the lifetime value obtained for 10 ppb, 1 min immersion *with prolonged air exposure prior to RFPCD measurement* is roughly a factor of 30 *smaller* than the lifetime measured immediately after the exposure step. This pronounced increase in the effect of copper on the surface lifetime represents a similar increase in sensitivity of the RFPCD technique for surface copper detection.

By performing similar measurements on wafers exposed to uncontaminated HF solutions, we have verified that the reduction in lifetime is caused by the copper

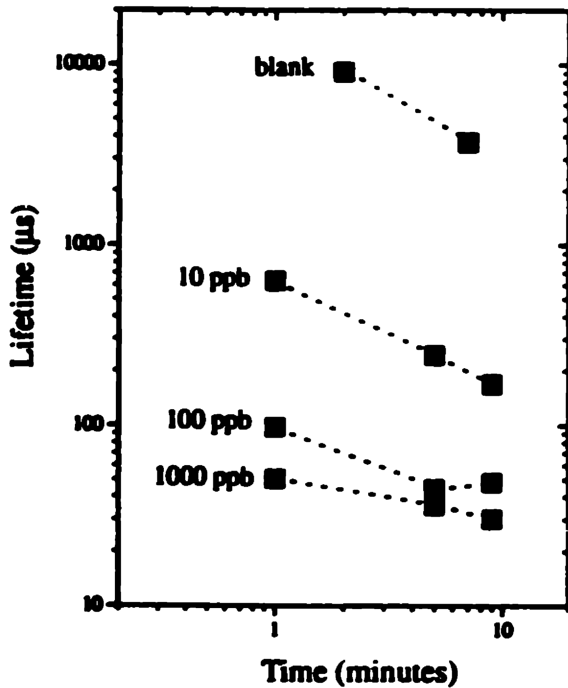

(a)

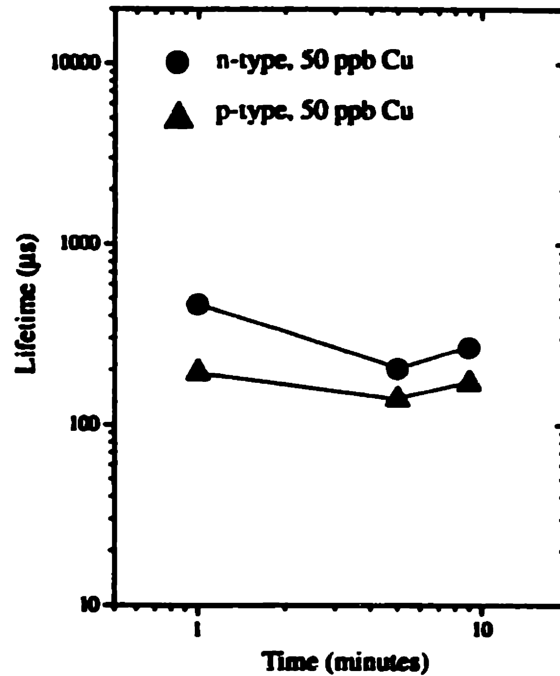

(b)

Figure 6-16: (a) Variation of surface lifetime with spiking level and immersion time. The wafers were exposed to air for several hours before being measured in 48 % HF. (b) Variation of surface lifetime with immersion time for n and p-type wafers. The wafers were exposed to 1:100 HF solutions containing 50 ppb Cu^{++}, followed by air exposure for 24 hours before being measured in 48 % HF.

contamination, and *not by native oxide growth during air exposure.* Exposure to 1:100 HF contaminated with Fe or V, followed by air exposure and 48 % HF measurement, leaves the surface lifetime unaffected. This proves that any native oxide, grown during air exposure, is rapidly removed in 48 % HF and hence does not affect the surface lifetime measurement.

Discussion

The observations presented in this section suggests that some of the copper present on the wafer after exposure to the contaminated solution is inactive in surface recombination during measurement in 48 % HF; subsequent air exposure brings the copper in an "activated" state where its effect on surface recombination is greatly enhanced. Since copper reduction is slow, physisorbed copper *ions* will be present on the wafer surface after removal from the contaminated solution. If the RFPCD measurement is done immediately following the immersion, these ions will not affect the surface lifetime since their bonding to the hydrogen passivated silicon surface is only very loose; hence, they do not affect the electronic structure of the surface. Upon ambient air exposure, native oxide growth introduces surface states with energy levels in the silicon bandgap (see Chapter 5). As pointed out earlier in this chapter, surface states are essential for the copper reduction reaction to take place, because the position of the Cu^{+}/Cu^{++} level in the silicon bandgap precludes direct electron capture from one of the bands (Figure 6.1). Hence we propose that air exposure, following copper contamination, leads to the reduction of physisorbed copper ions to the metallic state. Once fully reduced (oxidation state 0), the copper forms divalent bonds with the surface silicon, creating surface states in the silicon bandgap as discussed in Chapter 5. This mechanism is supported by the observation that surface copper increases the native oxide growth rate of HF-dipped silicon [137].

TXRF analysis of a wafer exposed to the the same treatment as the 10 ppb Cu^{++}, 1 min exposed wafer in Figure 6.16a revealed a copper level of 0.68×10^{10} cm^{-2}. Based on this value and the surface lifetime measured in 48 % HF (629 μs), we obtain a cross section per copper atom of approximately 10^{-15} cm^2. As can be seen in Figure

6.16b, ambient exposure results in a slightly stronger lifetime degradation for p- than for n-type wafers. The time dependence of the lifetime results in the low copper ion concentration range (10 ppb) is consistent with a diffusion limited physisorption process ($\tau_s \approx t^{-1/2}$).

Relevance

The results presented in this section emphasize the important role of air exposure for maximizing the effect of low levels of copper on the surface lifetime. Our data indicate that ambient exposure allows easy detection of copper contaminants at ppb and even ppt levels in HF solution. Based on the surface lifetime data shown Figure 6.16a, we predict a copper ion concentration of $\approx$ 440 ppt in the blank solution. This level of copper in the blank solution is consistent with the specified purity of 1 ppb for Gigabit^{TM} chemicals.

Using $\sigma = 10^{-15}$ cm^2, a lower detection limit of 10^8 cm^{-2} is obtained for copper detection in 48 % HF, after air exposure. this is 40 times lower than the lowest detection limits attainable for copper detection with TXRF. We can use the value for the cross section to calculate that the copper level on the wafer exposed to the blank solution for 2 min. (bulk lifetime 9.08 ms) is approximately 1.2x10^{8}cm^{-2}, or about 10 ppm of a monolayer coverage. This value is well below the detection limit of today's most advanced surface analysis tools. The demonstrated sensitivity of RFPCD for impurity detection in bulk liquids is matched only by ICP-MS. Meanwhile, its speed, cost, and easy of use make the RFPCD technique highly preferable for in-line application in a semiconductor fab.

6.4.10 Effect of illumination on copper deposition rate

Experimental

Wafers were cleaned and exposed to the contaminated solution according to the usual experimental procedure. For dark deposition experiments, the bath containing the contaminated solution was placed in an empty overflow bath and a plastic lid was

used to cover the overflow bath and screen cleanroom light. Fluorescent lights of the wetbench provided "normal" cleanroom lighting conditions for the experiments under illumination. The estimated light intensity under illumination , based on the measurement of the photocurrent of a high efficiency solar cell, is 10^{14} cm^{-2}. The corresponding injection level, based on an effective lifetime of 1 ms and a wafer thickness of 625 μm, is approximately 10^{13} cm^{-3}. Two different treatments were used to investigate the effect of the light: (1) immersion for 1 minute in 100 ppb 1:100 HF solution and (2) 5 minute immersion in 30 ppb 1:100 HF solution. The results of these experiments are shown in Figure 6.17.

Another set of experiments to study the effect of illumination involved both n and p-type wafers, exposed for 2 min. to a 1:100 HF solution containing 200 ppb copper ions. We used AFM to count the number and calculate the average size of the copper precipitates. All calculations were performed on a single 5x5 μ AFM image per wafer. The results of these experiments are shown in Figures 6.18.

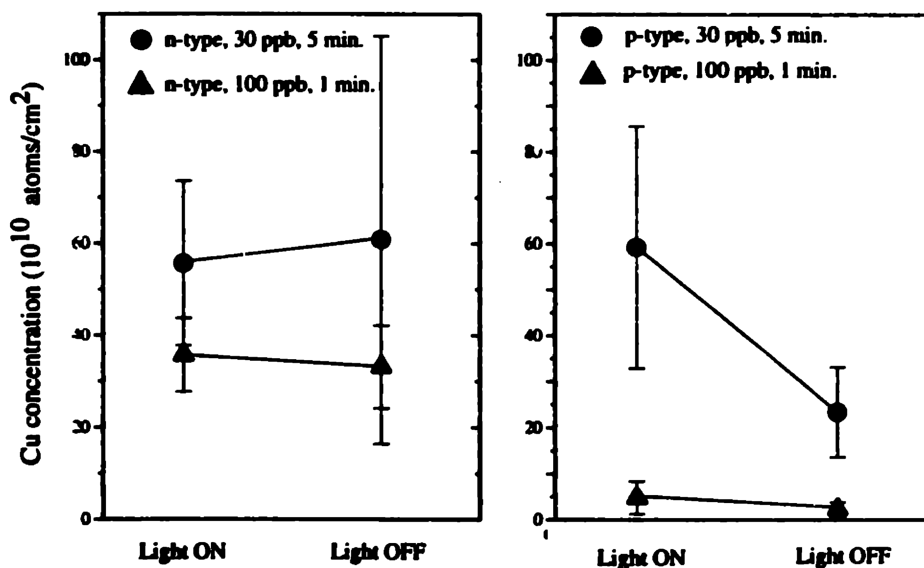

Figure 6-17: The effect of illumination on copper deposition on silicon from 1:100 HF solution.

Results and discussion

Figure 6.17 shows that low-intensity light increases the deposition rate, especially on p-type material. The increase in deposition rate on n-type is less pronounced. Figure 6.18 confirms that this increase is both due to an increase in the nucleation rate (number of precipitates) and an increase in precipitate size.

We have calculated the effect of illumination and doping type on the driving force for reduction of 200 ppb Cu^{++} ions from 1:100 HF solution. An injection level of $10^{13}cm^{-3}$ was assumed. The results of our calculations are summarized in Table 6.5. The negative values for the Gibbs free energy, ΔG, of the cathodic reaction indicate that reduction of ions from solution is thermodynamically favorable in all of the cases considered. The driving force is larger for deposition on n- than on p-type. Illumination increases the driving force for deposition, especially for p-type material.

Light	$\Delta G(n)$	$\Delta G(p)$
Off	-227	-87
On	-327	-267

Table 6.5: The effect of doping type and illumination on the driving force (Δ G, in meV) for the $1/2\ Cu^{++} + e^- \longrightarrow 1/2\ Cu^o$ reaction. A doping level of $10^{15}cm^{-3}$, a light injection level of $10^{13}cm^{-3}$ and 200 ppb Cu^{++} in solution were assumed. The calculation is further based on the measured values for the bandbending on n- and p-type material in the in the dark.

The number of precipitates nucleated is in good agreement with the driving forces calculated based on the thermodynamic model (Table 6.1); the drastic increase in the deposition tendency for p-type agrees with the strong increase in driving force ΔG (from -87 meV to -267 meV per electron). The higher density of precipitates on n-type agrees with the higher driving force calculated.

Under low level illumination, the surface hole concentration increases drastically

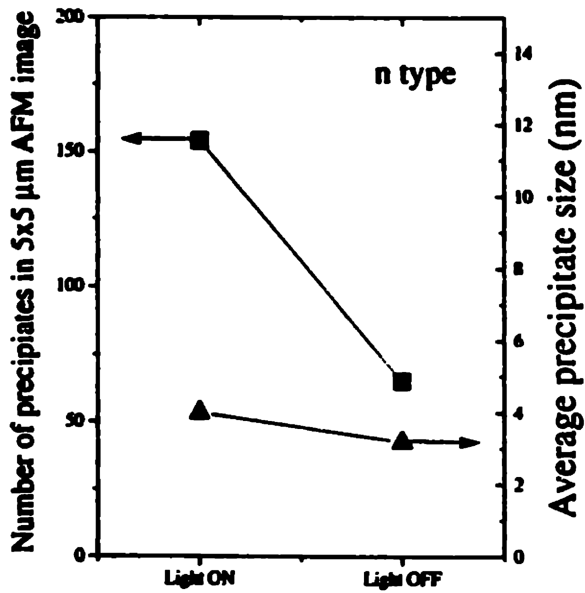

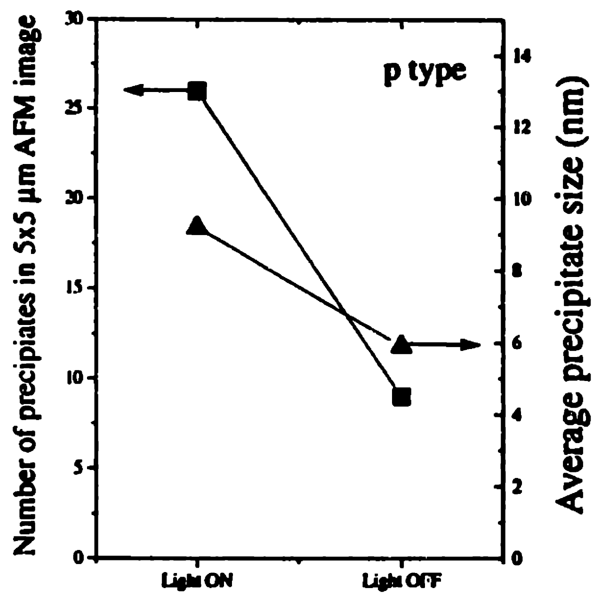

Figure 6-18: The effect of illumination on precipitate size and density for n and p-type wafers immersed for 2 min. in 1:100 HF containing 200 ppb Cu^{++}. Density and average precipitate size were obtained from 5x5 μm AFM images.

compared to the dark. As was mentioned before, the anodic reaction (silicon dissolution) is controlled by the flux of holes to the Si/solution interface. Because of the high concentration of copper in solution for the experimental data shown in Figure 6.18, the deposition rate is likely limited by the anodic reaction, not by the rate of copper ion diffusing towards the Cu/liquid interface. This explains the larger precipitate size on p-type compared to n-type and in the light compared to in the dark.

Based on the Nernst relationship (6.3), the low driving force for p-type in the dark (-87 meV) implies that copper deposition will stop completely ($\Delta G=0$) for 220 ppt Cu^{++} in solution (parts per trillion = ng/l). The absence of any deposition tendency for copper concentrations below this level is due to our implicit assumption that copper forms as a pure phase (unit activity), hence its entropy is not dependent on the surface concentration of copper. The effect of doping level and illumination on the copper level where the driving force vanishes is shown in Table 6.6. Only for p-type silicon in the dark could deposition be suppressed using today's highest purity chemicals (< 10 ppt Cu).

Light	ΔG(n-type)	ΔG(p-type)
Off	$4 \cdot 10^{-6}$	$2 \cdot 10^{-1}$
On	$2 \cdot 10^{-9}$	$2 \cdot 10^{-7}$

Table 6.6: The effect of doping type and illumination on the copper concentration (in ppb) where the driving force, ΔG, vanishes. This calculation was based on the driving force values listed in Table 6.5.

Significance

Good qualitative agreement between the model predictions and the calculated driving force strengthens the support for the deposition model developed in Section 6.3. Our

model postulates that surface electron concentration determines nucleation kinetics, while surface hole concentration determines growth rate. Apart from light, application of a bias potential across the silicon-liquid junction is an obvious way to influence the surface carrier concentrations. A possible approach to active control of the metal deposition rate by appropriately biasing the sample with respect to the solution, is presented in the next section.

6.4.11 Effect of bias potential on copper deposition rate

Experimental

Pieces of n and p type wafers (type I and III, four pieces of each type) were cleaned using the MIT standard clean. The wafers were immersed for 2 minutes in a 1:100 HF solution containing 200 ppb Cu^{++}. The deposition conditions were varied as follows: illumination (on or off); doping type (n or p); and open or closed circuit. For the closed circuit measurements, an ohmic contact was made between the wafer and a Pt mesh electrode (see Section 4.4.2). The Pt electrode, connected to the silicon, was then immersed together with the wafer in the 1:100 HF solution. For the open circuit measurements, no contact was made. After the immersion step, the eight samples were analyzed using AFM. Precipitate densities and the average precipitate size were calculated for 5x5 μm AFM images. The calculation of the average precipitate radius was performed as discussed in Section 6.4.7.

Results and discussion

The results are shown in Figure 6.19 (precipitate size) and Figure 6.20 (precipitate number). The contacting has a drastic effect on both nucleation and growth kinetics. With the contact, the number of precipitates as well as the precipitate size are significantly reduced both on n and p type when the light is on. With the light turned off, closing the circuit gives rise to a slight increase in the precipitate density, while the average precipitate size is again reduced.

To analyze this effect, we need to consider the effect of the Pt contact on the

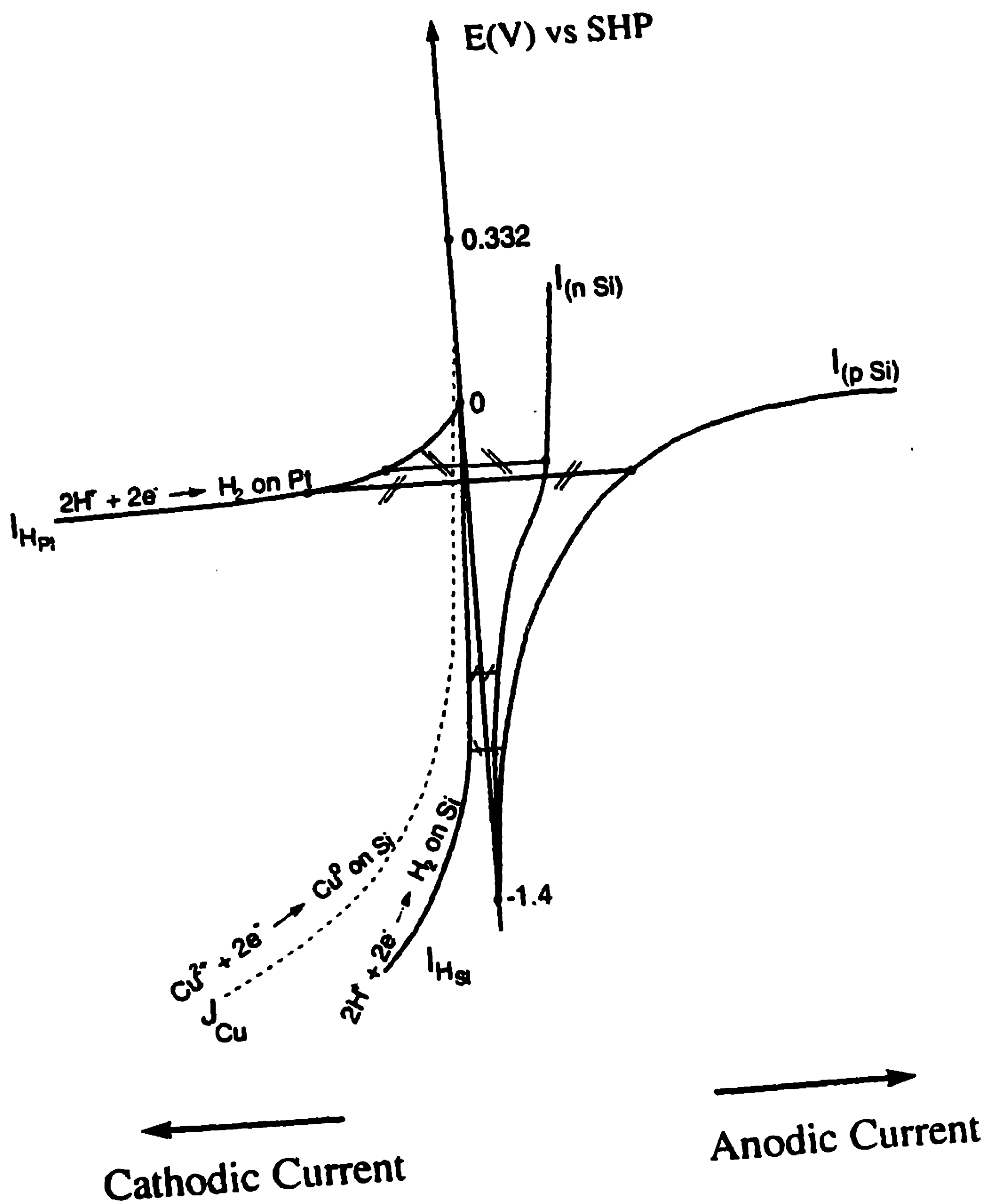

Figure 6-19: The effect of connecting the wafer to a Pt electrode on the electrode potential of n and p-type silicon.

bandbending at the silicon/liquid interface. As we discussed in Section 6.3, the bandbending potential affects the driving force for deposition, through its effect on the concentration of electrons at the surface and the filling of surface states which mediate the copper reduction reaction.

In contrast to open circuit conditions, the net current across the wafer/solution interface does no longer have to equal zero when the Pt contact is immersed in the 1:100 HF solution. Instead, charge balance requires the electrode currents at the Pt electrode and the silicon wafer to compensate each other. The silicon-Pt electrode system will acquire a so-called "mixed potential" (corrosion potential) at which the sum total of the electrode reaction currents equals zero [138].

Immersed in a acidic solution, the Pt electrode provides an active surface for the hydrogen reduction reaction :

$$2H^+ + 2e^- \longrightarrow H_2 \tag{6.11}$$

Due to the low overpotential (large exchange current density) of the hydrogen evolution reaction on Pt, the fermi energy inside the Pt electrode will effectively be 'pinned' at the energy corresponding to the reversible potential of the H^+/H_2 couple [138]. For small electrode currents, the fermi energy will remain flat across the metal-semiconductor interface, and hence the fermi level in the semiconductor will also be pinned at the reversible potential of the H^+/H_2 couple. Referring to Figure 6.1, this means that the silicon bands will be lifted up with respect to the energy levels of ions in solution, reducing the thermodynamic driving force for deposition, ΔG. The effect of the Pt contact on the potential of the silicon can also be understood using an Evans diagram construction (Figure 6.21) [138]. Due to the lower overpotential for silicon dissolution on p-type material (higher anodic reaction rate), the corrosion potential of the p-type Si-Pt couple will be slightly lower than for the n-type silicon-Pt couple. Illumination will reduce the overpotential for silicon dissolution on both n and p-type material, and hence will pull down the corrosion potential of both couples.

Returning to Figure 6.1, changes in the corrosion potential towards more positive

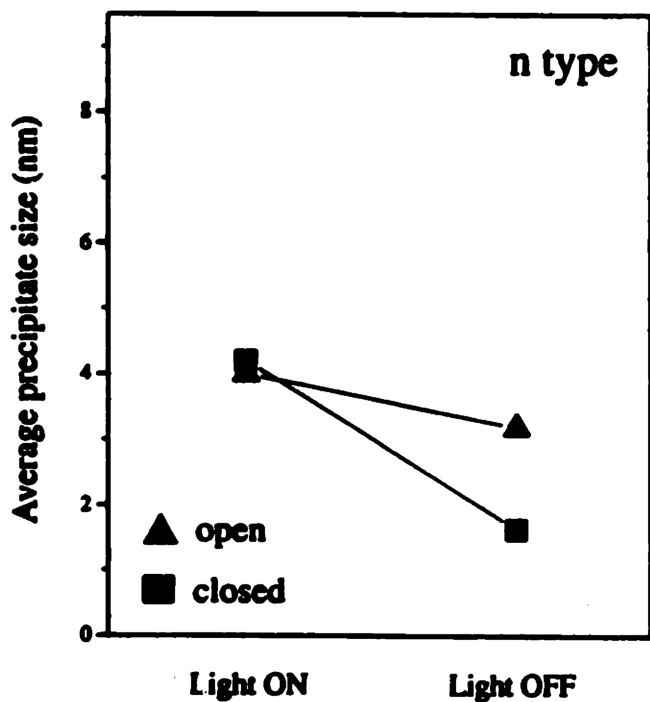

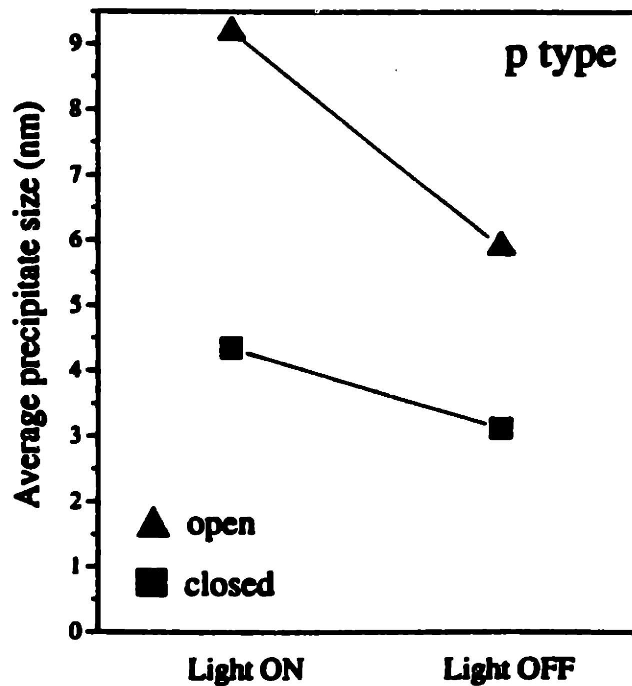

Figure 6-20: The effect of contacting the wafer to an immersed Pt electrode on the precipitate size for n and p-type wafers immersed for 2 min. in 1:100 HF containing 200 ppb Cu^{++}. The average precipitate sizes were obtained from 5x5 μm AFM images.

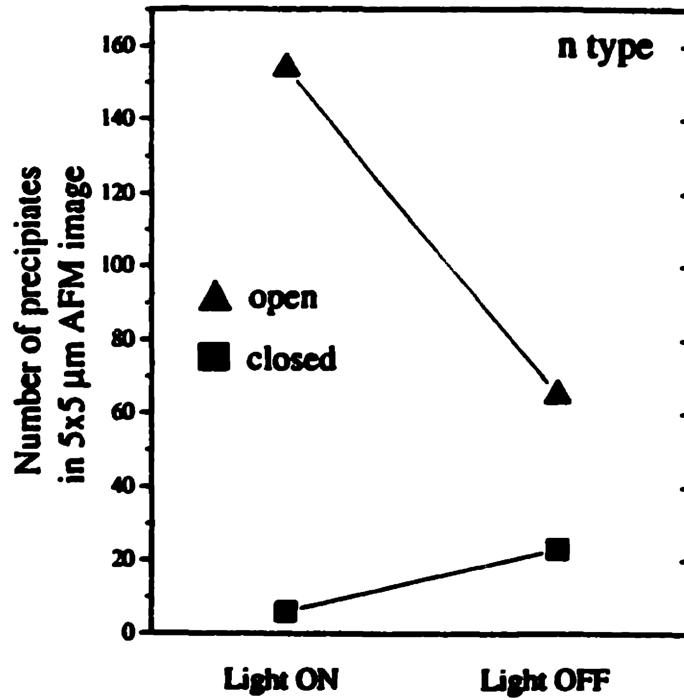

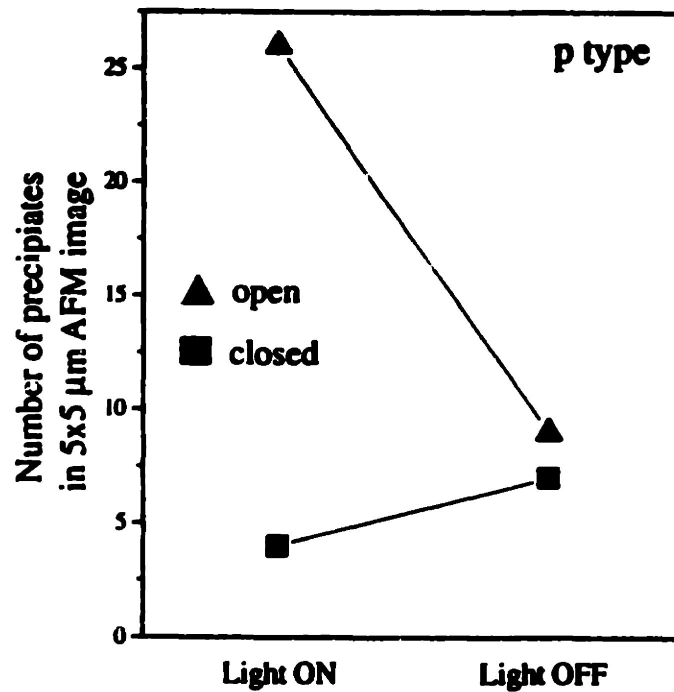

Figure 6-21: The effect of contacting the wafer to an immersed Pt electrode on the number of precipitates for n and p-type wafers immersed for 2 min. in 1:100 HF containing 200 ppb Cu^{++}. The numbers of precipitates were obtained from 5x5 μm AFM images.

values will reduce the driving force for deposition. This effect explains the pronounced reduction in nucleation rate as the contact with the immersed Pt electrode is made. The slight increase in the number of precipitates upon contacting for dark conditions cannot be explained using the above model.

Significance

The strong reduction in the nucleation rate, brought about by the upward shift in electrode potential of the silicon, confirms the correctness of the band model for metal reduction at the silicon/solution interface (Section 6.3). Because the results shown in Figure 6.19 and 6.20 are based on a single AFM picture for each of the deposition conditions, they should be regarded as semiquantitative at best. Further work is needed to establish the exact quantitative relationship between ΔG and the nucleation rate. As we mentioned earlier, the growth rate will be controlled by the concentration of holes at the surface. Experimental verification of a quantitative deposition model requires the use of a potentiostat for control of ϕ_s, and an accurate knowledge of the light injection level, to allow a precise control over ΔG.

The use of electrochemical techniques for enhanced control over the surface chemistry of silicon in HF wafer cleaning solutions was proposed earlier [139, 140, 141]. The use of such techniques to drain electrons from the silicon into an external system, thereby decreasing their tendency to reduce metal ions from solution, is a method for preventing metallic contamination with great intuitive appeal. Our experiment has convincingly demonstrated the efficacy of this approach. While the merits of electrochemical techniques are certainly underrecognized in the wafer cleaning community, we believe the potential benefits, in terms of relaxed purity needs for cleaning chemicals, are significant and these novel cleaning strategies are worth exploring. The feasibility of making an ohmic contact to the wafer during cleaning is but one of the issues that will have to be addressed.

6.4.12 The effect of trace copper levels on dielectric strength of ultrathin thermal oxides

Previous work

The effect of low levels of iron contamination on the breakdown strength of thin oxides was investigated by Henley *et al.* using E_{bd} testing in combination with SPV (surface photovoltage) [18]. Henley showed that conducting iron silicide precipitates form in the surface region of the wafer during cooldown after thermal oxidation. When present at the Si/SiO_2 interface, these conducting precipitates intensify the electric field and act as preferred sites for localized electric breakdown. As was pointed out earlier, iron levels as high as 10^{13} atoms/cm^3 were shown to have little negative effect on the breakdown properties of 200 Å "thick" oxides. Meanwhile, iron levels below 10^{10} atoms/cm^3 were needed to ensure satisfactory dielectric strength of 45 Å thin oxides.

Because of the importance of copper contamination in our research, we have studied the impact of very low levels of copper contamination on the breakdown strength of MOS capacitors. Available data on the effect of copper on gate oxide integrity (GOI) of thin oxides are scarce. Aderholdt *et al.* investigated the impact of Ca, Cu and Zn on the yield of a MOS DRAM process [142]. Copper levels were varied between 10^{11}-10^{13} cm^{-2} and thick (200 Å) oxides were used. No effects on the device yield were observed for copper concentrations below 10^{12} cm^{-2}. Angle-dependent TXRF analysis of thermally oxidized wafers revealed the presence of copper on top of the thermal oxide and at the oxide/silicon interface.

We have performed dielectric breakdown testing on wafers with surface levels of copper in the 10^{9}-10^{11} cm^{-2} range. The effect of these low copper levels on the dielectric strength of 70 Å, 90 Å and 200 Å thick gate oxides was studied. Our data provide the first experimental verification, for the case of copper, of the stringent surface purity requirements projected for advanced submicron CMOS [7].

Backgrounds

Dielectric strength testing is the ultimate performance metric to assess the effectiveness of pre-gate cleaning. The phenomenology of dielectric breakdown in thin SiO_2 films has been reviewed by Falster [143]. A variety of schemes exist for electrically stressing the silicon dioxide. Three approaches are commonly used : (1) the voltage is determined where the current through the capacitor exceeds a preset threshold (E_{bd} testing); (2) a constant voltage is applied and the time is measured when the current exceeds a limiting value (TDDB, time dependent dielectric breakdown); (3) a constant (low) current is sent through the oxide until the voltage drops below a preset value (Q_{bd}, charge-to-breakdown). The first of the three approaches is more suited for the analysis of so-called low-field breakdowns, caused by gross defects, which are considered the main culprits for yield loss. Charge-to-breakdown and TDDB testing provide information about time dependent breakdown events which affect *reliability* rather than *yield* of MOSFET devices. Because we expect copper contamination to give rise to a low density of isolated "killer" defects, we performed E_{bd} tests on large (3x3 mm) capacitors.

We used Weibull plots to present the results of the dielectric testing. A Weibull plot is a plot of the function ln(-ln(1-F)) vs breakdown voltage, E_{bd}. F is the cumulative fraction of devices that failed below E_{bd}. The Weibull distribution for a population of capacitors which fail by a similar mechanism is given by [144]:

$$F = 1 - exp(-CE^b) \tag{6.12}$$

where E is the voltage stress applied to the oxide. The parameter b, the slope of the failure distribution on an Weibull plot, expresses the spread of the breakdown strenths around their average value (b=0 means that capacitors are equally likely to break down at any given voltage; b=∞ means that all capacitors break down at the same stressing voltage). C determines the intercept of the failure population on the Weibull plot, and is a measure for the areal density of the defects causing the breakdown to occur.

In electrical breakdown testing, a constant slope part of a Weibull plot is often referred to as a *mode*. Metal-related surface defects are known to introduce a low-field tail in the breakdown distribution (Mode I breakdown). This breakdown mode has been attributed to the presence of hazeforming metals such as Fe, Cu, Ni, Co, Zn, Rd and Pt. In the absence of mode I breakdown events, the distribution is dominated by high-field mode II breakdown, which has a much "tighter" electric field distribution than mode I events, *i.e.*, a larger value for the parameter b [143].

Experimental

Wafers were precleaned using the MIT standard clean and exposed for 5 minutes to dilute HF solutions containing 3 different levels of copper: <10 ppt (part per trillion), < 1 ppb and 10 ppb. The grades of HF and spiking levels used are summarized in Table 6.7. Nine wafers were prepared for each contamination level, making the total number of wafers in the experiment 27.

HF grade	Cu^{++} specified	Cu^{++} added	$N_{Cu}(cm^{-2})$
Hashimoto	< 10 ppt	none	10^9-10^{10}
Ashland Gigabit^{TM}	< 1 ppb	none	10^{10}- 10^{11}
Ashland Gigabit^{TM}	< 1 ppb	10 ppb	10^{12}

Table 6.7: Copper levels of HF solutions, and estimated copper coverage after 5 min. immersion, for solutions used in pregate clean.

Immediately after the 5 min. exposure step, the wafers were transferred for gate oxidation. Gate oxides were grown at 900°C in dry O_2 [19]. The 27 wafers were furnace

[19]Gate oxidation was performed at MIT's Integrated Circuits Facility with the help of Bernard Alamariu.

oxidized in groups of nine, every split containing 3 wafers of each contamination level. Oxidation times were 11, 20 and 60 minutes, yielding oxide thicknesses of approximately 70, 90 and 200 Å. Blanket Al alloyed with 1 % Cu was deposited by e-beam immediately after cooldown to prevent oxide degradation by ambient exposure. No post metallization anneal was performed. MOS (metal-oxide-semiconductor) capacitor structures were fabricated by conventional wet chemical lithography. E_{bd} testing was performed using an computer controlled automatic wafer prober (Keithly S-450 Semiconductor Parametric Test System). Failure voltages were determined by a binary search alogorithm which determines the voltage value for which the current across the capacitor equals 1 μA.

Results and discussion

Weibull plots of the E_{bd} test results are shown in Figure 6.22. For the 200 Åoxide, the 10 and 1 ppb splits clearly give rise to a low-field breakdown mode in the failure voltage distribution. We attribute this breakdown mode to the presence of copper precipitates in the surface region. Because of the high diffusivity and vanishingly small solubility of copper at room temperature, copper has a very high tendency to from silicide precipitates upon cooling from the oxidation temperature [22, 23, 24]. These precipitates are thought to locally reduce the oxide thickness and focus the electric field lines, given rise to low field breakdown [18].

Surprisingly, the curve for the 10 ppb split is shifted downward with respect to the < 1 ppb curve, indicating a higher density of defects for the < 1 ppb split, but with the same failure behavior (weibull slope). The absence of the low field breakdown tail for the 0.01 ppb exposure emphasizes the need for extreme metallic purity, even for relatively thick oxides.

For the 90 Åset, no clear difference is seen between the 0.01 ppb and 1 ppb failure distributions, while the 10 ppb clearly introduces Mode I failure behavior (larger slope in Weibull plot). For the 70 Åsplit, 5 minutes exposure to HF solutions containing < 1 ppb or 10 ppb of copper leads to the appearance of a Mode I breakdowns tail in the Weibull plot. As in the case of the 200 Åthick oxides. we have no explanation for

the larger Y intercept observed for the < 1 ppb split.

These results demonstrate the impact of extremely low levels of copper (10^9 cm^{-2} - 10^{10} cm^{-2}) on the GOI (gate oxide integrity) of ultrathin oxides. Exposure to the $<$ 1 ppb solution has clearly a negative effect on the breakdown results of the 70 Åthick oxides, justifying the tightening of surface purity standards as gate oxide thicknesses are decreased into the sub-100 Årange.

6.5 Conclusions

In this chapter, we have demonstrated, for the first time, the use of minority carrier lifetime measurements for *in situ* kinetic studies of metallic adsorption phenomena on hydrogen passivated silicon in wet and dry ambients. All our results were analyzed in a coherent theoretical framework for the thermodynamics and kinetics of metal deposition processes.

The first step in the metal deposition reaction is the physisorption of the metal ion onto the hydrogen terminated surface, Si-H. The second step, reduction of the ion by charge transfer from the semiconductor, is only thermodynamically possible for metals with a sufficiently positive reduction potential, such as Cu and the noble metals. For Fe and electropositive metals such as V, the energy levels of ions in solution are above the fermi energy in the semiconductor, and the reduction reaction will not occur.

For reducible ions, the kinetics of the charge transfer reaction at the silicon/solution interface is strongly dependent on the position of the ion with respect to the silicon bands. Gold ions, which have energy levels below the silicon valence band edge, undergo reduction by hole injection in the silicon valence band. Because of the high density of states available inside the semiconductor, this reduction reaction occurs fast and is rate limited by ion diffusion in the liquid.

For copper, the rate limiting electron transfer reaction is the $Cu^{++} + e^- \longrightarrow Cu^+$ step. Because this reaction requires the transfer of electrons with energies in the forbidden gap, copper ion reduction involves surface states and is therefore inherently

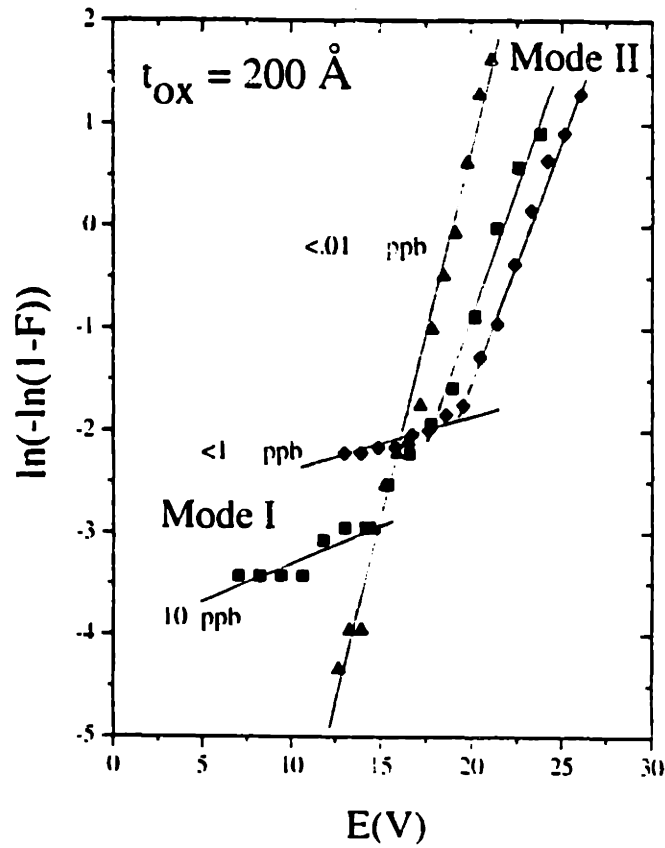

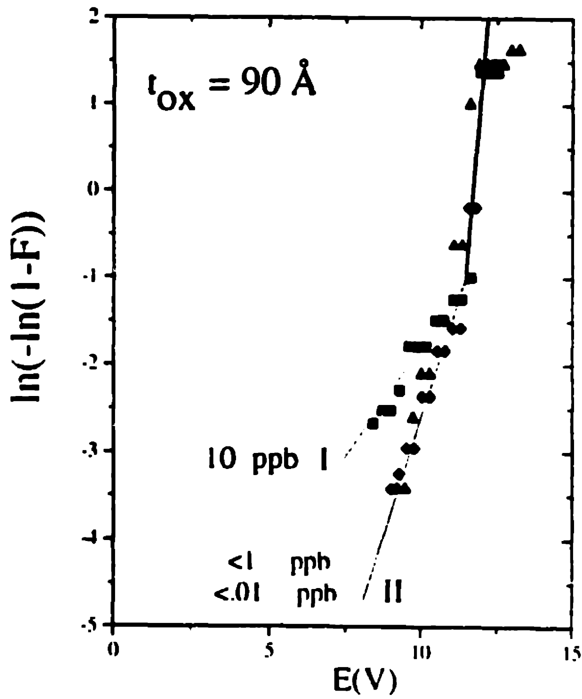

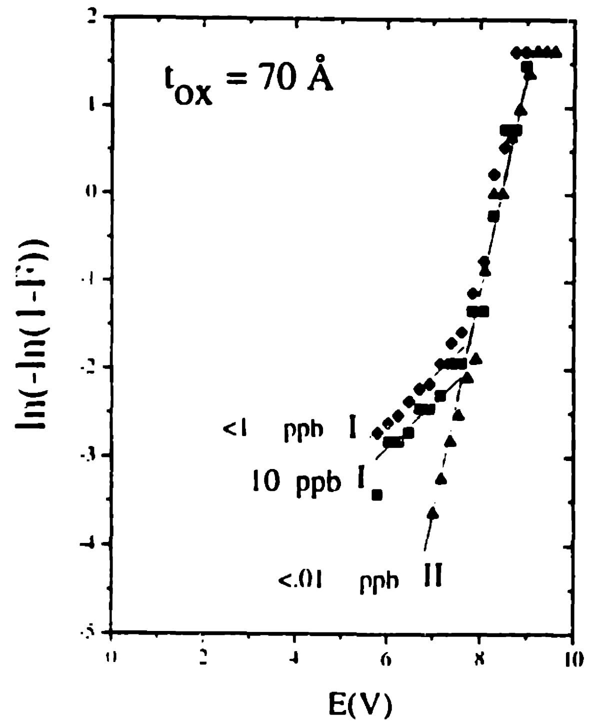

Figure 6-22: Weibull plots of breakdown voltage E_{bd} for 200 A. 90 Aand 70 Aoxides.

slow.

Increasing the HF concentration drastically reduces the copper. Meanwhile, part per million levels of chlorine *increase* the nucleation rate by increasing the rate constant of the $Cu^{++} + e^- \longrightarrow Cu^+$ step.

For large amounts of copper in solution, nucleation is fast and the deposition reaction occurs predominantly at the Cu precipitate/solution interface. Because the reduction of copper ions at an existing copper nucleus is facile, the deposition process is diffusion limited at high levels of copper ions in solution. Low intensity llumination increases both the nucleation and the growth rate on p as well as n-type silicon. The increase in growth rate is the result of the higher concentration of holes at the surface, which assist the anodic reaction (silicon dissolution). The increase in nucleation rate is explained by the increase in driving force for deposition, due to the shift in electron quasi fermi level.

Connecting the silicon to a Pt electrode via an ohmic contact drastically reduces nucleation on n as well as p-type. Because H^+ reduction at Pt requires a very low overpotential, the effect of the contact is to pin the electron quasi fermi level at the H^+/H_2 level, effectively decreasing the driving force for the copper reduction reaction.

RFPCD measures surface defects. For metallic contaminant detection, surface defects can either be metal precipitates or individual metal atoms chemisorbed to the silicon surface. As discussed in Chapter 5, chemisorbed metal atoms introduce deep levels in the bandgap which act as efficient recombination centers. Metallic precipitates perturb the periodic potential surface, introducing surface states. Using AFM, we determined the cross section of copper precipitates to be approximately $2{\cdot}10^{-14}cm^2$.

For Cu, deposit morphology controls RFPCD response. On p-type, the preponderance of precipitate growth over precipitate nucleation leads to larger precipitates, reducing the sensitivity of the surface lifetime to copper coverage. For gold ions, the variation of surface lifetime with time confirms a diffusion-limited deposition process ($\tau \approx t^{-1/2}$ and $N_{Au} \approx t^{1/2}$). For copper, the decrease of the surface lifetime is much slower. We believe this slow decrease to represent an increase in the cross section,

not the number, of surface states. The slow increase in cross section is the result of copper ion reduction at the pre-exististing surface state.

The strong increase in surface state density resulting from air exposure leads to reduction of physisorbed copper ions. The reduction reaction leads to copper atoms, divalently bonded to the silicon. The cross sections for individual metal atoms is 10^{-15} cm^2 for copper and 10^{-17} cm^2 for gold. Air exposure followed by lifetime measurement in 48 % HF allows detection of copper levels down to 10^8 cm^2. This is a factor of 50 better than the lowest detection limits achievable with state-of the-art TXRF equipment.

Finally, we have investigated the effect of 10^9 cm^{-2} - 10^{11} cm^{-2} copper levels on the dielectric breakdcwn characteristics of ultrathin gate oxides (< 100 Å). Even exposure to a 1:100 HF solution specified to have copper below 1 ppb in the HF, introduces sufficient copper on the surface to degrade the breakdown strength of 90 and 70 Åoxides. This observation proves the need for continually reducing surface metal concentrations as feature sizes are scaled down.

Chapter 7

Metallic Contaminants in Oxidizing Cleaning Solutions

7.1 Introduction

While recent work has elucidated the mechanism by which particles deposit onto wafer surfaces [30], a comprehensive description of metallic contamination in oxidizing solutions is still missing. The strong contamination tendency of iron in SC-1 has been attributed to its very low ionic solubility in basic solutions [145]. To explain the differences in contamination tendency among various metals in SC-1, some authors have proposed the stability of their oxide [146] as a quantitative measure. This approach is quite successful in explaining some general trends, but it fails to clarify the underlying mechanism of the contamination process.

E-pH diagrams [1] have been used extensively in the past for predicting corrosion equilibria in aqueous solutions. In this chapter, we present their first application to wet silicon processing. Because E-pH diagrams offer a graphic summary of the relevant reaction chemistry, they are expected to be of great value for the design of cleaning solutions for optimum cleaning effectivess[147].

[1] E-pH maps are also known as Pourbaix diagrams, after Marcel Pourbaix, who introduced them in his PhD thesis at Delft University in 1945.

7.2 Thermodynamics of metallic contaminants in oxidizing cleaning solutions

7.2.1 Introduction

E-pH diagrams map the stable phase (metal, oxide or ion) as a function of pH and redox potential, E, of the solution. For example, the E-pH diagram for the Fe-H_2O system at 75°C, showing the stability regions for the various solids (Fe, Fe_2O_3 and Fe_3O_4) and ionic species (Fe^{++} and Fe^{+++}) is shown in Figure 7.1. The boundary between a solid and soluble species moves into the solid region for lower concentrations in solution. In the figure, the boundaries for 1, 10^{-3} and 10^{-6} molality in solution are shown.

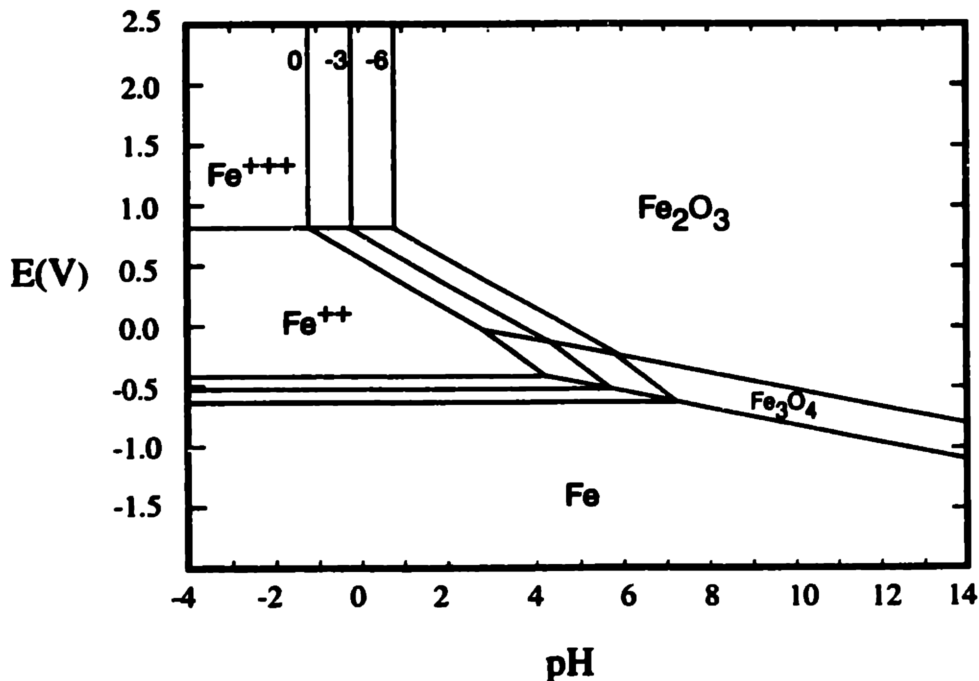

Figure 7-1: The E-pH diagram for the Fe-H_2O system at 75°C, with the stability regions for Fe, Fe_2O_3, Fe_3O_4, Fe^{++} and Fe^{+++}. Phase boundaries for 1, 10^{-3} and 10^{-6} molal concentration are shown.

The construction of the diagram involves the computation of the various solid/solution equilibria as a function of E and pH, using the standard electrode potential, E_o, of

the ions, and the free energy of formation (ΔG_f^o) of the oxides. Diagrams for the metal-H_2O system at room temperature are available for most metallic elements from Pourbaix [148]. While the formation of species other than the various oxides and aqueous ions is not treated here, E-pH diagrams which take into account the formation of silicates, silicides, and complex ions in solution can readily be calculated. In this chapter, we consider the chemical reactions of metallic species in an aqueous cleaning environment. This approach uniquely describes oxidizing cleaning solutions, where metal reaction with the silicon is limited by the presence of a chemical oxide.

7.2.2 The representation of cleaning solutions on an E-pH map

The equilibrium redox potential of a solution containing a single redox couple is given by Nernst's Law :

$$E = E_o + \frac{RT}{zF} ln(\frac{a_{ox}}{a_{red}}) \quad (7.1)$$

where a_{ox} and a_{red} are the activities of the oxidized and reduced state of the couple, respectively, z is the number of exchanged electrons, R is the ideal gas constant (8.314 J/mol·K) , F is Faraday's constant (96,500 J/V·mol) and T is the temperature of the cleaning solution in Kelvin. In oxidizing cleaning solutions, the redox potential is essentially fixed by the concentration of oxidant present. The relationship between the oxidant content and the redox potential can be derived by applying Nernst's Law to the reduction reaction of the oxidant. For example, for hydrogen peroxide, the reduction reaction can be written as :

$$H_2O_2 + 2H^+ + 2e^- \longrightarrow 2H_2O \quad (7.2)$$

Yielding a redox potential :

$$E = 1.776 - 2.303 \cdot \frac{RT}{F} pH + \frac{RT}{2F} ln([H_2O_2]) \quad (7.3)$$

Analogous relationships can be derived for other oxidizing cleaning mixtures based on nitric acid (e.g., HCl/HNO_3 and HF/HNO_3) or ozone (e.g., H_2O/O_3). In summary, the oxidant content determines the redox potential E much like the acid/base make-up of the mixture determines the pH. Approximate (E, pH) values of some standard wafer cleaning mixtures are shown on an E-pH map in Figure 7.2.

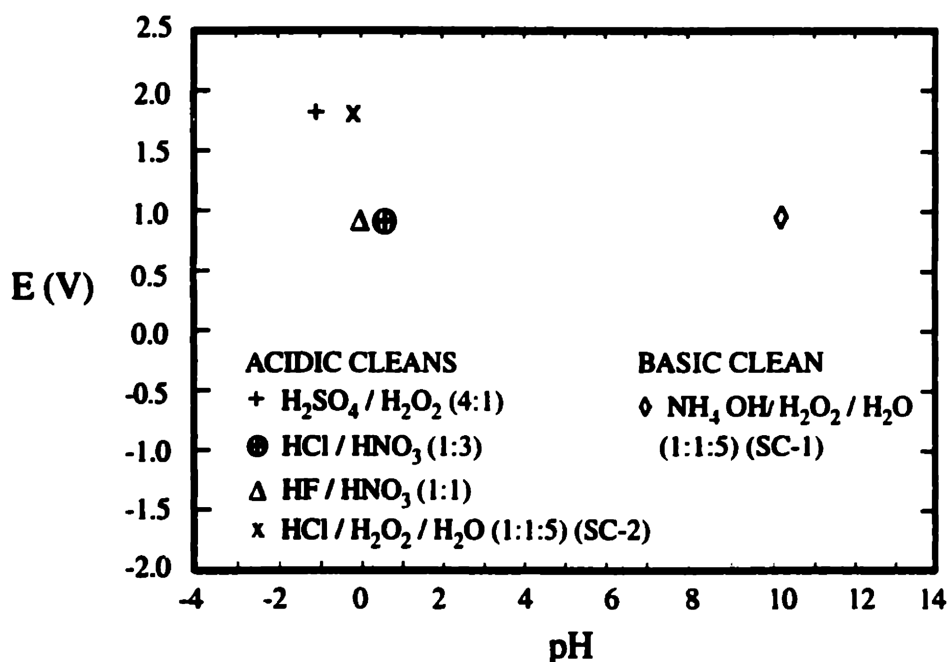

Figure 7-2: (E, pH)-values for some standard cleaning mixtures. The E values were calculated based on the reduction reaction of the oxidant, assuming standard cleaning solution compositions. For the acid solutions, the pH values are based on the assumption of complete dissociation (strong acid). The pH value for SC-1 was determined by pH measurement.

7.2.3 E-pH diagrams for metallic contaminants

If a cleaning solution falls in the stability region of a solid oxide phase for a given metal, then any ions of that metal present in the cleaning solution can lower their free energy by forming the metal oxide. (This deposition mechanism will be discussed in more detail in the next section.) E-pH diagrams delineate the regions in the solution

composition domain where a high tendency for oxide formation exists. They can therefore be used to accurately predict contamination by trace metal ions present in the cleaning mixture. Similarly, if the (E, pH) point of a cleaning solution lies in a region where an ion is the stable phase, then no deposition will occur ; and any metal present on the wafer surface will be removed by dissolution. This principle is illustrated below for a number of common contaminant metals.

E-pH diagram of Ca The E-pH diagram of Ca at 75°C is shown in Figure 7.3.

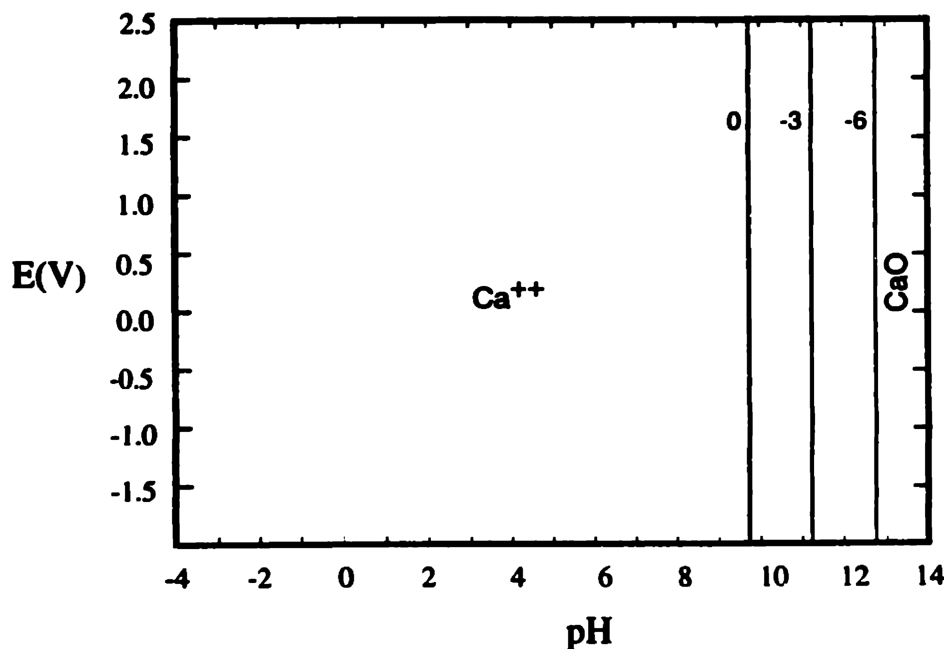

Figure 7-3: The E-pH diagram for the Ca-H_2O system at 75°C. Phase boundaries for 1, 10^{-3} and 10^{-6} molal concentration are shown.

As the pH is increased, the solubility decreases as CaO is formed. This agrees with the observations of Ca contamination in SC-1 (pH=10) [149]. Using this diagram, we predict that *increasing the pH of SC-1 will lead to more Ca depositing from solution.* Meanwhile, changing E by varying the hydrogen peroxide concentration will have no effect on the Ca contamination level.

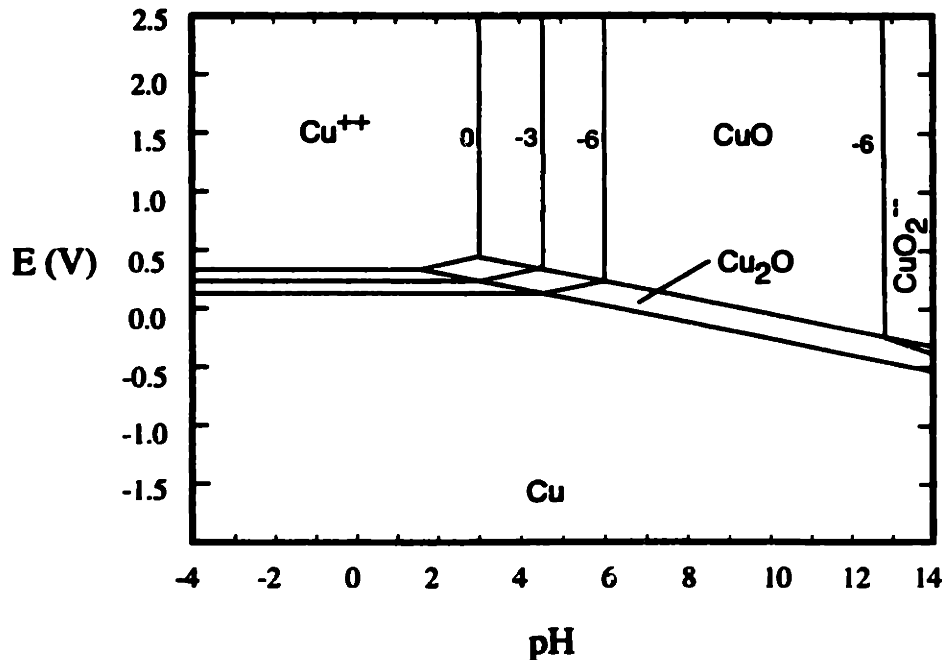

Figure 7-4: The E-pH diagram for the Cu-H_2O system at 75°C. Phase boundaries for 1, 10^{-3} and 10^{-6} molal concentration are shown

E-pH diagram of Cu The E-pH diagram of Cu at 75°C is shown in Figure 7.4. (The diagrams for Al, Ni and Zn all share the same principal features with the Cu diagram.)

From the position of the acidic oxidizing cleaning solutions in the region of high ionic solubility, it is clear that copper will be kept in solution as Cu^{++} when the pH is sufficiently low.

At intermediate pH, trace amounts of Cu will tend to deposit on the wafers as CuO. For high pH, the formation of $HCuO_2^-$ and CuO_2^{--} is increasingly favored [148], and ultimately CuO_2^{--} becomes the stable phase. Thus, in the high pH range (pH > 10), increasing the pH will *decrease* the amount of Cu depositing from solution.

E-pH diagram of Fe The position of SC-1 (NH_4OH/H_2O_2), deep in the stability region of Fe_2O_3 (Figure 1), explains why deposition of this metal from contaminated SC-1 solutions occurs so readily. Because of the high ionic solubility at low pH, *acidic cleaning solutions can be used to remove Fe contamination after SC-1.* At low pH,

a strongly oxidizing solution (E > 1V) will be *less effective* in removing Fe than a solution with low oxidation potential because Fe_2O_3 has a lower solubility as Fe^{+++} than as Fe^{++}.

E-pH diagram of Cr The E-pH diagram for Cr at 75°C is shown in Figure 7.5. SC-1 falls in the stability region of the CrO_4^{--} ion. Thus. in SC-1, contamination of the wafer surface by chromium will not occur and any chromium present on the wafer surface will readily dissolve as CrO_4^{--}.

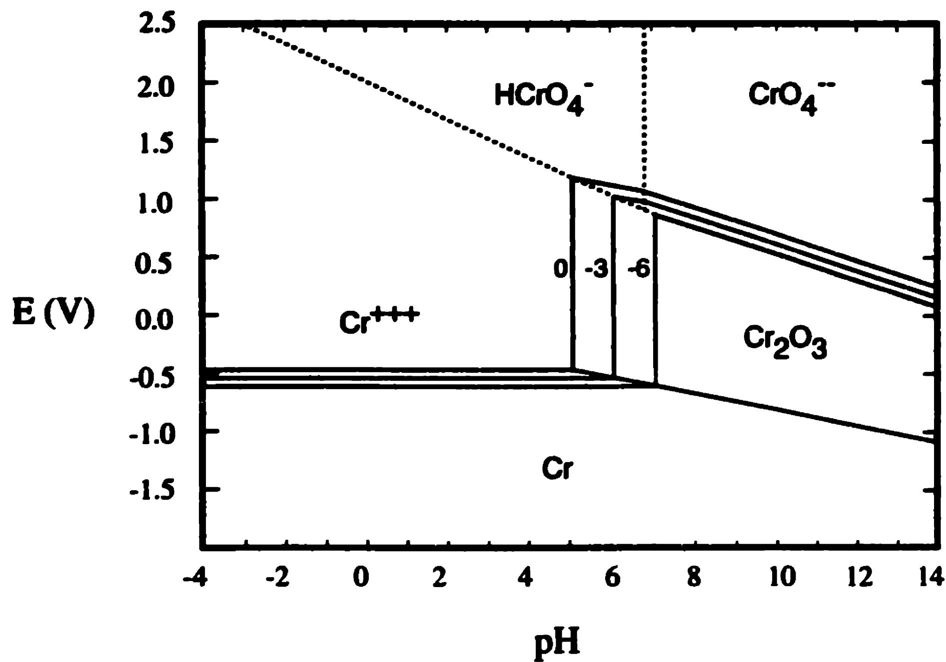

Figure 7-5: The E-pH diagram for the Cr-H_2O system at 75°C. Phase boundaries for 1, 10^{-3} and 10^{-6} molal concentration are shown.

E-pH diagram of Na The E-pH diagram for Na at 75°C is shown in Figure 7.6. From the position of the peroxide cleaning mixtures (H_2SO_4/H_2O_2, NH_4OH/H_2O_2, HCl/H_2O_2) near the Na^+/ Na_2O phase boundary, we predict that Na_2O will deposit on the wafer surface when the solubility limit is exceeded. Further increasing either the redox potential, E, or the pH of the solution, will strongly decrease the solubility limit for Na, and therefore more Na will deposit from solution. However, because of

the large stability region of the Na^+ ion over the entire pH range, immersion of the wafer in a solution with lower E (e.g., deionized water (DI)) will readily redissolve the Na_2O.

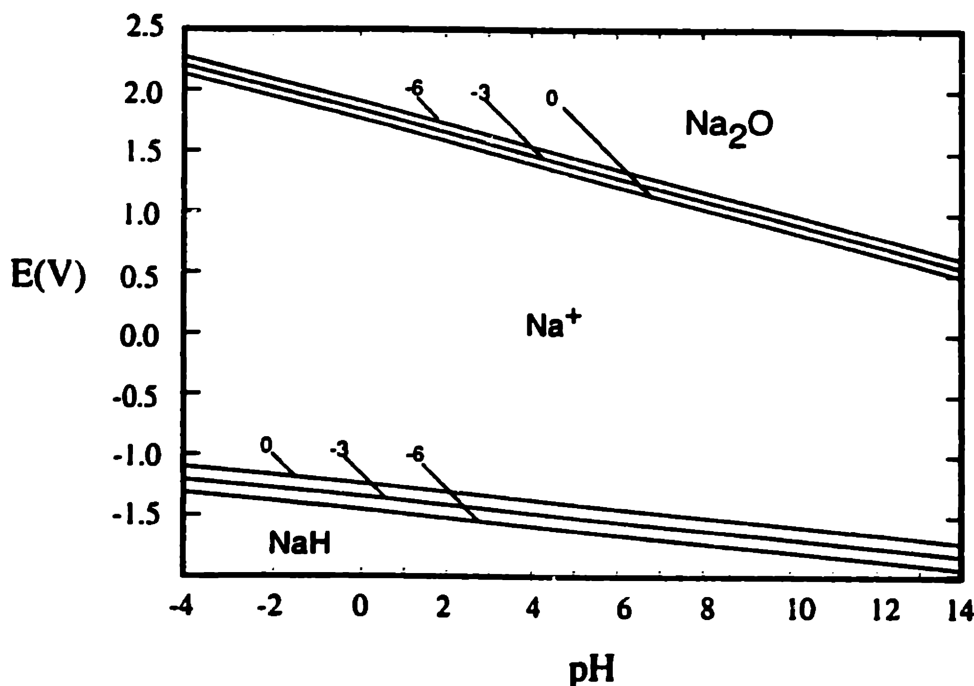

Figure 7-6: The E-pH diagram for the Na-H_2O system at 75°C. Phase boundaries for 1, 10^{-3} and 10^{-6} molal concentration are shown.

Table 7.1 shows the stable metallic species formed for SC-1 conditions, and the reactions describing the equilibrium between the stable solid and ionic species. In the cases where the metal is highly soluble for SC-1 conditions. no deposition occurs. The very high deposition tendency observed for Fe [28] agrees with the absence of a stable ionic species near the point representing SC-1 on the Fe E-pH diagram. The lower deposition tendencies observed experimentally for Zn, Ni and Cu can be explained by the existence of a stable anion species on the high-pH side of the SC-1 point. The anomalous deposition behavior of Al, which has an E-pH map similar to Ni, Cu and Zn, but a deposition tendency greater than Fe, can be explained by the formation of a silicate rather than an oxide upon deposition. The effect of silicate formation on

Element	Stable phase	Precipitation Reaction	Deposition ?
Al	Al_2O_3	$AlO_2^- + H^+ = 1/2\ Al_2O_3 + 1/2\ H_2O$	High
Fe	Fe_2O_3	$Fe^{+++} + 3/2\ H_2O = 1/2\ Fe_2O_3 + 3H^+$	High
Zn	ZnO	$HZnO_2^- + H^+ = ZnO + H_2O$	Medium
Ni	NiO	$Ni^{++} + H_2O_2 = NiO_2 + 2H^+$	Low
Cu	CuO	$HCuO_2^- + H^+ = CuO + H_2O$	Low
Cr	CrO_4^{--}	$2CrO_4^{--} + 4H^+ + H_2O = Cr_2O_3 + 3H_2O_2$	No
Na	Na^+	$Na^+ + 1/2\ H_2O = H^+ + 1/2\ Na_2O$	No
Mo	$HMoO_4^{--}$	$HMoO_4^- + H^+ = MoO_3 + H_2O$	No
V	HVO_4^{--}	$2H_2VO_4^- + 2H^+ = V_2O_4 + H_2O_2 + 2H_2O$	No

Table 7.1: The stable ionic or oxide species formed for SC-1 conditions and the experimentally observed deposition tendency.

the deposition tendency is discussed in detail in the next section.

In conclusion, E-pH diagrams delineate the regions in the solution composition domain where a contamination tendency by oxide formation exists. They can be used to predict the deposition tendency of metals in cleaning solutions of arbitrary pH and oxidant content. Conversely, they allow the design of a cleaning chemistry capable of removing a given metallic contaminant. Since contamination effects due to changes in solution conditions (concentration and temperature) can readily be modeled, E-pH diagrams are expected to be of significant value for optimizing the cleaning effectiveness of wet chemical systems.

7.3 Kinetics of metal deposition and removal in oxidizing cleaning mixtures

7.3.1 The deposition mechanism

As pointed out by Hurd and coworkers [150], the reactivity of metal ions towards silica gels has been recognized as far back as 1925 [151]. Because the silanol group is

weakly acidic, it can be substituted by a metal ion. Based on this earlier work, we propose the following mechanisms for the reversible adsorption of a metal ion (*e.g.*, Cu) onto a hydroxylated silica surface:

- at low pH (<7):

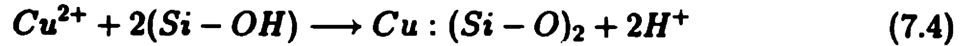

$$Cu^{2+} + 2(Si - OH) \longrightarrow Cu : (Si - O)_2 + 2H^+ \tag{7.4}$$

- at high pH (>7):

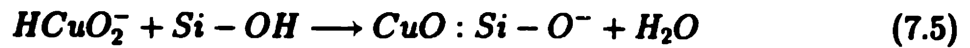

$$HCuO_2^- + Si - OH \longrightarrow CuO : Si - O^- + H_2O \tag{7.5}$$

After bonding on the silica surface, copper has retained its oxidation state (2+), and is bonded to oxygen, which itself is bonded to silicon. Thus, bonding state of the metal resembles a silicate. In the following, we present a phenomenological model for the kinetics of the deposition process, based on the thermodynamics of condensed phases.

7.3.2 Driving force for deposition

The free energy of the ion as it becomes included in the silicon oxide is shown in Figure 7.7 as a function of reaction coordinate. ΔG^* is activation energy of the deposition reaction. ΔG_R is the difference in chemical potential between the metal oxide dissolved in the silicon oxide and the metal ion in solution. - ΔG_R is the *thermodynamic driving force for deposition* and can be expressed in terms of fundamental thermochemical properties of the depositing metal as shown below.

For example, for the case of copper in SC-1, the E-pH diagram can be used to determine the dissolved ionic species ($HCuO_2^-$) in equilibrium with the SC-1 cleaning solution. Thus, deposition will occur as expressed by reaction (7.5). ΔG_R for Cu deposition can be be expressed in terms of the standard reaction free energy, ΔG_R^o, of reaction (7.5) as follows :

$$\Delta G_R = \Delta G_R^o + RTln(\frac{a^h(CuO : SiO^-)}{a^h(HCuO_2^-)}) \tag{7.6}$$

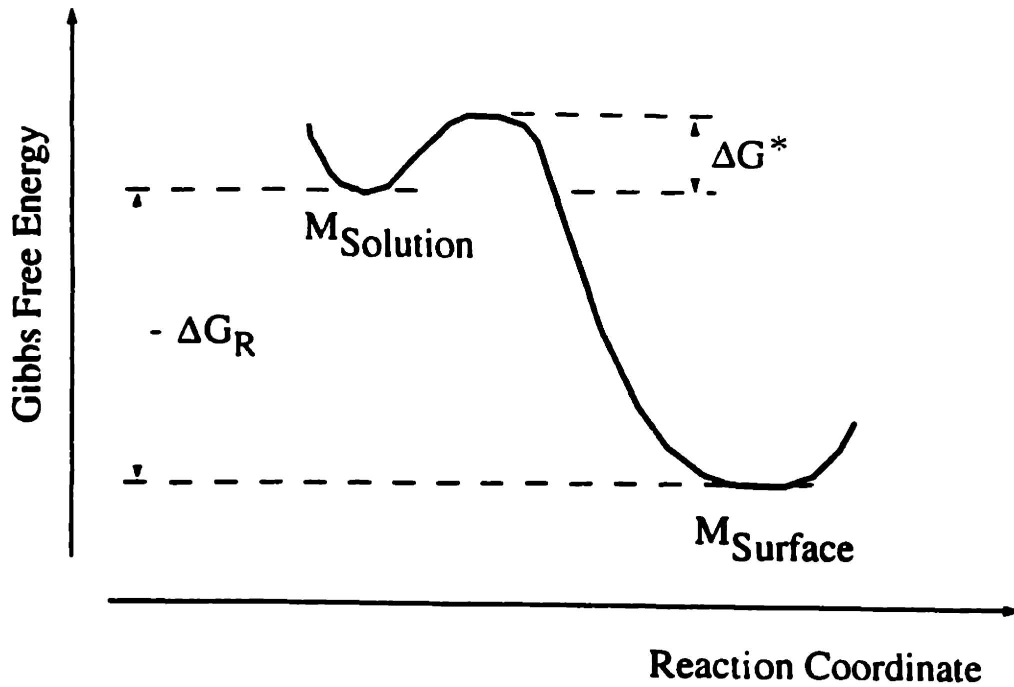

Figure 7-7: The Gibbs free energy of a metal ion undergoing incorporation in the silicon oxide, as a function of reaction coordinate. The energy barriers for the forward and reverse reaction are ΔG^* and $\Delta G^* - \Delta G_R$.

where the a^h are Henryan activities. Using equation (4), ΔG_R^o can be written as :

$$\Delta G_R^o = \Delta G^o(H_2O) + \Delta G^o(CuO : SiO^-) + RTpH - \Delta G^o(HCuO_2^-) \qquad (7.7)$$

where $\Delta G^o(CuO : SiO^-)$ is the Gibbs free energy in the Henryan reference state. This value is different from the free energy of formation of the pure oxide, $\Delta G^o(CuO)$ [106]:

$$\Delta G^o(CuO : SiO^-) = \Delta G^o(CuO) - RTln\gamma_{CuO}^o \qquad (7.8)$$

Where γ_{CuO}^o is the Raoultian activity coefficient for CuO on the silica surface at infinite dilution. The phenomenological constant γ_{CuO}^o is related to the bond stability of the silicate-like final bonding state on the silicon surface. An estimate for γ_{CuO}^o can be obtained from the standard Gibbs energy, ΔG_{silic}^o, for the formation of a silicate

from the metal oxide and SiO_2:

$$\gamma^o_{CuO} = exp(\Delta G^o_{silic}/RT) \tag{7.9}$$

Where ΔG^o_{silic} is the standard Gibbs free energy of the following reaction:

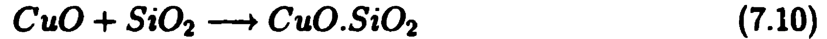

$$CuO + SiO_2 \longrightarrow CuO.SiO_2 \tag{7.10}$$

Some values for ΔG^o_{silic} are shown in in Table 7.2.

silicate	ΔG^o_{silic} (kcal/mol)
$ZnO.SiO_2$	-22.75
$NiO.1/2SiO_2$	-8.55
$Al_2O_3.SiO_2$	-145.83
$FeO.1/2SiO_2$	-12.35

Table 7.2: Standard free energies for the formation of a silicate from the metal oxide and SiO_2.

As long as we are dealing with sufficiently dilute solutions, the Henryan activity coefficients approach unity and expression (7.6) becomes :

$$\Delta G_R = \Delta G^o_R + RTln(\frac{c(CuO : SiO_2)}{c(CuO_2^-)}) = \Delta G^o_R + RTln(\frac{c}{c_s}) \tag{7.11}$$

where c and c_s are shorthand notations for the metal concentrations in the oxide and the cleaning solution respectively. They are expressed as atoms/cm^3.
Expressions (7.7), (7.8) and (7.9) define -ΔG_R, the instantaneous thermodynamic driving force for Cu deposition, in terms of c, c_s, and the fundamental thermodynamic properties γ^o_{CuO} and ΔG^o of the oxide and ion species involved.
The steady-state segregation coefficient k between the cleaning solution and the oxide is defined as :

$$k = \frac{c_{sat}}{c_s} \tag{7.12}$$

Where c_{sat} is the surface contaminant concentration at t = ∞ after immersion in the

cleaning solution. At thermodynamic reaction equilibrium ($\Delta G_R = 0$), (7.11) yields :

$$k_{eq} = exp(-\Delta G_R^o/RT) \tag{7.13}$$

Where $k_{eq} = c_{eq}/c_s$ is the equilibrium segregation coefficient between the cleaning solution and the oxide. Equation (7.13) signifies that, at thermodynamic equilibrium, the contaminant concentration in the oxide scales linearly with the concentration in the cleaning solution.

7.3.3 Model for simultaneous etching, deposition and oxidation

A simple model for the cleaning solution-wafer interface which combines oxidation, etching and deposition is shown in Figure 7.8. The model builds on the following assumptions :

- 1. An oxide layer with thickness d (cm) is present on the wafer. We assume that a uniform contaminant concentration c_o (atoms/cm^3) is present in a layer of thickness a within the oxide.

- 2. The oxide is etched at a constant rate r (cm/s). The etch rate depends on the nature of the cleaning solution. In SC-2 and Piranha, the etch rate is close to zero. In SC-1, the etch rate is small and depends on the NH_4OH concentration. In HF/HNO_3 and HF/H_2O_2, the etch rates can be quite high.

- 3. For positive values of the thermodynamic driving force ($\Delta G_R < 0$), a deposition flux, Φ_{dep}, of metal ions will be included in the chemical oxide (layer thickness a) as it is formed. For negative values of the thermodynamic driving force ($\Delta G_R > 0$), metals are being leached out of the oxide, while at the same time it is being etched by the cleaning solution.

- 4. We assume that surface reaction is slow compared to diffusion in the liquid. Consequently, the concentration profile will be flat and surface reaction will control the deposition process.

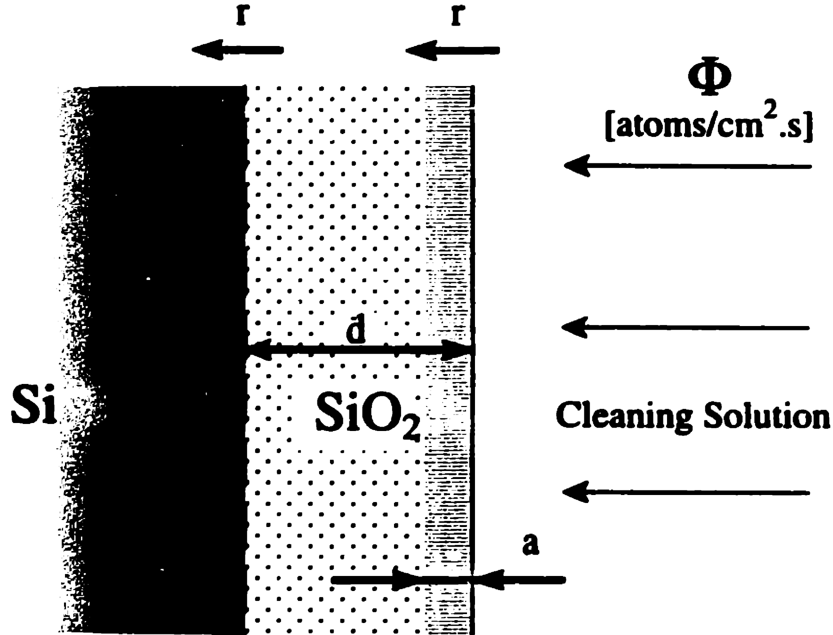

Figure 7-8: Model for the cleaning solution–wafer interface (r=etching speed ; d = oxide thickness ; Φ = flux of contaminant atoms). The contamination is concentrated in the outer layer (thickness a) of the chemical oxide.

Using the energy diagram of Figure 7.7, the forward and reverse reaction flux (atoms/cm²s) of contaminant atoms can be related to the height of the free energy barriers ΔG^* and $\Delta G^* - \Delta G_R$ as follows :

$$\Phi^+ = f^o exp(\frac{-\Delta G^*}{RT}) \tag{7.14}$$

$$\Phi^- = f^o exp(\frac{-\Delta G^* + \Delta G_R}{RT}) \tag{7.15}$$

With f^o representing a constant. Summation of (7.14) and (7.15) yields the net deposition flux (atoms/cm²) of contaminant into the oxide :

$$\Phi_{dep} = \Phi^+ - \Phi^- = f^o exp(\frac{-\Delta G^*}{RT})(1 - exp(\frac{\Delta G_R}{RT})) \tag{7.16}$$

7.3.4 Time dependence of the surface contaminant level

Since the etching of silicon dioxide, containing c metal atoms/cm^3, at a rate r (cm/s) results in a removal of $r.c$ atoms/cm^{2}s we can define an etch flux Φ_{etch} as

$$\Phi_{etch} = r.c \tag{7.17}$$

The change of the metal concentration in the chemical oxide can then be found from the continuity equation :

$$a.\frac{dc(t)}{dt} = \Phi_{dep} - \Phi_{etch} \tag{7.18}$$

Since the concentration in the liquid at the surface is assumed to be equal to the value in the bulk of the liquid, the equilibrium surface contaminant level is given by :

$$c_{eq} = c_s.exp(\frac{-\Delta G_R^o}{RT}) \tag{7.19}$$

By substituting (7.11) in (7.16), we obtain the following expression for the net flux, as a function of the instantaneous (c) and equilibrium (c_{eq}) surface contaminant level

$$\Phi_{dep} = f^o exp(\frac{-\Delta G^*}{RT})(1 - c/c_{eq}) \tag{7.20}$$

Substitution in (7.18), with initial condition :

$$c(t = 0) = c_0 \tag{7.21}$$

where c_0 (atoms/cm^3) is the initial surface concentration. yields the following differential equation :

$$\frac{dc(t)}{dt} + c(t)(\frac{r}{a} + \frac{\Phi_o}{ac_{eq}}) = \frac{\Phi_o}{a} \tag{7.22}$$

where :

$$\Phi_o = f^o exp(\frac{-\Delta G^*}{RT}) \tag{7.23}$$

Solving the differential equation yields the deposition transient :

$$c(t) = c_o + (c_{sat} - c_o)(1 - exp(-\frac{t}{\tau})) \tag{7.24}$$

where c_{sat}, the saturation surface concentration of contaminant, is given by :

$$c_{sat} = (\frac{r}{\Phi_o} + \frac{1}{c_{eq}})^{-1} \tag{7.25}$$

And τ is a time constant given by :

$$\tau = (r/a + \frac{\Phi_o}{a.c_{eq}})^{-1} \tag{7.26}$$

In this expression, the terms r/a and $\Phi_o/a.c_{eq}$ characterize the etch rate and deposition rate, respectively.

If diffusion between the bulk liquid and the liquid layer adjacent to the surface is the rate limiting step of the deposition reaction, then the process is under *diffusion-control.* For $\Delta G_R^o < 0$, an approximate solution can be found by assuming that the contaminant concentration drops from its value in the bulk of the liquid, c_s^∞, to zero at the solid/liquid interface over a boundary layer with thickness δ. Thus, the reaction flux becomes independent of the contaminant level in the oxide, c :

$$\Phi_{dep} = \frac{Dc_s^\infty}{\delta} \tag{7.27}$$

where c_s^∞ is the contaminant concentration in the bulk of the solution and D is the diffusivity of the metal ion in the cleaning solution. Solving the continuity equation (7.18) using equation (7.27) yields a saturation contaminant level :

$$c_{sat} = \Phi/r = \frac{Dc_s^\infty}{\delta r} \tag{7.28}$$

The time constant of the deposition transient (equation 7.24) is given by :

$$\tau = a/r \tag{7.29}$$

7.3.5 Discussion of model results

Some results of the model for the case of surface reaction control are shown in Figures 9 and 10.

Figure 7.9 shows the time dependence of the surface contaminant concentration, i.e. the deposition transient, equation (7.24). The parameter k_{eq} (equation (7.10)) is a measure for the strength of the driving force. For high k_{eq}, the saturation contaminant level c_{sat} (equation (7.25)) is largely determined by the magnitude of the etch rate, r. and only weakly dependent on k_{eq}. For nonzero etch rate, c_{sat} will be *smaller* than the thermodynamic equilibrium value c_{eq}.

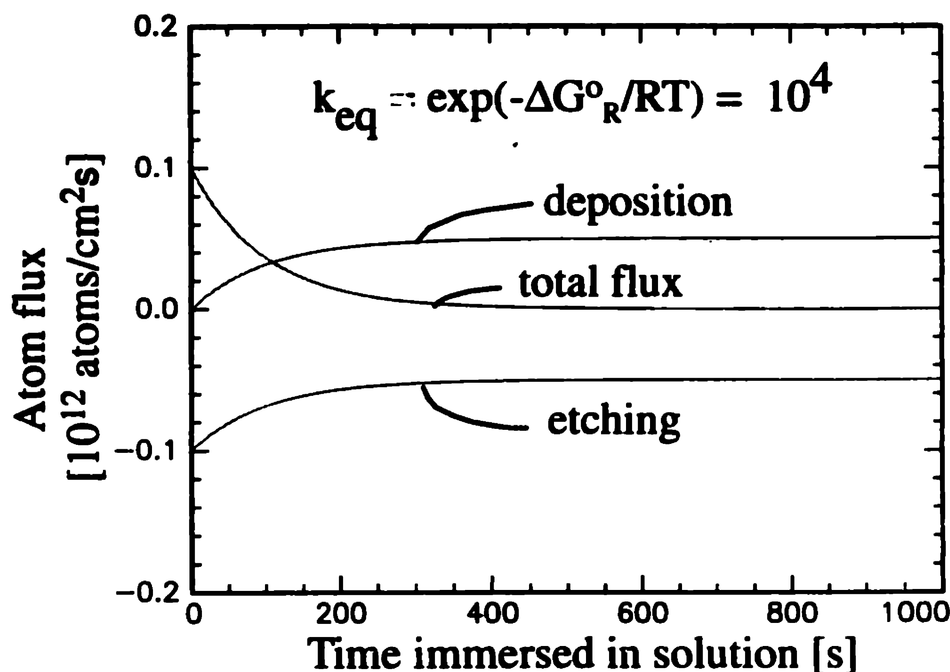

Figure 7-9: Effect of the magnitude of the driving force on the deposition transient. The following mode! parameters were used : k_{eq} = exp(- ΔG^o_R/RT), $c_o=10^{12}$ atoms/cm^2, a = 2 nm, $\Phi_o=10^{11}$/cm^2, r=0.01 nm/s.

Deposition and etching are competing processes. The time-dependence of the etching and deposition fluxes is shown in Figure 7.10. The change in contaminant concentration over time, dc(t)/dt, is determined by the difference between deposition and etch flux (equation (7.18)). In steady state, the deposition flux Φ_{dep} is compen-

sated entirely by the etch flux Φ_{etch}, and hence $dc(t)/dt = 0$.

In the case where diffusion controls the deposition process, the final contaminant level is dependent on the diffusivity of metal ions in the liquid, the boundary layer thickness and the etch rate (equation (7.28)), rather than on the value of the thermodynamic driving force. In conclusion, both etching and mass transport effects will cause the steady-state segregation coefficient ($k = c_{sat}/c_s$) to deviate from its equilibrium value k_{eq} predicted by thermodynamics.

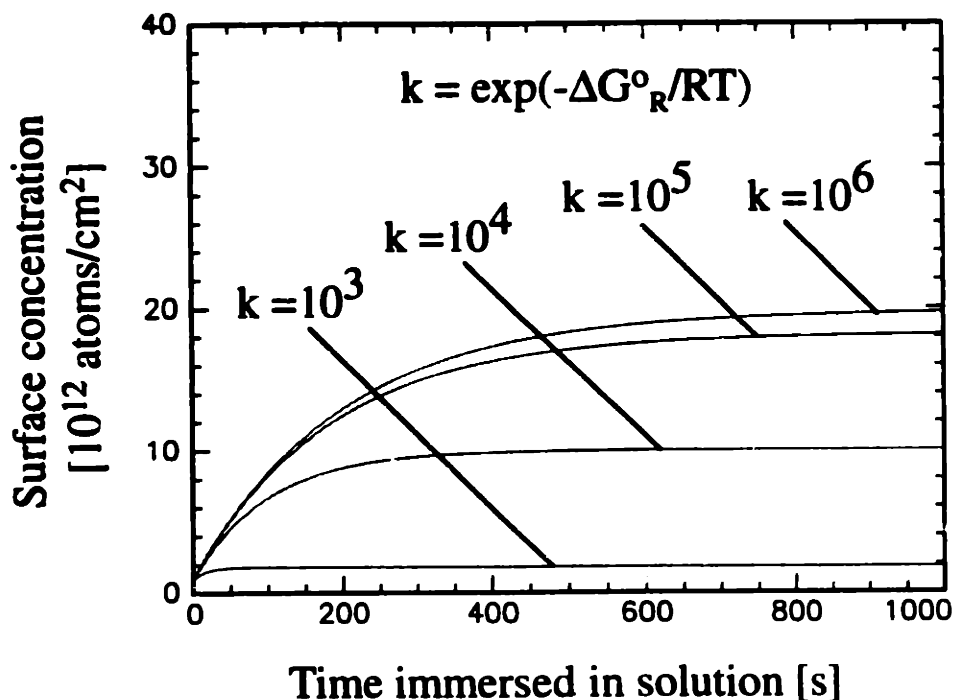

Figure 7-10: The total contaminant flux as the sum of deposition (Φ_{dep}) and etching (Φ_{etch}) fluxes. The following model parameters were used : $k_{eq} = 10^4$, $c_o = 20 \cdot 10^{12}$ atoms/cm^2, $a = 2$ nm, $\Phi_o = 10^{11}$/cm^2, $r = 0.01$ nm/s.

7.4 Conclusions

In this chapter we demonstrated the use of condensed phase thermodynamics for studying metallic contaminants in the various mixtures used for wafer cleaning. Metals deposit on a hydrophilic surface by deprotonation of surface silanol groups, leading

to a silicate-like bonding arrangement. E-pH diagrams map the ionic solubility as a function of solution conditions (oxidizing potential, E, and pH). Using E-pH diagrams, the tendencies of different metals to deposit from the various commonly used cleaning solutions can be predicted with reasonable accuracy, based on the assumption that an oxide is formed. Excellent agreement with experiment is obtained when silicate formation is included.

The strong deposition tendencies of Al, Fe, Zn and to a lesser extent Ni and Cu in the basic cleaning solution SC-1 arise from the high driving force for oxide formation from the stable ionic species. For certain metals such as Zn, Ni, Fe, and most notably Al, contribution of the silicate formation reaction to the driving force has to be considered. The effect of silicate formation on the deposition tendency of Al from SC-1 is illustrated in Figure 7.11 using the Al-H_2O and the Al-Si-H_2O E-pH diagrams.

E-pH diagrams are a universal tool for analyzing the behavior of metallic contaminants in cleaning solutions. They allow a quick assessment of the impact of compositional changes on cleaning effectiveness. For example, we predict that decreasing the pH will reduce Ca deposition from SC-1. Meanwhile, Cu, Al, Ni and Zn deposition will be increased. Fe deposition from SC-1 is hard to avoid and acidic cleaning solutions are needed to remove Fe after SC-1. Fe deposition will occur more easily in acidic solutions with a high oxidizing potential ($E > 1V$)[2].

We presented a kinetic model for metal removal and deposition in oxidizing solutions. Cleaning or contamination occur by virtue of a gradient in the Gibbs free energy, which acts to redistribute contaminants between the oxide and the solution; etching of the growing oxide constitutes an additional mechanism for contaminant removal. Due to etching and mass transport effects, the saturation contaminant level on the surface may deviate from its thermodynamic equilibrium value.

In this chapter, we did not consider reactions involving charge transfer between the silicon bands and ions in solution. As mentioned earlier, this approach is uniquely useful for oxidizing cleaning solutions, where the presence of an insulating chemical

[2]This prediction has been verified experimentally [152].

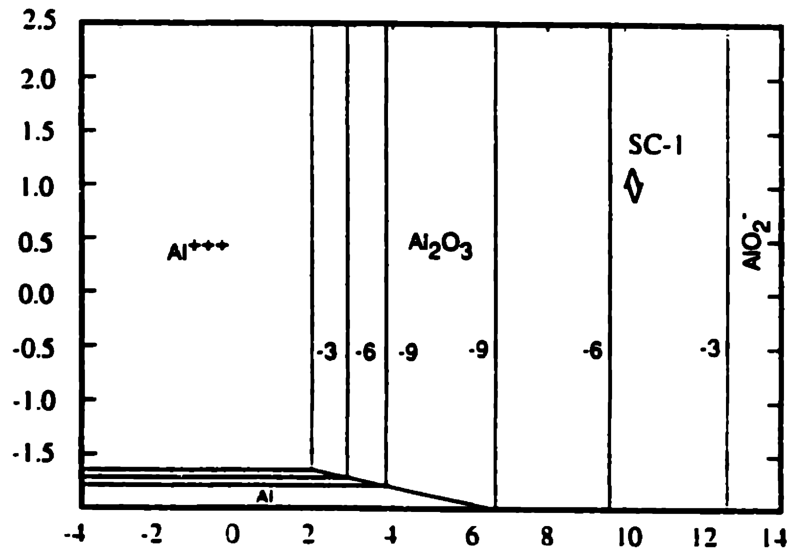

(a)

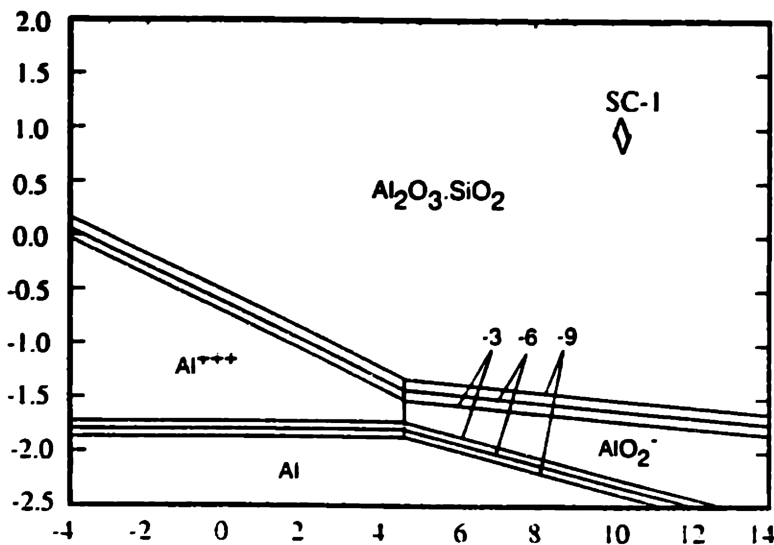

(b)

Figure 7-11: The E-pH diagram for the Al-H_2O system at 75°C. (a) without taking into account silicate formation and (b) assuming the formation of the silicate phase $Al_2O_3.SiO_2$. Phase boundaries for 10^{-3}, 10^{-6}, and 10^{-9} molal concentration are shown.

oxide makes the occurrance of such reactions highly unlikely. Effects of complexing and chelating compounds on deposition equilibria [153, 8] were not discussed in the present chapter, but their effects can readily be included provided the requisite thermodynamic data is available.

Chapter 8

Research Achievements, Applications and Future Strategies

8.1 Summary

Radio-Frequency Photoconductance Decay (RFPCD) is a noninvasive technique to measure carrier lifetime in silicon. Using high bulk lifetime (> 1 ms), unpatterned Czochralski material, RFPCD allows the measurement of very low levels of surface defects (detection limit $\approx 10^8$ cm^2). We have used RFPCD for *in situ* studies of silicon surface reactions in various ambients.

To ensure accurate quantification of surface state density, control of injection level during the RFPCD measurement is important. We have developed a detailed theoretical model for the dependence of the surface recombination velocity (SRV) on injection level in the presence of surface charge. SRV is modulated by the band-bending potential, ϕ_s reaching a maximum at full depletion. In turn, ϕ_s varies with instantaneous injection level, as the bands are flattened under the influence of excess carriers. We propose a straightforward model for the dependence of SRV on Δn in the presence of surface charge. Our model assumes high bulk lifetime, τ_b, and low

SRV, so that quasi-equilibrium holds throughout the wafer thickness. Because SRV is small, we may assume that the photoresponse of the bands obeys pn junction-type behavior.

For bands bent into accumulation by an amount ϕ_s. surface recombination is decreased by a factor $\exp(q\phi_s/kT)$. Bands bent into depletion will increase surface recombination, but this effect is easily thwarted by bias illumination which acts to flatten the bands. For bias light levels corresponding to low level injection, band bending in inversion gives rise to a decrease in surface recombination velocity (increase in surface lifetime) as the injection level is increased in the low injection level regime ($\Delta n << $ doping level).

We have verified the correctness of this model by measurements on a p-type oxidized wafer using a pulsed infrared LED source for carrier excitation. At the highest injection levels, the high injection lifetime $\tau_n + \tau_p$ is recovered. Intermediate injection levels, corresponding to flatband conditions, provide τ_n. The ratio of minority to majority carrier lifetimes establishes the cross section ratio, $\tau_n/\tau_p = \sigma_p/\sigma_n$. At the lowest injection levels, the bands at the surface relax back towards their equilibrium position in the dark and the surface recombination is increased. We show that the dependence of the effective lifetime on injection level in the bandbending regime can be used to extract surface charge. We found a value of $9 \times 10^{11} cm^{-2}$, which we attribute to fixed oxide charge resulting from the thermal oxidation with no anneal. Reasonable agreement with the predictions by Deal *et al.* [70] was obtained.

We have studied the kinetics of surface reactions on monolayer terminated Si (100) based on the results of electronic structure calculations at the Hartree-Fock level. The reactivity of chemisorbed halogens towards polar molecules such as water and HF easily gives rise to etching by backbond insertion (in HF) and the formation of silanol groups by hydrolysis (in air and water). The kinetics of both reactions for the different halogens can be understood based on the bond polarity and bond order of silicon-halogen bons.

Surface silanols undergo a condensation reaction, catalyzed by moisture, which leads to a bridgebonded oxygen atom and two silicon dangling bonds. The surface

states, introduced by the dangling bonds, are close to midgap and can therefore be detected by means of surface lifetime measurements. Chemisorption of reducible metals such as Cu also introduces surface states, which are due to orbitals localised on the metal atom.

Metal deposition from dilute HF was studied in detail using TXRF, ICP-MS, and AFM. On thermodynamic grounds, the reduction reaction of metal ions at the silicon surface is only possible for metals with sufficiently positive standard reduction potential, such as Cu and the noble metals. Less electronegative metals, such as Fe and V, do not undergo reduction, although physisorption of the ion onto the hydrogen passivated surface does occur. For copper, the thermodynamic driving force for reduction at the Si/solution interface is relatively small and nucleation is required. For gold ions, with a much higher driving force for reduction, the critical nucleus size is smaller than one atom and therefore deposition occurs atom by atom. Because the free energy of gold ions in solution overlap with the silicon valence band, gold ions can inject holes into the valence band and are reduced instantaneously upon adsorption. The deposition of gold on silicon is rate-limited by gold ion diffusion in the liquid.

Reduction of copper ions is mediated by electron capture from surface states by the Cu^{++}/Cu^{+} couple. Because of the low density of bandgap states on HF-immersed silicon, this reduction mechanism occurs much more slowly than the hole injection observed for gold ions. The nucleation rate of copper nuclei on n-type is considerably larger than on p-type because the areal density of filled surface states is larger on n-type. Low intensity illumination increases the driving force for deposition by increasing the fermi energy (for n-type) or the quasi-fermi energy for electrons (for p-type) with respect to ion levels in solution. The increase in driving force is reflected in an increase in the nucleation rate for material of both types under illumination. Simultaneously, light increases the growth rate of copper nuclei as the concentration of holes at the surface is increased.

For prolonged exposure or high copper concentrations, the deposition reaction becomes dominated by precipitate growth, and copper reduction occurs predominantly

at the Cu/HF solution interface. Reduction of copper ions at the Cu/dilute HF interface is fast, and therefore the copper deposition is rate limited by copper ion diffusion in the liquid in this regime. Small amounts of chlorine (ppm) *increase* the the nucleation rate, by reducing the overpotential of the $Cu^{++} + e^- \longrightarrow Cu^+$ reaction.

Using RFPCD in combination with AFM we showed that SRV on copper contaminated wafer scales with the areal density of copper precipitates. Because the anodic reaction rate is higher on p-type material, larger precipitates are formed on p-type material, and the sensitivity of RFPCD for copper detection is reduced. The cross section per precipitate is approximately 10^{-14} cm^2. For less than 10^{10} cm^{-2} copper coverage, we measure a capture cross section of 8x10^{-17} cm^2 for holes and 5x10^{-17} cm^2 for electrons, consistent with a larger critical nucleus size on p-type material. Air exposure has a large effect on the surface lifetime response for low copper levels (less than 10^{10} cm^{-2}). We attribute this effect to the reduction of physisorbed copper ions at surface states, introduced by incipient native oxide growth. With ambient exposure, the cross section per copper atom becomes approximately 10^{-15} cm^2 and copper levels as low as 10^8 cm^{-2} can be detected. For gold, the cross section is approximately 10^{17} cm^2, independent of carrier type, resulting in a lower detection limit of 10^{10} cm^{-2}.

A quantitative description of metal removal and deposition phenomena in oxidizing cleaning solutions is possible using E-pH diagrams. These diagrams define a thermodynamic driving force for deposition, which is the difference between the chemical potential of the metal ion in the cleaning mixture and the metal or metal oxide on the silicon surface. Metals which form stable ions in solution will easily be removed; meanwhile, metals that form stable oxides or silicates will have a high tendency to deposit. A kinetic model, which combines the thermodynamic driving force with etching and mass transport effects, was presented.

8.2 Applications

The increases in process complexity in silicon IC manufacturing have intensified the need for rapid. nondestructive wafer characterization tools to prevent yield loss by timely detection of process contamination. In-line detection of contaminants requires an analysis technology which is fast, sensitive. and noninvasive [15]. For effective control of IC manufacturing processes, defect identification is desirable, but less important than detection sensitivity. Because surface cleanliness prior to thermal front-end-of-line (FEOL) process steps is especially critical in ULSI processes. early detection of contaminants in wet chemical solutions has received increased attention recently [154, 155].

Though lifetime measurements have been widely used for in-line detection of defects and impurities, their scope has so far been limited to measurement of bulk lifetime for characterization of process purity [49]. To detect surface impurities, a timeconsuming drive-in step is needed, as well as effective surface passivation during the measurement. In this thesis we have reported, for the first time, *in situ* lifetime measurements during wet cleaning. We demonstrated the use of RFPCD measurements on wafers residing in the cleaning solution, elimininating the need for "monitor" wafers for *ex situ* surface analyses.

The capability to detect low levels of surface defects with RFPCD is critically dependent upon the bulk lifetime of the material analyzed. Table 8.1 lists the bulk lifetimes measured on today's commercial CZ silicon material. The extraordinary bulk quality of today's prime CZ material has enabled us to detect surface defects at concentrations well below the detection limit of state-of-the-art surface analysis techniques. We can define N_{ldl}, the lower detection limit for surface defects, as:

$$N_{ldl} = \frac{d}{2\sigma v_{th}\tau_b} \tag{8.1}$$

N_{ldl} is the density of surface defects that will result in a 50 % degradation in effective lifetime. According to Equation 8.1, the detection limit for surface defects depends on their cross section, the thickness of the wafer, and its bulk lifetime. Table

Vendor	size(in)	polish	τ_b	thickness (μm)	N_{ldl}(cm^{-2})
MEMC	4	ssp	80μs	575	$4 \cdot 10^{10}$
MEMC	5	ssp	100μs	625	$3 \cdot 10^{10}$
MEMC	6	ssp	800 μs	675	$4 \cdot 10^{9}$
MEMC	8	ssp	17ms	725	$2 \cdot 10^{8}$
SEH	5	dsp	7ms	625	$4 \cdot 10^{8}$
SEH	5	ssp	7ms	625	$4 \cdot 10^{8}$
SEH	6	dsp	10ms	675	$3 \cdot 10^{8}$
SEH	6	ssp	10ms	675	$3 \cdot 10^{8}$

Table 8.1: Typical bulk lifetimes of commercial CZ material (dsp = double side polished; ssp = single side polished) and their influence on the lower detection limit for surface defects, N_{ldl}.

7.1 lists the detection limit for 'typical' defects (cross section $\sigma=10^{-15}$cm^2).

If the purpose is to monitor the cleanliness of a cleaning solution, not the wafer surface, improved detection sensitivity for copper is possible using a thin, high lifetime silicon sample [1]. As expressed by Equation 8.1, the detection limit of the RFPCD technique scales with sample thickness. By making use of 10 μm samples, the sensitivity of RFPCD to surface defects can be improved by a factor of 50, boosting the sensitivity to 10^8 cm^{-2} for *in situ* detection and 2x10^6 cm^{-2} for *ex situ* measurements in 48 % HF. These values are predictions which will have to be verified by careful exposure tests in high purity solutions.

As pointed out earlier, a prerequisite for detection of ions is their reduction from solution. Physisorbed ions do not introduce surface states and will not be detected. For metals such as Fe and V which are less noble than Cu, reduction from solution does not occur spontaneously, but a cathodic bias to the silicon during immersion will likely allow detection. While the surface lifetime measurement does not allow impurity identification, measurement of the variation of the lifetime with small sample bias can be used to establish the energy position of the defect introduced by the impurity, and hence its identity (Section 4.4).

8.3 Future strategies

After three decades of continual exponential growth, the global semiconductor industry has reached a point where future growth prospects are threatened, not by demand saturation, but by the significant environmental impact of its manufacturing operations. As other industries are reducing their emissions, the growth in the semiconductor industry leads to a rising share in the generation of hazardous chemical waste, volatile hydrocarbons and ozone depleting chemicals. Because this trend is hard to justify in an environmentally conscious world, the need to include the total environmental impact in the cost of ownership of a manufacturing tool has been realized. Since wet cleaning operations contribute significantly to the generation of

[1]FZ wafers with thickness in the 10 μm range are commercially available [156].

hazardous waste, new cleaning approaches with reduced environmental impact will become a priority in future cleaning research.

Stringent purity standards are a major factor in the volume of waste chemicals generated. Therefore, a "just clean enough" philosophy is key to minimizing chemicals usage [157]. Here, *in situ* monitoring of chemical purity, as was demonstrated in this thesis using RFPCD, has a major role to play, because it allows better assessment of process risk from trace contaminants in the cleaning bath, and hence reduction of waste generated by unnecessary bath changes. In addition, the design of more "robust" cleaning solutions, *i.e.* chemistries which achieve satisfactory contaminant removal even when liquid purity specifications are relaxed, could add significantly to the lifetime of cleaning solutions.

Our research provides a firm theoretical framework for designing new cleaning methods with improved metal removal efficiency and relaxed purity constraints. We have introduced E-pH diagrams for ready assessment of contamination risk based on the ionic solubility limit. Future uses of E-pH diagrams include the design and control of more robust cleaning chemistries, *e.g.* electrolytic wafer cleaning , and the use of complexants to improve metal removal efficiency. For HF-based solutions, we showed that increasing the oxidation potential of the solution or reducing the light level on the wafer will decrease the driving force for copper deposition by lowering the energy of electrons in the silicon with respect to reducible ions in solution. A related approach to mimimize metallic contaminant deposition is to increase the electrode potential of the silicon by draining electrons to an external source, be it a potentiostat or a noble metal electrode immersed in the HF solution. While the use of electrochemistry opens interesting opportunities for wafer cleaning, process integration issues, as well as the effect of (small) anodic biases on silicon dissolution and surface roughening, will have to be carefully addressed.

Bibliography

[1] H. C. Gatos, Surface Science **299-300**, 1-23 (1994).

[2] I. Tamm, Physic. Z. Sow. **1**, 733 (1932).

[3] W. Shockley, Phys. Rev **56**, 317 (1939).

[4] J. Bardeen, W. H. Brattain, Phys. Rev. **71**, 717 (1947).

[5] G. Moore, IEEE Spectrum **16**, 30 (1979).

[6] S. Verhaverbeke, "Dielectric Breakdown in Thermally Grown Oxide Layers", PhD Thesis, KU Leuven (June 1993).

[7] "SIA Semiconductor Technology - Workshop Working Group Reports", p 78, Semiconductor Industry Association, 1993.

[8] W. Kern, Editor, "Handbook of Semiconductor Wafer Cleaning Technology", Noyce Publications, New Jersey, 1995.

[9] W. Bergholz, G. Zoth, F. Gelsdorf, B. Kolbesen, in: Defects in Silicon II, W. M. Bullis, U. Gosele, F. Shimura, Editors, ECS Proceedings Volume 91-9, p 21, The Electrochem. Soc. Softbound Proceedings Series, Pennington, NJ (1991).

[10] S. Verhaverbeke, M. Meuris, P. W. Mertens, M. M. Heyns, A. Pilipossian, D. Graef, A. Schnegg in : Techn. Dig. IEDM, p 71, IEEE, Piscataway, NJ (1991).

[11] W. B. Henley, L. Jastrzebski, N. F. Haddad, Mat. Res. Soc. Symp. Proc. Vol. 315, 299 (1993).

[12] M. Morita, T. Ohmi, Jpn. J. Appl. Phys. **33**, 370 (1994).

[13] S. L. Cohen, MRS Symp. Proc. Vol. 315, 49 (1993).

[14] T. Ohmi, M. Miyashita, M. Itamo, T. Imaoka, I. Kawanabe, IEEE Trans. Electron Dev. **39**, 537 (1992).

[15] L. C. Kimerling, J. Michel, H. M'saad, G. J. Norga, in: "Semiconductor Characterization: Present Status and Future Trends", W. M. Bullis, D. G. Seiler, A. C. Diebold, Eds., AIP, NY, 1996.

[16] A. Ohsawa, K. Honda, N. Toyokura, J. Electrochem. Soc. **131**, 12 (1984).

[17] G. Zoth, W. Bergholz, J. Appl. Phys. **67**, 6764 (1990).

[18] W. B. Henley, L. Jastrzebsky, N. Haddad, MRS Symp. Proc. Vol. 315, 299 (1993).

[19] M. M. Heyns, S, Verhaverbeke, M. Meuris, P. W. Mertens, H. Schmidt, M. Kubota, A. Philipossian, K. Dillenbeck, D. Graef . A. Schnegg, R. de Blank, MRS Symp. Proc. Vol. 315, 35 (1993).

[20] E. R. Weber, Appl. Phys. **A 30**, 1 (1983).

[21] R. Keller, M. Deicher, W. Pfeiffer, H. Skudlik, D. Steiner, Th. Wichert, Phys. Rev. Lett. **65**, 2023 (1990).

[22] L. Zhong, F. Shimura, Jpn. J. Appl. Phys. **32**, L1113 (1993).

[23] H. Wendt, H. Cerva, V. Lehmann, W. Palmer, J. Appl. Phys. **65**, 2402 (1989).

[24] L. Zhong, F. Shimura, Appl. Phys. Lett. **61**, 1078 (1992)

[25] H. Dallaporta, M. Liehr, J. E. Lewis, Phys. Rev. **B 41**, 5075 (1990).

[26] H. M'saad, "The Role of Surface and Bulk Defects in the Processing and Performance of Crystalline Silicon", PhD Thesis, Materials Science and Engineering, MIT (September 1994).

[27] W. Kern, RCA Review **31**, 187 (1970).

[28] O. J. Anttila, M. V. Tilli, J. Electrochem. Soc., **139**. 1180 (1992).

[29] M. Meuris, S. Verhaverbeke, P. W. Mertens, M. M. Heyns, L. Hellemans, Y. Bruynseraede, A. Philipossian, Jpn. J. Appl. Phys. **31**, L1514 (1992).

[30] D. J. Riley, R. G. Carbonell, J. Colloid Interface Sci. **158**, 259 (1994).

[31] S. Verhaverbeke, M. Meuris, P. Mertens, H. Schmidt, M. M. Heyns, A. Philipossian, D. Graef, K. Dillenbeck, in : Proceedings of the Fourth International Symposium on Ultra Large Scale Integration Science and Technology, ECS Proceedings Volume 93-13, p 199, The Electrochem. Soc. Softbound Proceedings Series, Pennington, NJ (1993).

[32] Y. J. Chabal, MRS Symp. Proc. Vol. 259, 349 (1991).

[33] T. Ohmi, in : Cleaning Technology in Semiconductor Device Manufacturing, J. Ruzyllo, R. E. Novak, Editors, ECS Proceedings Volume 94-7, p 3, The Electrochem. Soc. Softbound Proceedings Series, Pennington, NJ (1994).

[34] R. Takizawa, T. Nakanishi, K. Honda, A. Ohsawa, Jpn. J. Appl. Phys. **27**, L2210 (1988).

[35] W. Kern, Editor, "Handbook of Semiconductor Wafer Cleaning Technology", p 121, Noyce Publications. New Jersey, 1995.

[36] J. R. Vig, in "Handbook of Semiconductor Cleaning Technology", W. Kern, Ed., pp 233-273, Noyce Publications, New Jersey, 1995.

[37] P. H. Singer, "Trends in Wafer Cleaning", Semiconductor International, p 36 (December 1992).

[38] D.A. Bohling, S. E. Beck. B. S. Felcker, A. G. Gilicinski, J. C. Ivankovits, J. G. Langan, S. W. Rynders. J. A. T. Norman, D. A. Roberts, G. Voloshin, M. A. George, D. M. Hess, A. Lane, in : Cleaning Technology in Semiconductor Device Manufacturing, J. Ruzyllo, R. E. Novak, Editors, ECS Proceedings Volume 94-7, p 253, The Electrochem. Soc. Softbound Proceedings Series, Pennington, NJ (1994).

[39] L. C. Kimerling, J. L. Benton, J. J. Rubin, Inst. Phys. Conf. Series **59**, 217 (1981).

[40] C. R. Brundle, C. A. Evans Jr., S. Wilson, Eds., "Encyclopedia of Materials Characterization: Surfaces, Interfaces, and Thin Films," Butterworth Heinemann, Manning, 1992.

[41] R. H. Brigham, Private communication.

[42] G. Binnig, C. F. Quate. Ch. Gerber, Phys. Rev Lett **56**, 930 (1986).

[43] O. M. R. Chyan, J. J. Chen, H. Y. Chien, to be published in J. Electrochem. Soc.

[44] J. A. Sees, L. H. Hall, O. M. R. Chyan, J. J. Chen, H. Y. Chien, Proceedings of the 2nd International Symposium on Ultraclean Processing of Silicon Surfaces (UCPSS'94), p 147, Acco, Leuven, 1994.

[45] J. E. Cantle, "Atomic Absorption Spectrometry", Elsevier, Amsterdam, 1982.

[46] A. R. Date, A. L. Gray, Eds., "Applications of Inductively Coupled Mass Spectroscopy", New York, Chapman and Hall, 1989.

[47] IMEC Ultra Clean Processing Group, Leuven, Belgium.

[48] D. T. Stevenson, R. J. Keyes, J. Appl. Phys. **26**, 190 (1955).

[49] T Boone, G. S. Higashi. J. L. Benton, R. C. Kistler, G. R. Weber, R. C. Keller, G. Makris, MRS Symp. Proc. 315, 359 (1993).

[50] T. S. Horanyi, P. Tutto, Cs. Kovacsics, J. Electrochem. Soc. **143**, 216 (1996).

[51] Y. Kirino, A. Buczkowski, Z. J. Radzimski, G. A. Rozgonyi, F. Shimura, Appl. Phys. Lett. **57**, 2832 (1990).

[52] J. W. Orton, P. Blood, "The Electrical Characterization of Semiconductors: Measurement of Minority Carrier Properties", p 71, Academic Press, New York, 1990.

[53] D. K. Schroder, "Semiconductor Material and Device Characterization", p 367, Wiley, New York, 1990.

[54] J. I Pankove, "Optical Processes in Semiconductors", p 11, Dover, New York, 1975.

[55] E. Yablonovitch, T. Gmitter, Appl. Phys. Lett. **49**, 587 (1986).

[56] W. Shockley, W. T. Read, Phys. Rev. **87**, 835 (1952).

[57] R. N. Hall, Phys. Rev. **87**, 387 (1952).

[58] A. Buczkowski, J. J. Radzimksi, G. A. Rozgonyi, F. Shimura, J. Appl. Phys. **72**, 2873 (1992).

[59] A. Buczkowski, J. J. Radzimksi, G. A. Rozgonyi, F. Shimura, J. Appl. Phys. **69**, 6495 (1991).

[60] K. L. Luke, L. J. Cheng, J. Appl. Phys. **61**, 2282 (1987).

[61] A. Aberle, A. Glunz, W. Warta, J. Appl. Phys. **71**, 4422 (1992).

[62] S. W. Glunz, A. B. Sproul, A. Warta, W. Wettling, J. Appl. Phys. **75**, 3 (1994).

[63] A. Kaniava, U. Menczigar, J. Vanhellemont, J. Poortmans, A. L. P. Rotondaro, E. Gaubas, J. Vaitkus, L. Koster, D. Graf, MRS Symp. Proc. Vol. 386, 389 (1995).

[64] Fitzgerald, A. S. Grove, Surf. Sci **9**, 347 (1968).

[65] A. Many, Y. Goldstein, N. B. Grover, Semiconductor Surfaces, p 200, North Holland, Amsterdam, 1965.

[66] E. Yablonovitch, T. Gmitter, Appl. Phys. Lett. **49**, 587 (1986)

[67] Gamry Instruments, Willow Grove, PA.

[68] G. J. Norga, K. A. Black, A. J. Reddy, J. Michel, L. C. Kimerling, Paper presented at the 2nd Working Group Meeting on the Measurement of Minority Carrier Diffusion Length and Lifetime in Silicon Materials and Devices (NREL), Scottsdale, Arizona, January 17-19, 1996.

[69] PC-1D Solar Cell Simulation Package, Sandia National Laboratory.

[70] B. E. Deal, M. Sklar, A. S. Grove, E. H. Snow, J. Electrochem. Soc. **114**, 266 (1967).

[71] G. Ceder, M. Asta, D. de Fontaine, Nature **343**, 544-546 (1990).

[72] S. K. Ghandi, "VLSI Fabrication Principles", p 235, Wiley, New York, 1983.

[73] T. S. Horanyi, T. Pavelka, P. Tutto, Appl. Surf. Sci **63**, 306 (1993).

[74] H. M'saad, J. Michel, J. J. Lappe, and L. C. Kimerling, J. Electron. Mat. **23**, 487-491 (1994).

[75] C. G. Van de Walle, F. R. McFeely, S. T. Pantelides, Phys. Rev. Lett. **61**, 1867 (1988).

[76] G. W. Trucks, K. Raghavachari, G. S. Higashi, Y. J. Chabal, Phys. Rev. Lett. **65**, 504 (1990).

[77] M. S. Morse, Private communication.

[78] T. Hoshino, M. Tsuda, S. Oikawa, I. Ohdomari, Surf. Sci. **291**, L763 (1993).

[79] I. P. Batra, P. S. Bagus, K. Hermann, Phys. Rev. Lett. **52**, 384 (1984).

[80] Y. Miyamoto, A. Oshiyama, Phys. Rev. **B 43**, 9287 (1991).

[81] C. Okada, H. Kobayashi, I. Takahashi, J. Ryuta, T. Shingyouji, Jpn. J. Appl. Phys. **32**, L1031 (1993).

[82] M. Morita, T. Ohmi, E. Hagesawa, M. Kawakami, K. Suma, Appl. Phys. Lett. **55**, 562 (1989).

[83] M. Morita, T. Ohmi, E. Hagesawa, M. Kawakami,M. Ohwada, J. Appl. Phys. **68**, 1272 (1990).

[84] B. S. Meyerson, F. J. Himpsel, K. J. Uram, Appl. Phys. Lett. **57**, 1034 (1990).

[85] T. Konoshi, K. Uesugi, K. Takaoka, S. Kawano, M. Yoshimura, T. Yao, Jpn. J. Appl. Phys. **32**. 3131 (1993).

[86] D. Graef, M. Grundner, R. Schultz, L. Muelhoff, J. Appl. Phys. **68**, 5155 (1990).

[87] T. Konoshi, K. Uesugi, K. Takaoka, S. Kawano, M. Yoshimura, T. Yao, Jpn. J. Appl. Phys. **32**. 3131 (1993).

[88] P. J. Hay, W. R. Wadt, J. Chem. Phys. 82, 270 (1985); W. R. Wadt,P. J. Hay, J. Chem. Phys. 82, 284 (1985); P. J. Hay, W. R. Wadt, J. Chem. Phys. 82, 299 (1985)

[89] P. Hohenberg, W. Kohn, Phys. Rev. **B 136**, 864 (1964).

[90] W. Kohn, L. Sham, Phys. Rev. **A 140**, 1133 (1965).

[91] R. A. Friesner, Annu. Rev. Phys. Chem. **42**, 341 (1991).

[92] Gaussian Incorporated, Philadelphia, PA.

[93] Cerius2, Molecular Simulations Incorporated.

[94] A. Szabo, N. S. Ostlund, "Introduction to Advanced Electronic Structure Theory," Mc Graw Hill, New York, 1989.

[95] Y. J. Chabal, K. Raghavachari, Phys. Rev. Lett. **53**, 3 (1984).

[96] H. Bender, S. Verhaverbeke, M. Caymax, O. Vatel, M. M. Heyns, J. Appl. Phys. **75**, 1207 (1994).

[97] A. K. Rappé, C. J. Casewit, K. S. Colwell, W. A. Goddard, W. M. Skiff, J. Am. Chem. Soc. **114**, 10024 (1992).

[98] J. B. Foresman, A. Frisch, "Exploring Chemistry with Electronic Structure Methods, a Guide to Using Gaussian", Gaussian Inc., Philadelphia, PA, 1993.

[99] M. Nakamura, T. Takahagi, A. Ishitami, Jpn. J. Appl. Phys **32**, 3125 (1993).

[100] J. Matsuo. K. Karahashi, A. Sato, S. Hijiya, Jpn. J. Appl. Phys. **31**, 2025 (1992).

[101] P. L. Cowan, J. A. Golovchenko, M. F. Robbins, Phys. Rev. Lett. **4**, 1680 (1980).

[102] V. Chakarian, D. K. Shuh, J. A. Yarmoff, M. C. Hakansson, U. D. Karlsson, Surf. Sci. **296**, 383 (1993).

[103] N. Aoto, E. Ikawa, T. Kikkawa, Y. Kurogi, Surf. Sci **247**, 21 (1991)

[104] M. L. W. Vanderzwan, J. A. Bardwell, G. I. Sproule, M. J. Graham, Appl. Phys. Lett **64**, 446 (1994).

[105] G. J. Norga, M. R. Black, K. A. Black, H. M'saad, J. Michel, L. C. Kimerling, Mat. Sci. Forum **196-201**, 1531 (1995).

[106] C. H. P. Lupis, "Chemical Thermodynamics of Materials", p 161, North Holland, New York (1983)

[107] D. R. Frankl, "Electrical Properties of Semiconductor Surfaces", Pergamon, Oxford, 1967.

[108] W. H. Brattain, J. Bardeen, Bell Syst. Techn. J. **32**, 1 (1953).

[109] G. Wallis, S. Wang, J. Electrochem. Soc. **106**, 231 (1959).

[110] A. Many, D. Gehrlich, Phys. Rev. **107**, 404 (1957).

[111] D. R. Frankl, J. Electrochem. Soc. **109**, 238 (1962).

[112] D. R. Frankl, Phys. Rev. **128**, 2609 (1962).

[113] P. J. Boddy, W. H. Brattain, J. Electrochem. Soc. **109**, 812 (1962).

[114] R. Memming, Surf. Sci. **2**, 436 (1964).

[115] V. Margoninski, A. Gavron, Surf. Sci. **5**, 387 (1966).

[116] E. P. Matsas, L. L. Dyner, V. E. Primachenko, O. V. Snitko, Surf. Sci. **19**, 109 (1970).

[117] H. Gerischer, Surf. Sci. **18**, 97 (1969)

[118] H. Gerischer, in: Advances in Electrochemistry and Electrochemical Engineering, Vol. 1, Eds. P. Delahay and Ch. W. Tobias, Interscience, New York, 1961.

[119] S. R. Morrison, "Electrochemistry of Semiconductors and Oxidized Metal Electrodes", Plenum, New York, 1980.

[120] S. R. Morrison, "Chemical Physics of Surfaces", Plenum, New York, 1977.

[121] S. R. Morrison, in : "Treatise on Solid State Chemistry, Vol. 6B (Surfaces II)", N. B. Hannay, Ed., Plenum, New York, 1976.

[122] P. Allongue, in: Modern Aspects of Electrochemistry, Number 23, B. E. Conway *et al.*, Eds., pp 239-314, New York, Plenum (1992).

[123] P. Whoriskey, J. Appl. Phys. **29**, 867 (1958).

[124] E. Hsu, H. G. Parks, R. Craigin, S. Tomooka, J. S. Ramberg, R. K. Lowry, J. Electrochem. Soc. **139**, 3659 (1992).

[125] H. Aomi, F. Derouin, T. Ohmi, MRS Symp. Proc. Vol. 315, 333 (1993).

[126] H. Morinaga, M. Suyama, T. Ohmi, J. Electrochem. Soc. **141**, 2834 (1994).

[127] K. K. Yoneshige, H. G. Parks, S. Ragavan, J. B. Hiskey, P. Resnick, J. Electrochem. Soc. **142**, 671 (1995).

[128] I. Teerlinck, H. F. Schmidt, A. L. P. Rotondaro, T. Q. Hurd, L. Mouche, P. W. Mertens, M. Meuris, M. M. Heyns, D. Vanhaeren, W. Vandervorst, to be published in the Proceedings of the 4th International Conference on Cleaning Technology in Semiconductor Device Manufacturing, Chicago, Illinois, October 8-13, 1995.

[129] H. Reiss, A. Heller, J. Phys. Chem. **89**, 4207 (1985).

[130] Z. Nagy, J. P. Blaudeau, N. C. Hung, L. A. Curtiss, D. J. Zurawski, J. Electrochem. Soc. **142**, L87 (1995).

[131] J. N. Chazalviel, M. Stefenel, T. B. Truong, Surf. Sci. **134**, 865 (1983).

[132] M. Kuisl, E. Sasse, Surf. Sci. **92**, 681 (1980).

[133] R. Hockett, Private communication.

[134] D. R. Lide, Editor, "CRC Handbook of Chemistry and Physics", CRC Press, Boca Raton, 1990.

[135] L. A. Nagahara, T. Ohmori, K. Hashimoto, A. Fujishima, J. Vac. Sci. Technol. **A 11**, 763 (1993).

[136] K. Schouterden, "Deposition of Copper from HF Solutions", B. S. Thesis, Department of Chemistry, KU Leuven, 1993 (in Dutch).

[137] D. Graef, D. Grundner, L. Muelhoff, M. Dellith, J. Appl. Phys. **69**, 7620 (1991).

[138] G. Kortum, "Treatise on Electrochemistry", Elsevier, Amsterdam, 1965.

[139] H. J. Lewerenz, T. Bitzer, J. Electrochem. Soc. **139**, L22 (1992).

[140] H. J. Lewerenz, T. Bitzer, M. Gruyters, K. Jacobi, J. Electrochem. Soc. **140**, L45 (1993)

[141] T. Bitzer, M. Gruyters, H. J. Lewerenz, K. Jacobi, Appl. Phys. Lett. **63**, 397 (1993)

[142] W. R. Aderhold, N. Streckfuss, E. P. Burte, U. Keller, Proceedings of the 2nd International Symposium on Ultraclean Processing of Silicon Surfaces (UCPSS'94), Acco, Leuven, p 159.

[143] R. Falster, J. Appl. Phys. **66**, 3355 (1989).

[144] W. Weibull, Ing. Vetensk. Akad. Proc. **151**, 153 (1934).

[145] C. R. Helms, H. Park, in : Cleaning Technology in Semiconductor Device Manufacturing, J. Ruzyllo, R. E. Novak, Editors, ECS Proceedings Volume 94-7, p 26, The Electrochem. Soc. Softbound Proceedings Series, Pennington, NJ (1994).

[146] T. Ohmi, T. Imaoka, I. Sugiyama, T. Kezuka, J. Electrochem. Soc. **139**, 3317 (1992).

[147] G. J. Norga, L. C. Kimerling, J. Electron. Mat. **24**, 397 (1995).

[148] M. Pourbaix, "Atlas of Electrochemical Equilibria in Aqueous Solutions", p 389, Pergamon, Oxford, 1966.

[149] M. Meuris, M. Heyns, W. Kueper, S. Verhaverbeke, A. Philipossian, in: ULSI Science and Technology 1991, J. M. Andrews, G. K. Celler, Editors, ECS Proceedings Volume 91-11, p 454, The Electrochem. Soc. Softbound Proceedings Series, Pennington, NJ (1991).

[150] T. Q. Hurd, H. F. Schmidt, A. L. P. Rotondaro, L. H. Hall, M. M. Heyns, to be published in the Proceedings of the 4th International Conference on Cleaning Technology in Semiconductor Device Manufacturing, Chicago, Illinois, October 8-13, 1995.

[151] W. A. Patrick, E. H. Barclay, J. Phys. Chem. **29** 1400 (1925).

[152] P. M. Mertens, G. J. Norga, Unpublished data.

[153] K. Mishra, K. Osseo-Asare, D. Wei, Paper presented at the 3d International Conference on Cleaning Technology in Semiconductor Device Manufacturing, Chicago, Illinois, October 10-15, 1993.

[154] G. J. Norga, K. A. Black, H. M'saad, L. C. Kimerling, Mat. Sci. & Techn. **11**, 90 (1995).

[155] G. J. Norga, K. A. Black, M. R. Black, J. Michel, L. C. Kimerling, to be published in the Proceedings of the 4th International Conference on Cleaning Technology in Semiconductor Device Manufacturing, Chicago, Illinois, October 8-13, 1995.

[156] Virginia Semiconductor, Inc., Fredericksburg, VA.

[157] M. M. Heyns, Private communication.